ABSTRACT

Title of Document: ELECTROCHEMICAL SYNTHESIS, TRANSFORMATION, AND CHARACTERIZATION OF MNO_2 NANOWIRE ARRAYS FOR SUPERCAPACITOR ELECTRODES

Jonathon Duay, Doctor of Philosophy, 2013

Directed By: Professor, Sang Bok Lee
Department of Chemistry and Biochemistry

The utilization of MnO_2 nanowire arrays for future light weight energy storage devices is investigated here. One of the more specific questions this work looks to answer is: Can ultra high density arrays of MnO_2 nanowires really be used to create future flexible micro-supercapacitors with high energy density, high power density, and long cycle lives? This research investigates the energy storage properties of dense arrays of solely MnO_2 nanowires and synergistic MnO_2 nanowire composites consisting of two or more materials/architectures, where the composite materials are able to offset some of the detrimental intrinsic properties of the MnO_2 nanowires. Accordingly, a complete flexible supercapacitor device was prepared utilizing a coaxial MnO_2/poly (3, 4-ethylenedioxythiophene) (PEDOT) core/shell nanowire array cathode with a PEDOT nanowire array anode. This material demonstrated metrics considerably better than current devices even while being flexed. In addition, a hierarchical MnO_2

nanofibril/nanowire array was synthesized by transformation of a bare MnO_2 nanowire array. This material was investigated for its supercapacitor properties while altering the parameters of its nanowire and nanofibril architectures. Finally, MnO_2 nanowires were investigated for their charge storage mechanism using ICP-AES to detect Li ion to Mn ion ratios during the charging and discharging process. Their charge storage process was found to differ depending on whether the electrolyte solvent used was aqueous or organic. These projects all help advance energy storage devices well beyond their current status as bulky, heavy energy sources toward their prospective use as light weight, flexible, micro- power sources.

ELECTROCHEMICAL SYNTHESIS, TRANSFORMATION, AND CHARACTERIZATION OF MNO_2 NANOWIRE ARRAYS FOR SUPERCAPACITOR ELECTRODES

By

Jonathon Duay

Dissertation submitted to the Faculty of the Graduate School of the
University of Maryland, College Park, in partial fulfillment
of the requirements for the degree of
Doctor of Philosophy
2013

Advisory Committee:
Professor Sang Bok Lee, Chair
Professor Bryan Eichhorn
Professor Janice Reutt-Robey
Professor YuHuang Wang
Professor Gary Rubloff

Dedication

This work is dedicated to my wife, Charlotte, for her willingness to separate herself from everything she had known to join me on this endeavor.

Acknowledgements

First and foremost, I thank my advisor, Professor Sang Bok Lee, for his guidance throughout my graduate career. I truly appreciate his confidence in my knowledge and my abilities even when I had my doubts.

I would also like to thank Ran Liu, who helped me greatly when I was first beginning. There is no way I would have gotten this far without him. I thank Stefanie Sherrill for being a great companion at all of the random NEES-EFRC and ACS conference events. I thank Liz Nguyen for helping our group to become a cohesive unit even outside of the lab. I thank Dr. Kim for always encouraging me to be manlier ("Are you man?"). I thank Zhe Gui for always asking the toughest questions about my research. I thank Junkai Hu for his willingness to always go with me on the hunt for free food. I thank Lauren Graham for helping me understand what exactly goes on downstairs. I thank Eleanor Gillette for the random discussions involving anything and everything and for always willing to be my profreader. I thank Jaehee Song for her willingness to take on my project and know you will do well with it. I thank Nikki Schneck for our brief discussions about our love affair with analytical chemistry. I thank Professor Gary Rubloff for access to his group's toys (instruments) and for always encouraging me to think bolder about my experiments. I also thank the whole Rubloff group for allowing me to usurp some of your expertise. Sitting in on those joint group meetings, I realized that your knowledge base is on a completely broader plane than mine.

Finally, I thank my family who has provided great support during this process and I apologize for making you believe that I make tiny microscopic batteries.

Table of Contents

Table of Figures

Chapter 1: Introduction to Current MnO_2 Electrochemical Capacitor Research

Due to the effects of global climate change, there is an increasing need to alleviate the world's dependence on greenhouse gas producing fossil fuels. This has led to the increased emphasis on renewable energy sources such as wind, solar, and geothermal power. However, the energy produced from these sources needs to be stored and transported efficiently to the consumers without fluctuations in the amount of power supplied or energy delivered.

Electrochemical energy storage devices such as batteries and capacitors have been a safe and reliable way to store and transport energy for over a century. However, these devices will need to be improved in order to meet the demands of future portable electronics, for example plug-in or hybrid electric vehicles or other electric machinery or instruments.[1] They will also need to be in flexible packaging in order to power future flexible electronics such as wearable electronics, paper-like electronics, and flexible biomedical devices. All of these applications require high energy and high power devices with small masses and small volumes. Therefore it is important that the materials for these devices will have both high gravimetric and high volumetric energy and power densities.[2]

Currently, lithium ion batteries[3-13] and electrochemical capacitors[1, 3, 14-16] are at the frontier of the this research effort, as they play important roles in our daily lives by powering numerous portable consumer electronic devices (e.g., cell phones, PDAs, laptops) and even current plug-in hybrid electric vehicles (PHEVs).

However, these current rigid, bulky electrochemical energy devices do not have enough energy density at high charge/discharge rates with good cycle abilities to satisfactorily energize current and future portable power applications for extended periods of time. Therefore, an important objective for today's scientists is to technologically advance electrochemical energy storage devices to the point where they can effectively uptake and deliver high energies at high power demands while realizing low masses and small volumes. In addition, these devices will need to be quite flexible as future electronics are showing signs of becoming rather elastic.

As mentioned, lithium-ion batteries and electrochemical capacitors are sharing the spotlight when it comes to current research on electrochemical energy storage devices. The reason for this is that they complement each other nicely. Lithium-ion batteries, which have been more heavily researched to date, are known for their high energy densities. However, their power density is only moderate. Whereas, electrochemical capacitors, also known as supercapacitors, have high power densities and moderate energy densities. In other words, to use an electric car as an example, lithium-ion batteries can provide the energy to go long distances but with slow acceleration while electrochemical capacitors can provide fast acceleration but with little energy to go very far. This can be seen visually in the Ragone plot found in Figure 1.1 where the energy density, both gravimetric and volumetric, of common complete electrochemical energy storage devices is plotted versus their power density.

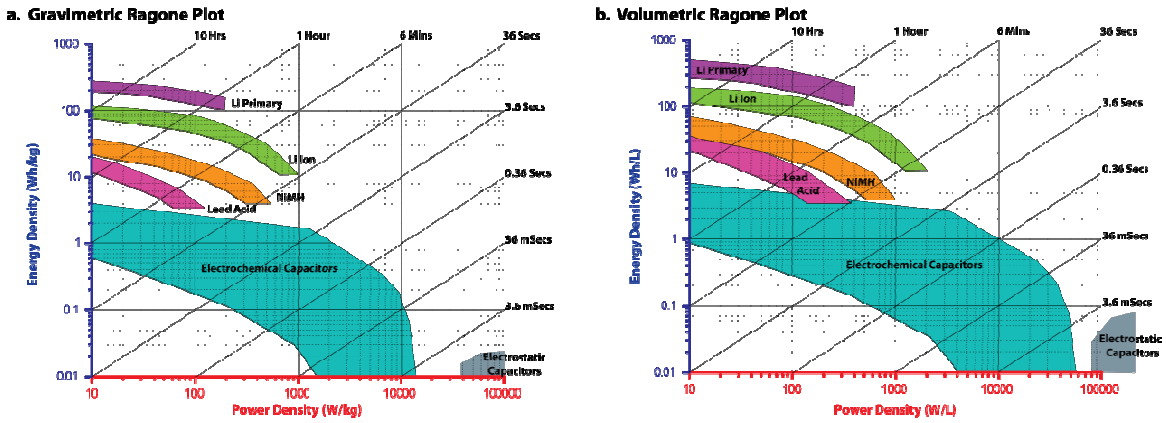

Figure 1.1. Gravimetric and Volumetric Ragone plots

Energy versus power density plots comparing different energy storage devices in terms of a. Gravimetric and b. Volumetric aspects. Graph adapted from Simon *et al.*[1]

Therefore, one of the goals of the research presented here is to increase the energy density of supercapacitors in order to produce devices that can provide high power over an extended period of time.

1.1 What is an Electrochemical Capacitor?

As can be learned in an introductory physics course, a traditional capacitor is simply two metal plates sandwiching an insulating dielectric layer as represented by Figure 1.2. Applying a potential difference between the plates results in a positively and a negatively charged plate.

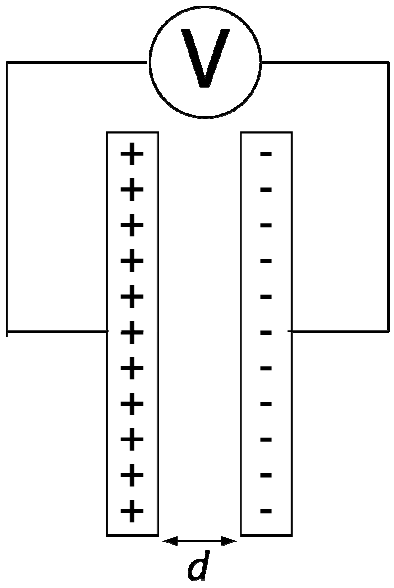

Figure 1.2. Electrostatic Capacitor Graphic

Graphic depicting two parallel plates separated by a dielectric with a thickness, d, where a potential, V, is applied

As this potential, *V*, is increased, the amount of charge, *q*, increases linearly. This characteristic d*q*/d*V* constant is known as capacitance, *C*, and its unit of measurement is the farad, F, which represents a coulomb per volt. The magnitude of this metric of capacitance, *C*, then can be considered using the following equation:

1

where is the relative permittivity constant of the dielectric layer or dielectric constant,

is the vacuum permittivity constant, *d* is the distance between the charged plates (thickness of the dielectric layer), and *A* is the overlapping area of the plates. This

capacitance can be directly correlated with the energy, E, through the following equation:

$$E = \frac{1}{2} CV^2 \qquad 2$$

where V represents the voltage applied. Therefore, one can improve the capacitance and thus the energy by either increasing the area of the plates or reducing the thickness of the dielectric area.

As opposed to this traditional capacitor, electrochemical capacitors or supercapacitors contain an electrolytic solution of ions between the electrodes instead of the dielectric layer. This results in essentially two capacitors in series with the capacitance being stored between each electrode's surface and the electrochemical double layer of the electrolyte as seen in Figure 1.3. Accordingly, devices utilizing this type of charge storage are called electrochemical double layer capacitors (EDLCs).

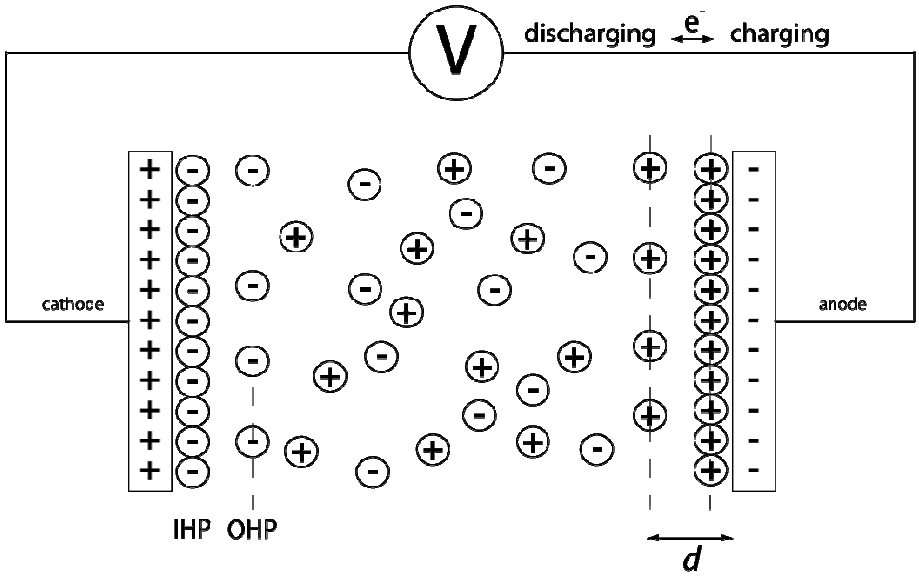

Figure 1.3. Electrochemical Capacitor Graphic

Schematic of an electrochemical double layer capacitor where *d* is the thickness of the double layer, while IHP and OHP stand for the inner and outer Helmholtz plane, respectively

Since the charge separation distance, *d*, for these devices is much smaller than the dielectric layer thickness of electrostatic capacitors, equivalent to the thickness of the double layer (<3 Ångstroms for a 0.3 molar electrolyte in aqueous solution *versus* tens of nanometers for even the best dielectric),[17, 18] much higher capacitance values can be obtained which is the reason why these capacitors are often called 'super-' or 'ultra-'capacitors.

Traditional materials for these devices have included high surface area porous carbons such as carbon nanotubes, onions, and fibers as well as the most utilized EDLC material, activated carbon.[16] These materials can achieve specific surface areas greater

than 1500 m^2 g^{-1}.[1, 19] Due to their superior surface areas and small charge separation distances, EDLCs can achieve volumetric capacitances >100 F cm^{-3} which are 1000 times larger than those obtained by even the most advanced electrostatic capacitors (0.1 F cm^{-3}).[18, 20]

1.1.1 Pseudocapacitance

It was first observed in 1971 by Trasatti et al. that RuO_2 films cycled in sulfuric acid exhibited capacitance-like behavior.[21] The capacitance values obtained for these films were comparable to EDLCs.[22] The high capacitance for these films was thought to be achieved by a fast reversible charge transfer between the electrolyte double-layer and the electrode. However, unlike a battery, where this type of charge transfer also occurs, the voltage profile during galvanostatic charging changes linearly with the amount of charge accumulation (dq/dV is constant). Since this discovery, other metal oxides and even conductive polymers have been observed to have this capacitance-type behavior, which has been termed "pseudo-" capacitance as the origin of the capacitance does not come from traditional charge separation. This type of charge transfer process, also called a faradaic reaction, allows additional surface or near surface atoms to be electrochemically active through adsorption and insertion reactions which contribute to the overall capacitance. This mechanism can be seen in Figure **1.4** below.

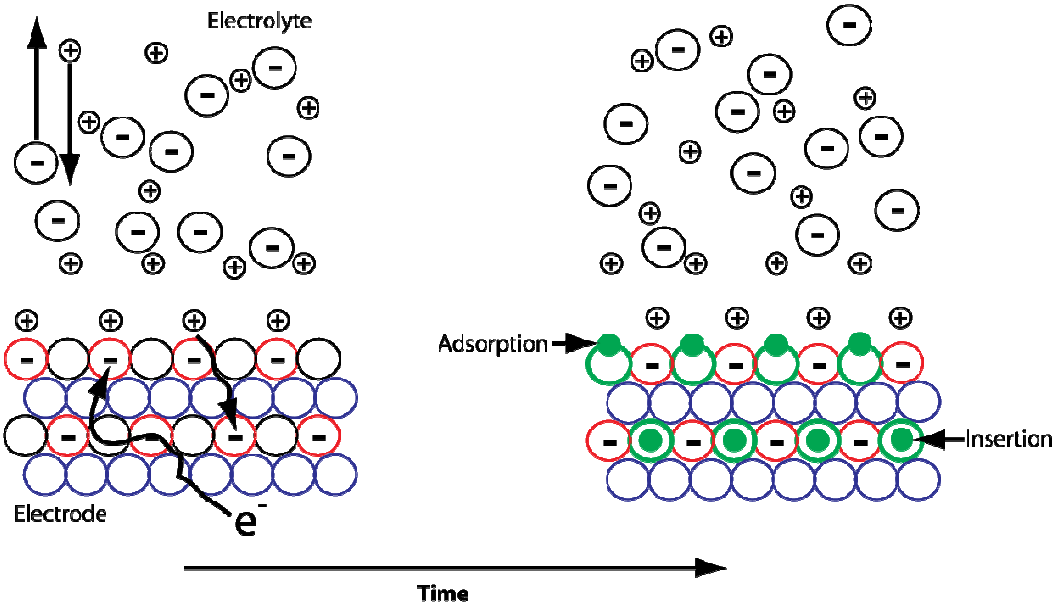

Figure 1.4. Pseudocapacitive Charge Storage Process

Illustration of the proposed cation adsorption and insertion during charging of a pseudocapacitive material

Owing to this charge storage behavior, these pseudocapacitors can reach gravimetric capacitances greater than 1200 F g^{-1} which is considerably higher than even the best EDLCs (300 F g^{-1}).[1, 23-25] Also, their volumetric capacitances can be, in principle, 10 to 100 times larger than those for EDLCs.[26] Conductive polymers[3, 26] such as polypyrrole, polyaniline, and polythiophene along with transition metal oxides such as the mentioned RuO_2[27, 28], Fe_3O_4[29, 30], V_2O_5,[31, 32] and MnO_2[33] are the typical materials used for these devices.

For conductive polymers, the faradaic process resulting in their capacitance-like behavior involves the insertion and de-insertion of counter-ions through their polymer matrix. Although injection of electrons into their polymer backbones is considered

metal-like and thus a charge-separation or EDLC-type behavior, faradaic electrochemical changes such as radical cation and anion formations are observed and thus conductive polymers are labeled as pseudo-capacitive materials.[26]

On the other hand, metal oxide's charge storage behavior is still debated but it is considered either a surface ion adsorption mechanism or a bulk ion insertion mechanism.[34-36] For example, the mechanism of charge storage for RuO_2 in H_2SO_4 follows the following chemical reaction:[37]

$$RuO_2+xH^++xe^- \leftrightarrow RuO_{2-x}(OH)_x$$

where protons are thought to either adsorb on the surface or insert into the bulk while ruthenium's oxidation state changes between Ru^{4+} and Ru^{2+}.

Whether it is considered an adsorption mechanism or that of an insertion mechanism, there is considered to be a redox reaction taking place near the surface affecting the valence state of these elements.

1.1.2 Why Nano?

Due to the fact that pseudocapacitive charge storage is thought to take place within tens of nanometers from the surface, decreasing a pseudocapacitive materials particle size should increase the surface active sites while decreasing the bulk inactive material. This has indeed been shown in the literature.[25, 34, 38, 39] For example, Srinivasan et al. showed that electrospun V_2O_5 nanofibers had the highest capacitance values when annealed at 400°C.[31] This was due to this sample having the highest BET specific surface area of any of the other annealed samples.

Another reason for nanostructuring is the buffering of stresses involved during the electrode cycling. For pseudocapacitors, where there is a redox reaction, there is a change in the volume of the crystal structure during the charging and discharging process which results in stresses that build up in the bulk as is illustrated by Figure **1.5**a. Ultimately, these stresses can result in cracks being formed in the electrode potentially disconnecting regions of the material from the electronic circuit. These stresses can be buffered by mitigating the amount of bulk material and creating void spaces between the nanostructures that allow the expansion of this material as seen in Figure **1.5**b. Owing to this, nanostructuring has resulted in better cycle ability performance of nanostructured materials versus their bulk counterparts.

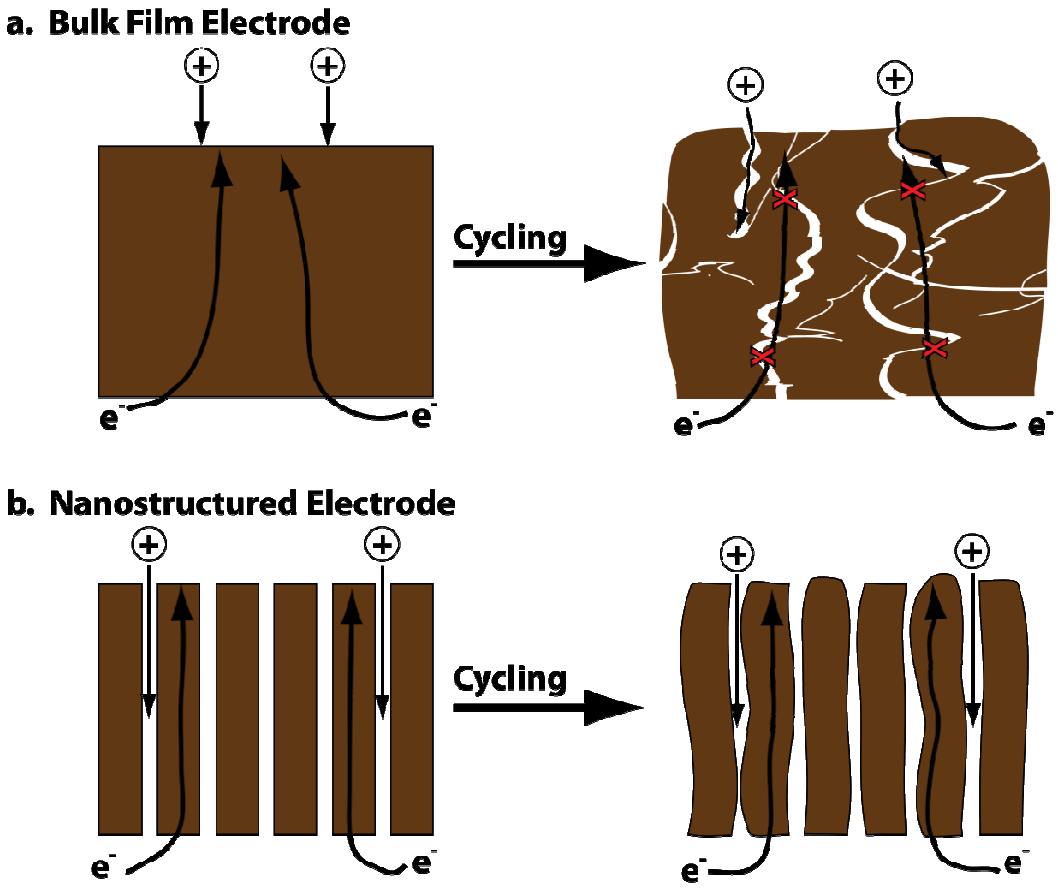

Figure 1.5. Bulk versus Nano Electrodes

Depiction of (a) bulk film and (b) nanostructured electrode before and after cycling

In addition, due to the increase in electrolyte accessibility to the surface and short diffusion distances of ions into the bulk, nanostructured electrodes can achieve superior power densities. This has been shown when comparing nanostructured and thin film electrodes with bulk electrodes.[40-42] Also, nanotubes have shown to have higher capacitance numbers compared to nanowires due to their additional surface area and thin walls supporting fast ion diffusion.[43]

Although nanostructuring has been shown here to improve capacitance behavior for materials, it can also have some unwanted side effects.[44] Due to the increased specific surface area, nanostructured materials' stable voltage cycle windows can be smaller when compared to bulk as a result of increased side reactions with the electrolyte. Nanomaterials also tend to have a low packing density resulting in low volumetric capacitances that may not be practical for certain applications. Therefore, all of the modified properties caused by nanostructuring must be taken into account before one can assume that nanostructuring is the best decision.

1.1.3 Calculating Capacitance

Capacitance is the most common metric for comparing capacitive materials. This metric for pseudocapacitor materials is obtained either by galvanostatic or cyclic voltammetry which are common testing techniques for all capacitors. In galvanostatic voltammetry (GV), a constant charging or discharging current is applied while the voltage is monitored. For capacitors, this results in a linear curve for voltage *versus* time like the one found in Figure **1.6**a which is in sharp contrast to the typically nearly constant voltage GV curves obtained for batteries.

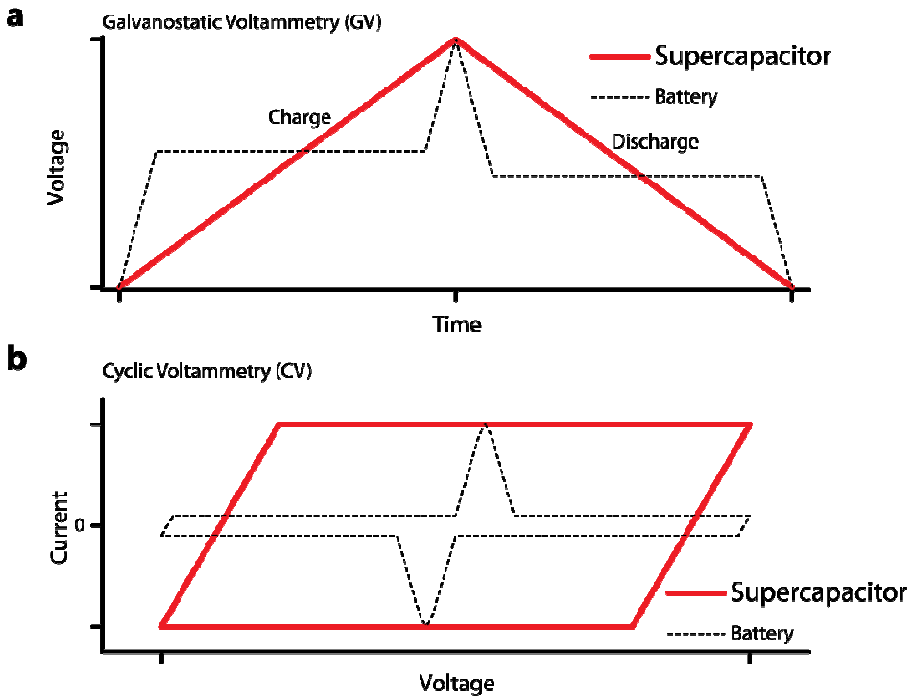

Figure 1.6. Ideal Galvanostatic and Cyclic Voltammetry Curves

Curves representing ideal supercapacitor and battery behavior during (a.) galvanostatic and (b.) cyclic voltammetry testing

The main metric, capacitance (*C*), is then obtained using the following equation:

$$C = \frac{Q}{V} \qquad (3)$$

where *Q* stands for the charge in coulombs and *V* stands for potential in volts. The unit used for this is a farad, which represents a coulomb per volt. For GV, equation **3** is rearranged into the following equation as $Q = it$:

$$C = \frac{it}{V} \qquad 4$$

where *i* stands for the current applied, *t* stands for the charging or discharging time, and *V* is the voltage window used.

In cyclic voltammetry (CV), voltage is changed at a constant rate, also called a scan rate (*v*), while current is monitored. For electrochemical capacitors, this usually results in a square shaped current *versus* voltage curve like the one found in Figure **1.6**b again in sharp contrast to the peak-shaped CV curves obtained for batteries. Capacitance using this method can be found by rearranging equation **3** into the following:

$$C = \frac{\int i\, dV}{v} \qquad 5$$

where the capacitance (*C*) is found by taking the area under the charging or discharging current (*i*) *versus* voltage (*V*) curve and dividing by the constant scan rate (*v*) in volts per second.

Reports quoting capacitances obtained from these methods should always indicate the current or scan rate (power level) used for GV or CV respectively. This is because at low current or scan rates, these materials may show high capacitances, but at more practical powers the material may fail to demonstrate a practical capacitance. Therefore, no capacitance value should be compared with another without the accompanying power level at which they were obtained.

1.1.4 Important Observations

In utilizing both GV and CV characterization, the voltage window is an input function. In other words, the voltage is chosen by the experimenter. This window is chosen by the careful observation of previous wide voltage current versus potential cyclic voltammetry graphs at moderately fast scan rates of the material, which is depicted in Figure 1.7. For ideal supercapacitors, this window should not contain well-defined slow redox processes or irreversible electrochemical reactions either from the material or from the solvent. Thus, all reactions in the electrochemical stability window should be fast and reversible.

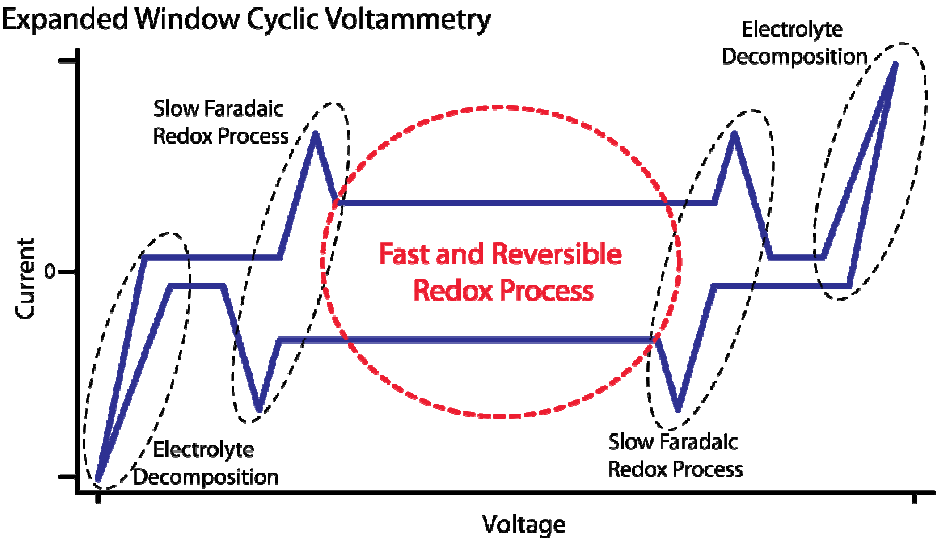

Figure 1.7. Choosing Supercapacitor Potential Window

Illustration representing a typical extended window cyclic voltammetry test at moderately fast scan rates to determine ideal electrochemically reversible potential window (Note: At slower scan rates, redox peaks in the chosen reversibility window may appear)

For conductive polymers this electrochemical stability window is shown to be around 1.2 V for poly (3,4-ethylenedioxythiophene) (PEDOT)[43] and 1.0 V for both polypyrrole[45] and polyaniline.[46] For metal oxides, the potential window ranges from 1.4 V for RuO_2[26] to around 1.0 V for MnO_2[34, 35] to a very small 0.5 V for NiO.[47]

Capacitances obtained using these electrochemical stability windows are usually normalized with respect to the material's mass in order for comparisons to be made. Theoretical maximums for these specific capacitances, $C_{Spec,Max}$, can be obtained using the following equation:

$$C_{Spec,Max} = \frac{zeN_A}{MV} \qquad 6$$

where z represents the number of electrons inserted per material unit, e represents the charge of an electron, N_A is Avogadro's number, M is the molar mass of the material, and V is the voltage window. It should be noted that this theoretical maximum specific capacitance only includes capacitance associated with pseudocapacitance; whereas, materials with large specific surface areas can achieve specific capacitances higher than these theoretical maximums due to the additional double layer capacitance. For conductive polymers, z represents the maximum counter ion doping level per polymer unit, which if exceeded results in a significant decrease in the polymer's conductivity.[48] For PEDOT, z is 0.33 and results in a maximum specific capacitance of 190 F g^{-1} for this polymer at a 1.2 V potential window.[49] Other maximum specific capacitances can be calculated as 1110 F g^{-1} for MnO_2 and 2580 F g^{-1} for NiO assuming one electron transfer per formula unit.

An important point to be made here is that NiO may seem to be near 2.5 times as good as MnO_2; however, great caution should be used when observing these numbers as NiO's large theoretical capacitance comes from its small 0.5 V potential window (MnO_2's is around 1.0 V). Equation **2** shows us that this potential window is exponentially important when it comes to energy. In fact, if the theoretical maximum energy density of MnO_2 and NiO is calculated using equation **2** (substituting specific capacitance for capacitance), 154 Wh kg^{-1} for MnO_2 and 179 Wh kg^{-1} for NiO is obtained. So what appeared to be a great advantage for NiO is marginal at best.

Another pit fall that may come about for a researcher is the interpretation of specific capacitance values from a so-called "three-electrode" or "half-cell" test *versus* specific capacitance values from a "full-cell" or "two-electrode" test. Adjusting equation 4 in order to calculate specific capacitance, C_{Spec}, the following equation is obtained:

$$C_{Spec} = \frac{it}{Vm} \qquad 7$$

where *m* here represents mass.

Traditionally, supercapacitors were tested utilizing the "two-electrode" test where both the cathode and the anode were of the same material. When applying a voltage here it refers to the potential difference between the anode and cathode. Therefore, any change in the cathode must be accompanied by an equal but opposite change in the anode, including potential changes. Accordingly, for GV testing, the anode's and cathode's respective voltage windows are half of the voltage window of the full cell which is depicted by Figure **1.8**a. Two electrodes are considered active material here;

therefore the sum of both masses is included in any gravimetric metric.

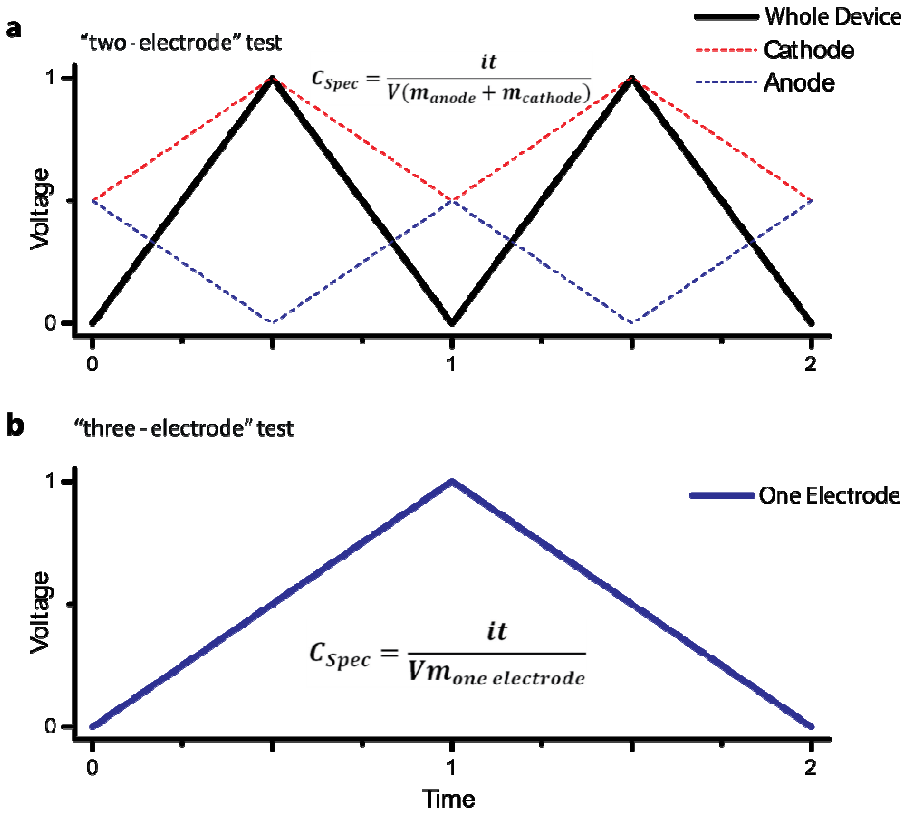

Figure 1.8. Two-electrode vs. Three-electrode GV Curves

Galvanostatic voltammetry (GV) curves typical of (a.) two-electrode and (b.) three-electrode testing

On the other hand, the "three-electrode" test involves the material of interest being labelled as the working electrode, an electrode of known potential as the reference electrode, and a relatively large area electrode that only has benign electrochemical reactions as the counter electrode. In this case, the analysis is focused only on the working electrode as the potential of this electrode is directly monitored by a reference

as seen in Figure **1.8**b. The working electrode here is cycled utilizing the same potential window as that for the "full-cell" or "two-electrode" test. This means that the electrode functions through both the cathode and anode voltage windows. This means that for equation 11, the time during charging and discharging for the GV is going to take twice as long, while the mass will be half as much compared to the "two-electrode" test resulting in specific capacitances that are four times greater.

This can also be shown mathematically. The total capacitance, C_{Total}, in the "two-electrode" test can be calculated using the following equation modified from the equation for capacitors in series:

$$\frac{1}{C_{Total}} = \frac{1}{C_{Cathode}} + \frac{1}{C_{Anode}} \qquad 8$$

where $C_{Cathode}$ represents one electrode and C_{Anode} the other. Since each reaction at the cathode must have an equal but opposite reaction at the anode, the capacitances for each must be equal. This results in the following equation:

$$\frac{1}{C_{Total}} = \frac{1}{C_{Cathode}} + \frac{1}{C_{Cathode}} = \frac{2}{C_{Cathode}} \qquad 9$$

This can be rearranged and solved for C_{Total} giving the following:

$$C_{Total} = \frac{C_{Cathode}}{2} = 0.5\, C_{Cathode} \qquad 10$$

Thus, the total capacitance is half what it is at either electrode. Applying this result to the specific capacitance results in the following equation where the mass of each electrode is the same:

$$C_{Spec,Total} = \frac{C_{Total}}{mass_{Total}} = \frac{0.5\ C_{Cathode}}{2\ mass_{Cathode}} = 0.25\ C_{Spec,Cathode} \quad (11)$$

This result indicates that in the "two-electrode" test, the total specific capacitance is only a fourth what it is for each electrode. This again supports the fact that the specific capacitance obtained from the "two-electrode" test is a fourth of what it is for the "three-electrode" test. Therefore, all specific capacitances in this document from the "two-electrode" test are multiplied by a factor of four in order for the reader to make accurate comparisons.

1.1.5 Symmetric vs. Asymmetric

As seen in equation 11, the voltage window of these devices has an exponential effect on their energy density. Traditional pseudocapacitors have consisted of an anode and a cathode with the same material. These types of capacitors are called symmetric capacitors. Most materials used for symmetric pseudocapacitors have limited voltage windows of less than 1.2 V and some as low as 0.5 V in aqueous electrolytes as indicated on page 15. Carbon-based EDLCs have maximum potential windows of 1.23 volts in aqueous solutions which can be increased to >2.5 volts in organic solvents.[1, 19]

Therefore, one way to improve the pseudocapacitor voltage windows is by using organic electrolytes; however, due to their lower dielectric constant, ε_r, utilization of organic solvents results in lower capacitances.[19, 50] Also, since voltage windows for pseudocapacitors are chosen between slow redox peaks as seen in Figure **1.7**, expansion of the voltage window for these types of capacitors can be limited.

In order to bypass the problems associated with trying to increase the potential window for symmetric pseudocapacitors is to create asymmetric pseudocapacitors. In this case, the cathode and anode are different materials with different reversible electrochemical potential windows. These devices maintain the high capacitances associated with pseudocapacitance, while increasing the voltage window. A schematic for an ideal two volt device and the behavior of its cathode and anode material during a typical CV scan can be found in Figure **1.9**.

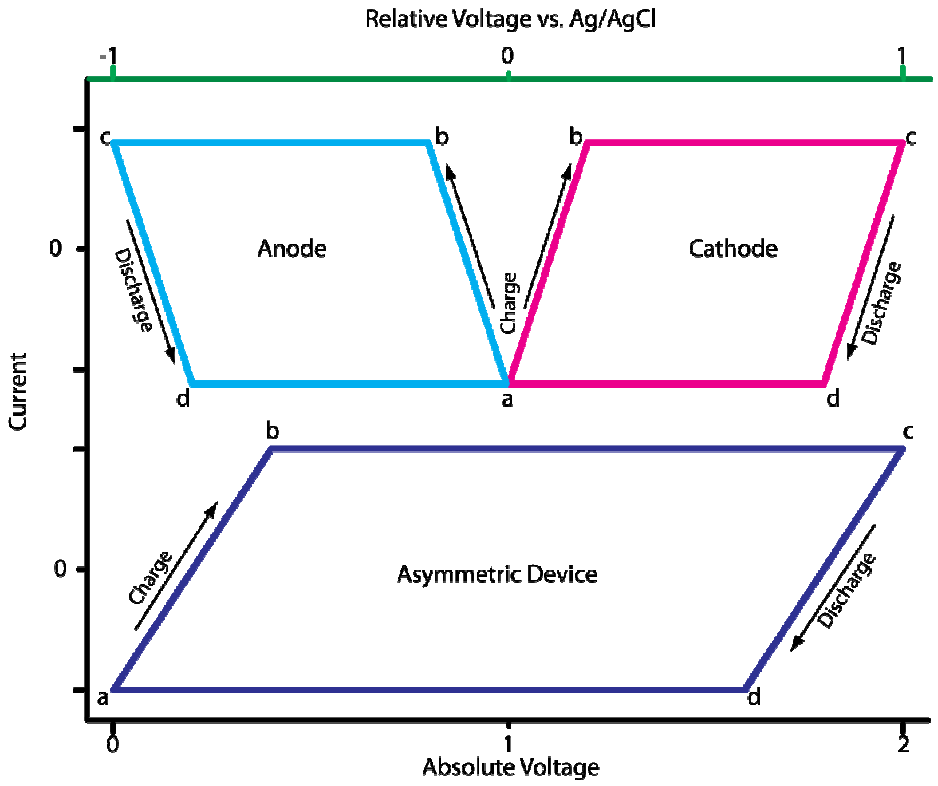

Figure 1.9. Representation of an Asymmetric Device

Illustration of cyclic voltammetry testing for an asymmetric device noting the anode and cathode windows

Owing to this, asymmetric supercapacitor devices utilizing a variety of combinations of redox materials, conductive polymers, and EDLC carbon materials have been prepared.[51-55] The material for the anode and cathode are chosen carefully so that the total electrochemical stability window (cathode potential window plus the anode potential window) is maximized. MnO_2, RuO_2, TiO_2, NiO, and other metal oxides are typically chosen as cathodes with carbon-based materials usually selected as anodes; [53, 56-58] while conductive polymers are able perform in both regards.[52, 59] This research has led to asymmetric devices with voltage windows of two volts in aqueous electrolytes,

which is greater than water's theoretical electrochemical stability window according to water's Pourbaix diagram.[60]

1.2 MnO_2 Materials for Supercapacitors

As noted on page 7, ruthenium oxide was the first redox pseudocapacitive material studied for supercapacitor applications. This material has many great properties for a supercapacitor material such as a large (1.2 Volt) potential window, high specific capacitance, high conductivity, and good electrochemical stability.[37] However, these great properties are offset by its high cost, environmental toxicity, limited earth abundance, and its utilization of a strongly acidic electrolyte. Therefore, there is a need to find another material that can achieve or approach the same good properties of RuO_2 without including as many of the bad properties as possible.

Oxides of manganese are perhaps the best choice for this substitution. Manganese is the twelfth most abundant element on earth[61] and is less toxic than the ever-present metals of nickel, iron, and copper.[62] It is also less expensive than other competitive energy storage materials such as CoO_2, RuO_2, NiO, or V_2O_5.[63] In addition, MnO_2 has a large 1.0 V electrochemical potential window (typically between 0 and 1 V vs. Ag/AgCl) and a high theoretical specific capacitance (1110 F g^{-1}) in a neutral aqueous electrolyte.[64]

Furthermore, manganese oxides also have a long history as energy storage materials. In the 1860s, Georges Leclanche developed the alkaline cell based on the electrochemistry of Zn and MnO_2.[65] Owing to this, batteries containing MnO_2 are by

far the most common energy storage device on the market today thus showing this material's practical ability to be incorporated in affordable and mass produced devices.

1.2.1 Supercapacitor Charge Storage Mechanism

Recently, manganese oxides have been applied to supercapacitor applications. In 1999, Goodenough et al. first discovered manganese oxide's had a capacitive behavior in a neutral aqueous KCl electrolyte.[35] This amorphous material was shown to deliver a specific capacitance of 200 F g^{-1} and an areal capacity (q cm^{-2}) of 3.8 C cm^{-2} as compared to 11.1 C cm^{-2} for RuO_2. The charge storage mechanism was thought to be an adsorption of the potassium ion. The ion was proposed to bind to three surface oxygen atoms which resulted in its low capacity compared to RuO_2.

However, this limitation to the charge storage mechanism was modified when researchers were able to obtain specific capacitances for MnO_2 thin films that approached values for RuO_2 at 700 F g^{-1} and even higher at 1380 F g^{-1}.[34, 36] Thus, the mechanism for the charge storage for MnO_2 in aqueous electrolyte has been and is still being further investigated, including by our group as can be seen on page 104 and 128. The main arguments are whether there is ion insertion into the bulk or if there is only ion adsorption on the surface and whether this active ion is a proton or the cation from the solution.[34-36, 66, 67] The best characteristic mechanism is depicted by the following reaction:

$$MnO_2 + aH^+ + bC^+ + (a+b)e^- \leftrightarrow MnOOH_aC_b$$

where C^+ represents the alkali metal cations in the electrolyte. As mentioned, a and b's contributions are disputed, and there is also an argument whether the overall reaction is only at or within tens of nanometers from the surface. Although the exact mechanism is still disputed, there is a common agreement that the charge is stored at or near the surface which is the reason for its capacitive-shaped rectangular CV curve.

1.2.2 Factors Affecting Capacitance

Manganese oxide's capacitance performance can be controlled by a variety of parameters including its morphology (*i.e.* crystallinity, size, shape, and micro-structure), chemical state (*i.e.* number of bound waters, valence state), and electrode composition (*i.e.* thickness of electrode).

As for crystallinity, MnO_2 materials with well defined crystallinity tend to have higher conductivities but at the expense of lower surface areas.[68] Also, crystallinity is most times adjusted by annealing which affects the amount of bound water molecules in the MnO_2 material.[69] It is thought that the more physically and chemically bound water molecules to the material results in a larger ionic conductivity and the maximum number of these water molecules per MnO_2 unit is found in the un-annealed state. Therefore, an optimization between ionic conductivity, electronic conductivity, and surface area must be found.

As MnO_2 has many polymorphs (α-,β-,γ-, and δ-MnO_2), where the MnO_2 octahedral units are ordered into different morphological structures, different capacitance performances can be observed for each.[70] These structures are represented schematically in Figure 1.10; whereas, α-MnO_2 contains 2x2 tunnels, β-MnO_2 has 1x1

tunnels, γ-MnO_2 is spinel-phase with 3-D tunnels, and δ-MnO_2 is layered sheets of octahedral MnO_2.[71] Among them, δ-MnO_2 has the highest specific capacitance versus BET surface area owing to its two-dimensional tunnel structure.[72]

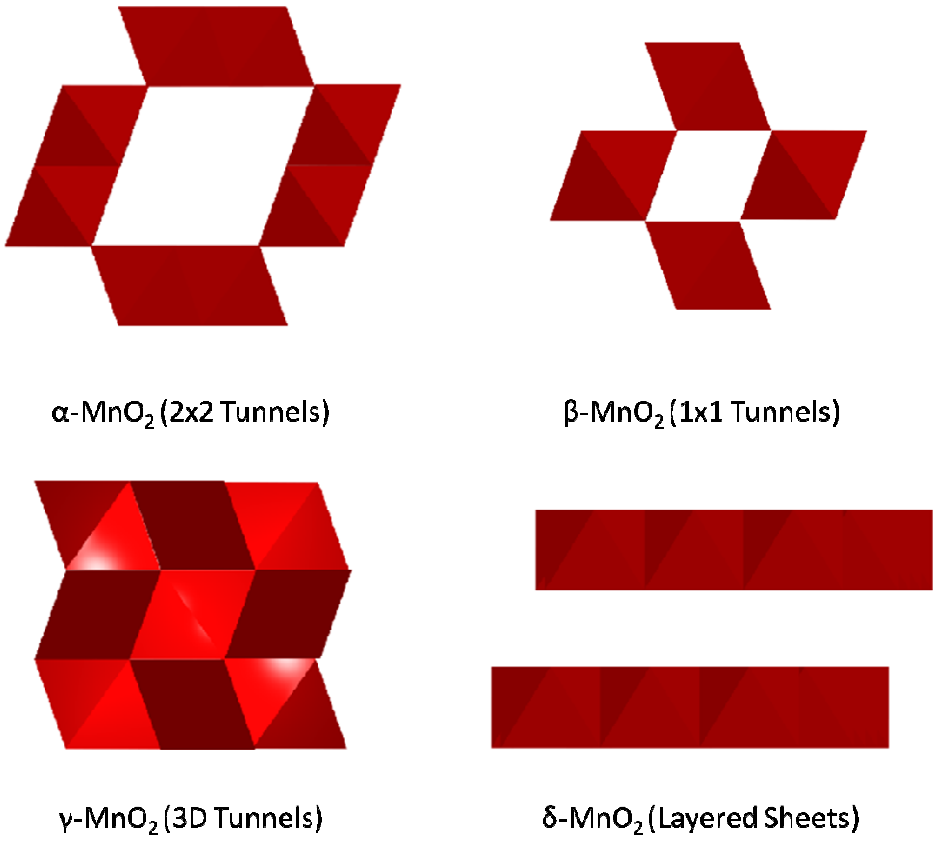

Figure 1.10. Schematic of Manganese (IV) Oxide Polymorphs

By reducing the size of MnO_2 materials, scientists have been able to increase its specific capacitance. Owing to this fact, nanostructuring of MnO_2 has been researched thoroughly and has shown vast improvements in specific capacitance, power capability, and cyclic ability when compared to its bulk counterpart.[73] This is due to the increase in specific area which allows greater active vs. inactive material resulting in more and

faster proton or cation adsorption and/or insertion per unit mass. In addition, these nanostructured materials allow void space where the material can expand and contract during cycling resulting in greater cycle ability.

The shape of the MnO_2 material also affects the capacitive performance. For nanostructured MnO_2, 0-D (nanospheres[74]), 1-D (nanorods[75] or nanowires[76]), 2-D (nanoflakes[77]) and 3-D nanostructures (porous nanogels[78]) have been produced. Among these, one-dimensional nanostructures are thought to be the most promising as they allow a lot of ion access points at their surface while maintaining good electronic connectivity along their length which is schematically shown in Figure **1.11**.[37]

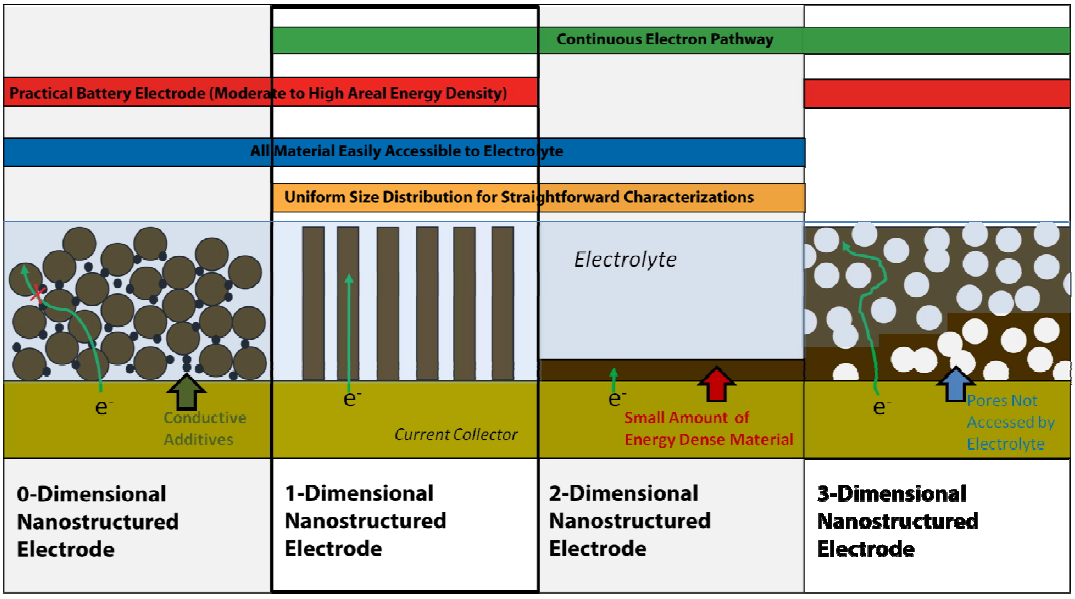

Figure 1.11. Dimensionality of Nanostructured Electrodes

Schematic representing the favorable properties of nanomaterials with different dimensionality (0-D, 1-D, 2-D, and 3-D).

Thickness of the electrode is also of concern as additional material can add to the overall capacitance but at the expense of the specific capacitance due to manganese oxide's intrinsic low conductivity. For example, Belanger *et al.* were able to produce thin films (< 5 μm thick) that achieved a specific capacitance of 1380 F g^{-1}; however, their areal capacitance was only 0.018 F cm^{-2}.[34]

1.2.3 Ways of Improving Capacitance Behavior

It is thought that by composing MnO_2 electrodes with conductive components in the form of doping MnO_2 films,[79, 80] adding coatings to MnO_2 nanostructures,[40, 81, 82] and applying thin films of MnO_2 to conductive porous networks,[83-89] the thickness of the electrode can be increased without a severe drop in specific capacitance. These type of materials are called heterogeneous or hybrid nanomaterials and have been reviewed in detail by our group and others.[90, 91]

Another aspect of MnO_2 that affects its capacitive performance is its dissolution rate. This dissolution is typically represented by the following disproportionation reaction:

$$MnOOH \leftrightarrow MnO_2 + Mn^{2+} + OH^-$$

When reduced to the MnOOH state upon the cathodic sweep during cycling, Mn^{2+} can dissolve into the electrolyte resulting in low capacitance retention during extended cycling. Researchers have are trying to mitigate this dissolution behavior by adding preventative additives to the electrolyte,[92] and protective coatings on the MnO_2.[93, 94] These measures have resulted in materials with enhanced extended cycling performance.

Another way of improving MnO_2's performance is through hierarchical structures. Ionic pathways for protons or cations are needed in the MnO_2 material to promote fast diffusion of these ions to the surface active sites. This can be accomplished by nanostructuring the material to have high porosity. However, these highly porous nanomaterials must be connected together in some fashion to promote electronic conductivity. This can be accomplished through hierarchical nanostructures, where one length scale offers an efficient way of transporting electrons while the other scale offers a higher surface area for greater adsorption or access of ions as is depicted in Figure 1.12. Thusly, hierarchical nanostructures of MnO_2 nanostructures have been successfully synthesized.[95-97] These hierarchical nanostructures have shown to have superior capacitive performance *versus* their single-length scaled counterparts. This hierarchical nanostructuring is further detailed in the introduction in Chapter 4:

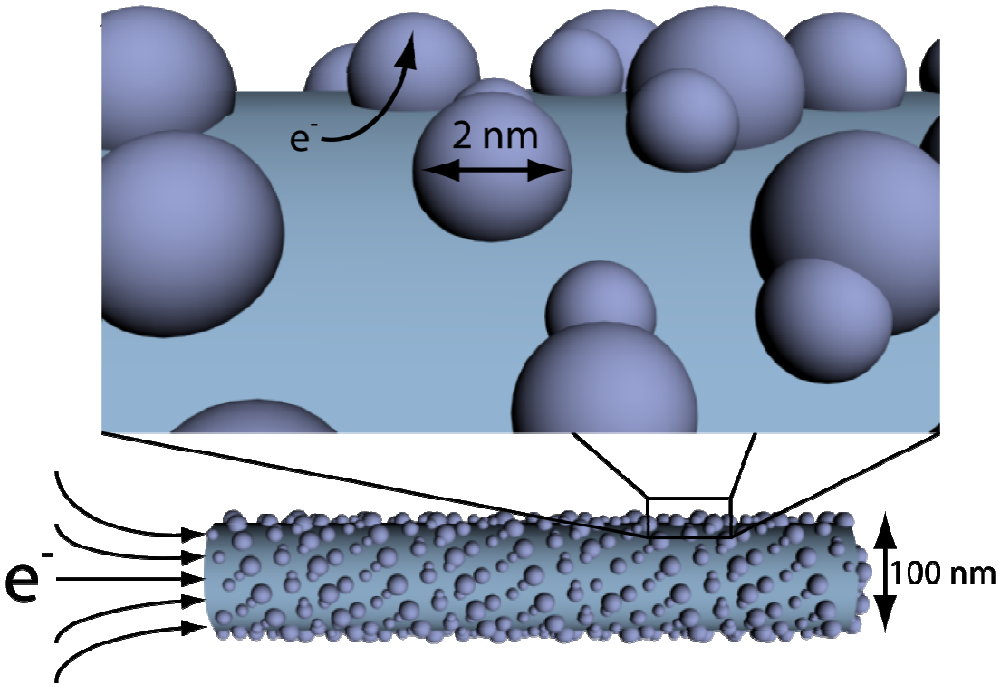

Figure 1.12. Schematic of a Hierarchical Structure

Scheme showing an imaginary hierarchical structure with the smaller electroactive material nanoparticles electronically connected to a larger one-dimensional nanostructure of the same material

1.2.4 Synthesis Methods for MnO_2

One of the great aspects of MnO_2 is its many synthesis methods. This makes it easier for this material to be functional for a variety of applications and morphologies. Owing to this, there are basically two types of products formed using these methods: powdered particles and thin films. Co-precipitation and hydrothermal methods tend to produce large amounts of MnO_2 particles in powdered form, while sol-gel and electrodeposited MnO_2 can be applied as thin films.

1.2.4.1 Powder Synthesis Techniques

Chemical synthesis or co-precipitation of MnO_2 is perhaps the most popular powder synthesis technique and was the method used by Goodenough et al. when they first discovered MnO_2's supercapacitor behavior.[35] This typically involves the mixing of potassium permanganate ($KMnO_4$) with manganese acetate ($Mn(CH_3COO)$) in water which results in the following redox reaction:

$$2Mn(VII)O_4^-{}_{(aq)} + 3Mn^{2+}{}_{(aq)} \rightarrow 5Mn(IV)O_{2(s)}$$

where the oxidant, Mn^{7+}, reacts with the reducing agent, Mn^{2+}, in water to produce a hydrated MnO_2 material.

While $KMnO_4$ is the main oxidant, other reducing agents include: manganese sulfate, potassium borohydride, sodium dithionate, in addition to conductive polymer monomers such as aniline and even polymers such as poly(3,4-ethylenedioxythiophene) (EDOT).[34, 82, 98, 99] These hydrated manganese oxide materials are usually amorphous as prepared, but typically become dehydrated α-phase MnO_2 when annealed.[64]

Another technique commonly used for MnO_2 synthesis, especially nanomaterials, is the hydrothermal method. The advantage for this method include the ability to control the morphology of nanostructures ranging from nanospheres to nanorods to nanourchins by adjusting parameters such as temperature, reaction time, and reactants used.[100] Various Mn sources can be used, from Mn^{2+} to Mn^{7+}; however, the majority of products made for supercapacitor applications are crystalline α-phase MnO_2.[100-103] These products tend to only differ by their nanomorphology.

Other techniques for creating powdered MnO_2 nanomaterials include ultrasonic and microwave-assisted techniques which provide low-temperature methods for producing nanostructure MnO_2 materials.[104-106]

Although the powdered products using the previous methods are promising, it is difficult to compare the products of each method as the synthesis procedures greatly affect the chemical and physical properties of their resultant materials. Another disadvantage of the powdered products is in the synthesis of the electrode. In order to connect this material to a circuit, it first must be pressed onto an electrode. This results in the need for heavy polymeric binders, which add weight to the electrode without any addition in energy storage. Also, as MnO_2 is known for its low electronic conductivity, a bulky conductive additive is needed to make sure the entire electrode is electrochemically active.

1.2.4.2 Thin Film Synthesis Techniques

A popular way to create MnO_2 thin-films is through the sol-gel technique which was first developed by Bach *et al.*.[107] Sol-gel offers advantages of homogeneous mixing of reactants, control over size and shape of products, and compatibility with thin film processes.[78] In this technique, organic acid (fumaric acid, $HO_2CCH=CHCO_2H$, produced the best results) is mixed with an alkali cation-MnO_4^- solution. A gel is then formed within 30 minutes of mixing. This first step in the gel formation is represented by the following reaction:

$$HO_2CCH=CHCO_2H + 2MnO_{4\,(aq)}^- + 8H_3O^+ \leftrightarrow 2CO_2 + HO_2C\text{-}COH + 2Mn^{3+} + 13H_2O$$

where HO_2C-COH is the chemical formula for glycoxylic acid. This aldehyde is then oxidized under basic conditions to oxalic acid (HO_2C-CO_2H) by the following reaction:

$$HO_2C\text{-}COH + 2Mn^{3+} + 3H_2O \leftrightarrow HO_2C\text{-}CO_2H + 2Mn^{2+} + 2H_3O^{+}$$

This formation of Mn^{2+} reacts rapidly with any excess MnO_4^- to produce MnO_2. The overall sol-gel MnO_2 formation is represented by the following reaction assuming a $KMnO_4$ manganese source:

$$3HO_2CCH{=}CHCO_2H + 10KMnO_4^- \leftrightarrow$$
$$[10MnO_2 + 3(KCO_2)_2 + 4KOH + 4H_2O]_{(gel)} + 6CO_2$$

This sol-gel process and variations of it have been used multiple times to create thin films of MnO_2 for energy storage applications though casting the gel onto current collectors.[78, 108, 109] Other synthesis using sol-gel have involved using anodized aluminum oxide (AAO) templates as a host for the gel followed by removal of the AAO producing MnO_2 nanowire arrays.[110] Typically, these materials are hydrated and amorphous, but become δ-phase MnO_2 upon annealing.[111]

Perhaps the best method for controlling the size, shape, physical and electronic connection, and mass loading of energy storage electrodes is electrochemical deposition which is reviewed in 1.3. Electrochemical synthesis of MnO_2 can be completed by either cathodic or anodic deposition.

For cathodic deposition, this usually involves the synthesis of $Mn(OH)_2$. This is first accomplished by applying a reducing voltage to an electrode in a Mn^{2+} aqueous solution which results in the production of OH^- from either the electrochemical reduction of water or a supplementary nitrate ion as the reactions depicted here:[112, 113]

$$2\ H_2O(l) + 2e^- \rightarrow H_2(g) + 2OH^-(aq)$$

$$NO_3^-(aq) + H_2O(l) + 2e^- \rightarrow NO_2^-(aq) + 2OH^-(aq)$$

The OH^- produced here then combines with the Mn^{2+} in solution to form $Mn(OH)_2$ depicted by the following reaction:[60]

$$Mn^{2+}(aq) + OH^-(aq) \rightarrow Mn(OH)_2(s)$$

The manganese hydroxide is then either electrochemically or thermally oxidized to MnO_2. Munichandraiah *et al.* has been the pioneer in this work even going as far as simultaneously depositing a MnO_2 cathode and anode utilizing the cathodic process to produce one electrode and the anodic process to produce the other electrode.[113]

Another cathodic process developed by Zhitomirsky *et al.* involves the direct electrochemical synthesis using the MnO_4^- ion represented by the following reaction:[114]

$$MnO_4^-(aq) + 2H_2O(l) + 3e^- \rightarrow MnO_2(s) + 4OH^-(aq)$$

where the morphology of the film is controlled by the concentration of MnO_4^- with high concentrations resulting in smooth films and low concentrations resulting in fibrous, porous films.[114-116]

Anodically deposited MnO_2 involves the oxidation of a Mn^{2+} species and heavily relies on the concentration and diffusion rate of this species thus more control over the morphology of the film is thought to be had. Chapman *et al.* was the first to utilize this method for supercapacitor applications.[36] This synthesis reaction is depicted by the following:

$$Mn^{2+}(aq) + 2H_2O(l) \rightarrow MnO_2(s) + 4H^+(aq) + 2e^-$$

Due to the controllability of this method, a wide-variety of morphologically controlled nanostructures and coatings on nanostructures has been produced by both template and template-free methods. These include nanostructures consisting of thin planar films,[36, 117-119] nanoflowers,[120, 121] nanowires,[86, 122, 123] porous films,[124] nanotubes,[122, 125] and nanoflakes[77] in addition to coatings on high surface area carbons,[126, 127] and colloid crystal templates.[128]

In addition to sol-gel and electrodeposition methods, other thin film synthesis methods for MnO_2 involve electrophoretic deposition and electrochemical oxidation of manganese metal.[129-132]

As will be mentioned in the next chapter, as these thin films tend to be directly deposited onto current collector either chemically or electrochemically, their electronic connectivity with the circuit is more ideal for electron transfer than the physically

pressed powdered electrodes. This leads not only to better performance of the material, but also a better ability to analyze materials for their fundamental properties. Therefore, these thin films, mainly electrochemically deposited films will be the main focus of remaining chapters.

1.3 Controlled Electrodeposition for the Synthesis of Nanostructures for Supercapacitors

As eluded to earlier in section 1.2.4.1, current energy storage electrodes consist of about 100 µm thick films[133] with 80-85% powdered electroactive material and 15-20% binder with large volume conductive additives (typical densities < 0.5 g cm^{-3}).[2] These electrodes are typically made by mixing the electroactive material, binder, and additives with an organic binder solvent into a slurry. The slurry is then coated or pressed onto a conductive foil and the solvent is combusted with a thermal oxidizer. A schematic of electrodes made this way can be found in Figure 1.13. This represents a problem, as promising nanostructured MnO_2 electroactive materials can have their high energy and volumetric densities negated by these electrode additives.

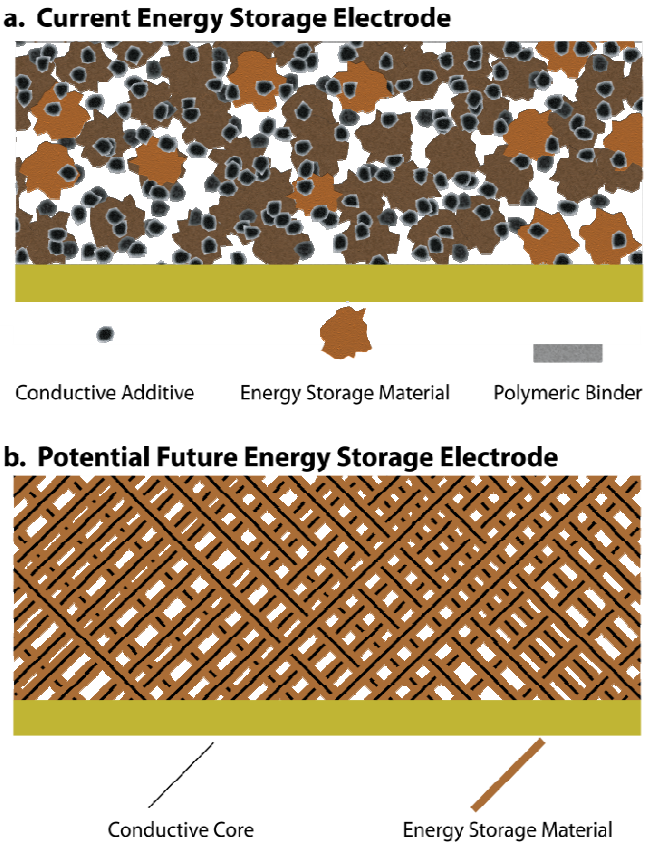

Figure 1.13. Current vs. Future Energy Storage Electrodes

Figure depicting a (a.) typical energy storage electrode and a (b.) proposed future electrode

Furthermore, since this electrode is just physically pressed onto the current collector, this can result in as much as 20% loss of the material's energy coming from the electrical contact resistance between the current collector and the electrode material due to contact surface imperfections that act as ohmic resistances as is illustrated in Figure 1.14.[134] Therefore, directly connecting MnO_2 through chemical means to a conductive substrate to create continuous contact between the electrode and current collector will reduce these ohmic losses. This can also result in higher gravimetric and volumetric

energy density devices not only by eliminating the need for these bulky additives but by also eliminating any electrochemically inactive materials that could result from dead spots associated with incomplete distribution of the conductive additives from these heterogeneously mixed materials.

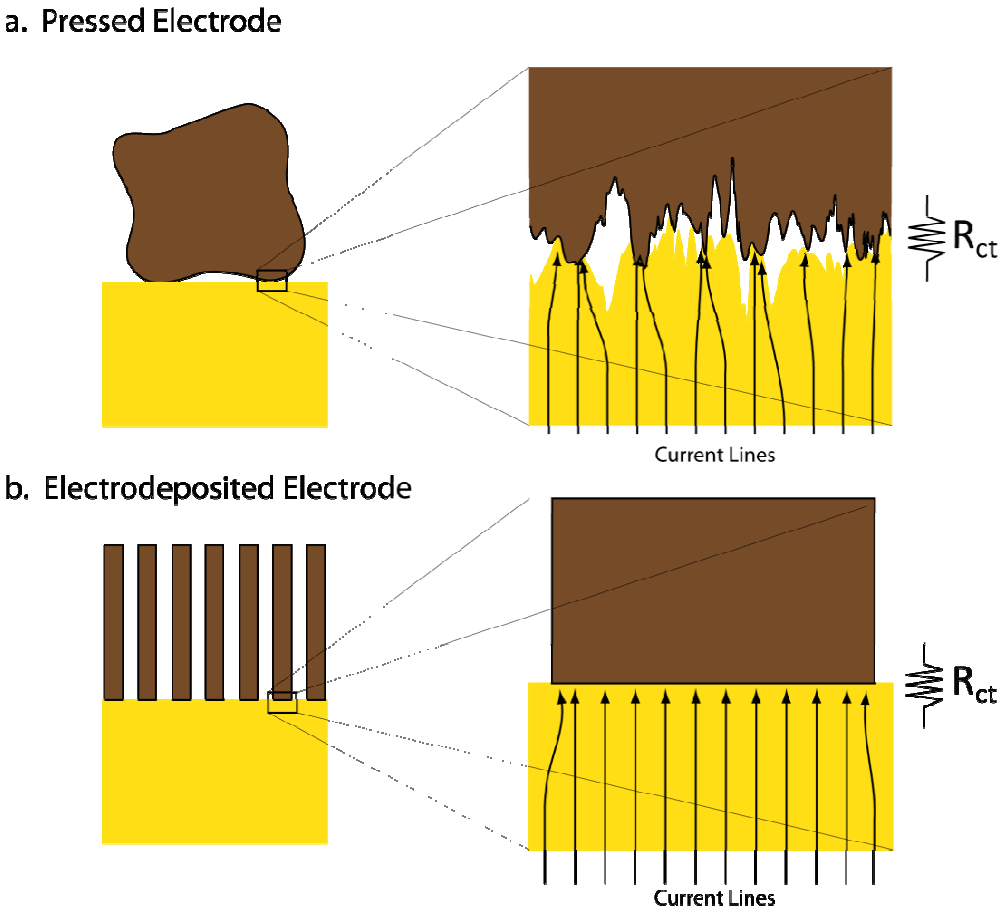

Figure 1.14. Physically Pressed versus Electrodeposited Electrode

Graphic depicting the current lines for an electrode that is pressed on to a current collector versus one that is electrodeposited with the resistance representing the contact resistance, R_{ct}

One way to achieve intimate contact between the current collector and MnO_2 is through direct electrodeposition of MnO_2 onto a conductive substrate. Large gravimetric and volumetric energy densities can be achieved through this method mainly by the deposition of thin metal, metal oxide, or conductive polymer films.[135-137]

Although these thin films show great material utilization, the performance of the material tends to deteriorate as their thickness is increased. Therefore, there is need to nanostructure these films in order to allow the superior materials utilization at greater thicknesses for practical applications that require high areal capacitances in addition to high specific capacitances.

A wide variety of synthesis methods for MnO_2 have been developed for preparing nano-architectured electrodes by electrochemical deposition. A lot of these methods include sacrificial templates which promote the easy adoption of their nano-morphology either by positive or negative replication.

For example, Li et al. was able to make mesoporous manganese dioxide by using a triblock copolymer species (Pluronic P123 and F127) as a sacrificial template.[138] The material showed a larger specific capacitance over a non-porous film in addition to better cycle ability. In addition, Nakayama et al. used a colloidal polystyrene (PS) crystal template to produce porous manganese oxide that achieved 163 F g^{-1} compared to 21 F g^{-1} without the utilization of PS.[128]

Additional templates have been employed for this purpose; however, AAO template synthesis will be emphasized here due to its unique properties and its utilization in our research.

1.3.1 AAO Template Synthesis

The anodized aluminium oxide (AAO) template synthesis nanomaterial fabrication method was developed in the mid-1970s.[139] AAO is thought to be advantageous for nanostructure templating due to the ability to accurately control its physical features which can lead to controllable nanostructures that are needed for fundamental research. In addition, it has a high pore density (10^9 pores cm^{-2}) which is promising for practical aspects of supercapacitor research that require high areal mass loadings.

AAO is typically made by anodizing aluminium foil in a strong acid electrolyte at high overpotentials anywhere from 2 to 500 volts. The magnitude of this overpotential affects many parameters of this porous structure such as pore diameter, pore wall thickness, pore density, interpore spacing, etc. while the time for anodization affects the length of the pores. This results in good control of the aspect ratio for the pores in these membranes. A graphical representation and SEM image of an AAO template can be found in Figure 1.15. A comprehensive review of the synthesis of this template was done by Sulka.[140]

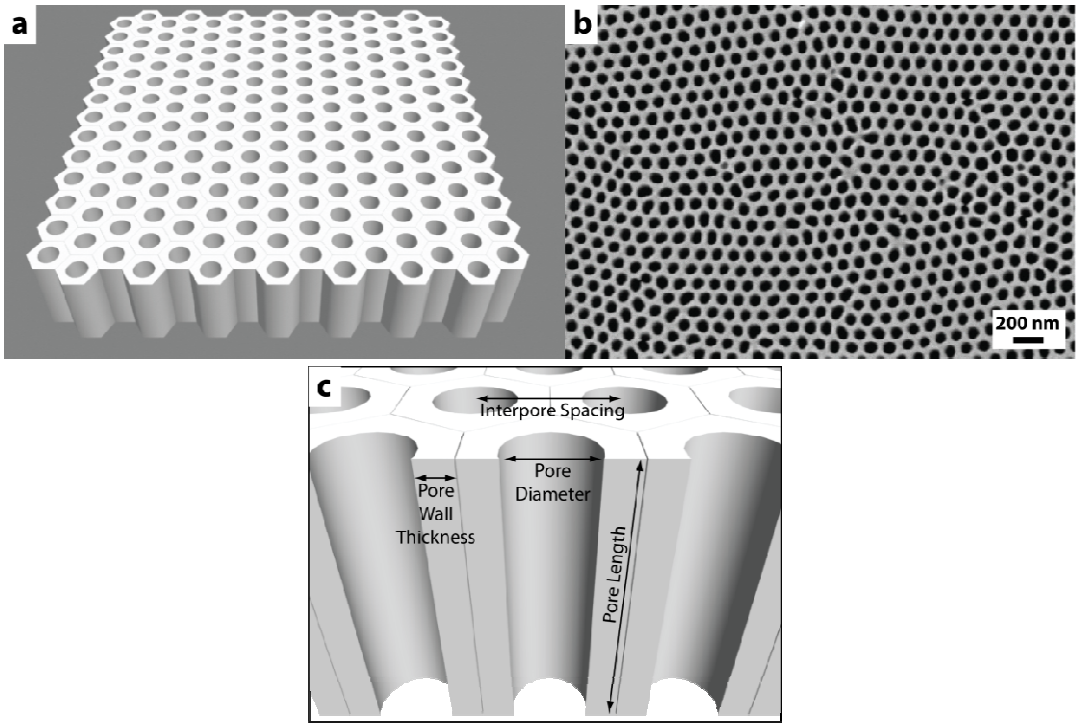

Figure 1.15. Graphic Representation and SEM Image of AAO

(a) Three-dimensional representation of an AAO template, (b) SEM top-view image of AAO (*courtesy of Ran Liu*), and (c) Close up of AAO pore structure

For electrochemical synthesis, typically the remaining aluminium is chemically etched along with the barrier layer that forms between the alumina pores and the aluminium. Then, a thin layer of conductive metal is either sputtered or evaporated onto one side of the membrane. The material, either current collector or energy storage material, is electrodeposited from the bottom up. The template is then chemically etched with either strong base or acid typically sodium hydroxide or phosphoric acid to reveal free standing one-dimensional nanowires or nanotubes directly attached to a conductive substrate. This synthesis process is represented by the graphics in Figure **1.16**.

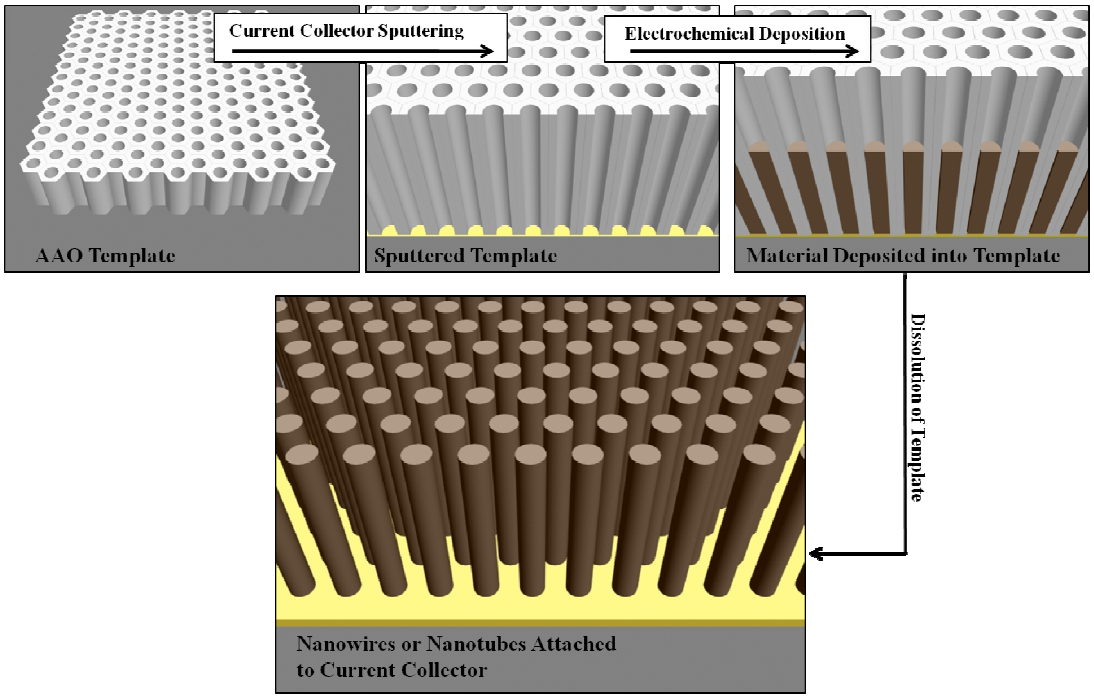

Figure 1.16. Scheme Representing Electrochemical Synthesis using AAO

In addition to the pioneering AAO template work done by Kawai *et al.*[139] in the 1970s, other groups have utilized the AAO template to produce nanomaterials through electrodeposition. For example, Ajayan's laboratory at Rice University has utilized AAO as an effective template to produce electrodeposited energy storage nanomaterials. They have shown that by first electrodepositing short gold current collectors in the AAO pores, the contact resistance between the chemical vapour deposited carbon nanotubes and their current collector is reduced due to the intimate contact between each one-dimensional structure and the current collector.[141, 142] They have also looked at the difference between electrochemically polymerized PANI coated on electrodeposited solid gold nanotubes and on porous gold nanowires synthesized from the dealloying of electrodeposited gold alloys both utilizing the AAO template.[143]

Simon and co-workers have also synthesized a variety of structures using the AAO template synthesis process. In their work reviewed here, they utilize the AAO pore structure to make electrodeposited one-dimensional nano-current collectors such as copper nanowires[29, 144] by pulsed cathodic current in an aqueous solution, or aluminium nanowires[145, 146] by pulsed cathodic current in an ionic liquid solution in an argon atmosphere glove box. Utilizing these metal nanowires, they were able to electrodeposit Fe_3O_4[29], Sn[147], and Bi[144] on the copper nanowires and by atomic layer deposition they were able to grow TiO_2[146] onto aluminium nanowires. All of these composites showed good rate capabilities owing to the intimate contact of the electrode material with the current collector.

In addition, our group has utilized this method many times to create various architectured nanomaterials as energy storage materials. The first materials analyzed by our group were conductive polymers such as polypyrrole (PPY), polyaniline (PANI), and (3,4-ethylenedioxythiophene) (PEDOT).[148] In the case of PEDOT, it was found that at high overpotentials (>1.4 V) controlling the monomer concentration and potential applied during the electrosynthesis of these conductive polymers, the morphology of the nanostructure in the AAO pore could be controlled. Accordingly, at high potentials and low monomer concentrations nanotubes were favoured while at low potentials and high concentrations nanowires were favoured. However, at low overpotentials (<1.4 V), morphology was unaffected by concentration or potential and only nanotubes were formed.[149] The mechanism for this is thought to be associated with the shape of the metal electrode at the bottom of the AAO pores. In this case, gold metal was sputtered on one side of the AAO with some of the metal actually depositing

inside the pores. Due to this, the bottom electrode has an annular or ring shape. This electrode morphology is thought to produce higher charge densities at the sharp edge of the ring along the pore wall which initiates polymerization of the monomer during conductive polymer synthesis. The monomer then continues to be polymerized up the wall forming nanotubes. The mechanism has been supported by experimentation using flat-top metal electrodes instead of ring-shaped electrodes.

By exploiting this mechanism, PEDOT nanotubes were investigated as supercapacitor materials.[43] This material was shown to have little to no charge transfer resistance from electrochemical impedance spectroscopy (EIS) owing to the good electrical contact between the electrochemically grown PEDOT and the current collector. The benefit of the PEDOT nanotubular structure as opposed to the solid PEDOT nanowires was accessibility of more of the surface of the material to the electrolyte resulting in lower diffusional resistance of the charging ions. This low resistance resulted in only a 20% drop in capacitance (150 to 120 F g^{-1}) when the power level was increased 5 times (5 to 25 mA cm^{-2}). Also, the intrinsic electrical conductivity of PEDOT allowed for only a 20% loss in specific capacitance when the charge passed during electrodeposition was increased 30 times. This means that areal energy density can be increased without much loss to the gravimetric or volumetric energy density.

The PEDOT nanotube synthesis mechanism was further exploited to create core/shell MnO_2/PEDOT nanowires.[40] This was achieved by the simultaneous deposition of PEDOT nanotubes along with a high energy density MnO_2 nanowire core. The mechanism of formation for this material can be found with the annular ring-

shaped electrodes promoting the coaxial nanostructure and the flat-top electrodes promoting a PEDOT covered MnO_2 nanodome. The advantageous core/shell structure was able to improve the areal and volumetric energy density at high power when compared to the PEDOT nanotubes alone. A completed device utilizing this material as a cathode in shown in Chapter 3:

Owing to our own previous promising research, the utilization of this template method to create heterogeneous and hierarchical MnO_2 materials for fundamental and applied research is the method used in this thesis. In addition, this method of deposition can be utilized for more fundamental science due to the ability to control the nanostructures morphology such as length and diameter.

1.3.2 Conclusions

Electrochemical deposition offers a great way to ensure good electrical contact between the MnO_2 and the current collector which is the major resistance loss in current electrochemical energy storage systems. In addition, AAO template synthesis offers a great way to control this deposition, resulting in nanowires with chosen diameters, lengths, and areal densities.

In addition, electrochemical deposition with AAO synthesis is shown in our group and in others to have been utilized to create energy storage nanostructures that have superior charge storage properties with great controllability.

Chapter 2: Characterization of Nanostructured MnO_2

In order to evaluate different nanostructured materials of MnO_2, each must be characterized well. The following sections will show how the MnO_2 structures are typically characterized. Some of the electrochemical techniques such as CV and GV that are used to characterize a materials' performance have been mentioned previously on page 12; however, here methods will be presented here that have been used to characterize the structure of the MnO_2 nanowire material produced later in this thesis. This material is typically produced using the AAO template electrosynthesis method reviewed in the previous chapter and represented by Figure 1.16. (Note: The following chapters will include the detailed synthesis of each structure.)

2.1 Electron Microscopy (SEM and TEM)

All TEM images in this manuscript were obtained by Dr. Li-Chung Lai

Obviously, since nanostructures are being dealt with here, instruments capable of visualizing these materials. Scanning and transmission electron spectroscopy (SEM and TEM) are great methods for accomplishing this goal.

In SEM, a focused electron beam raster scans electrons onto an object while a detector collects secondary electrons (SE) and back-scattered electrons (BSE) and converts the intensity of these into an image.[150] This method gives very good surface topography of a material at resolutions at or below 5 nm. Conductive samples are needed in order for high resolution imaging.

Sample preparation for this instrument is fairly easy for the research done in the following chapters. Electrode samples consisting of free-standing nanowires electronically connected to the current collector are easily prepped for SEM by simply attaching the electrode to the sample holder by a piece of double-sided carbon tape. A typical SEM image of a sample consisting of a MnO_2 nanowire array can be found in Figure **2.1**.

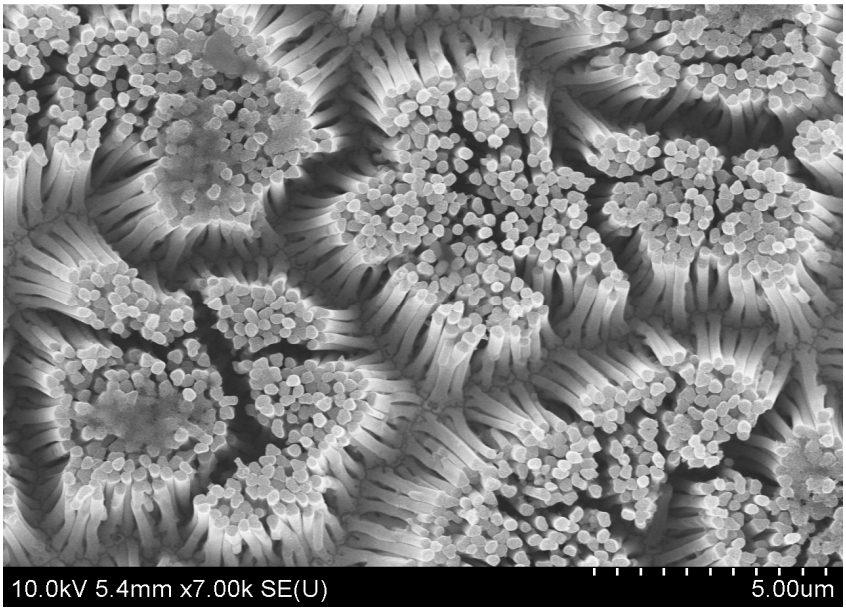

Figure 2.1. SEM image of MnO_2 Nanowires Attached to Current Collector

In TEM, a focused electron beam is transmitted through a material while a detector collects the transmitted electrons and converts the intensity of these into an image.[129] Since the electrons pass through the material, thicknesses must be kept below a few hundred nanometers. Advanced TEMs can resolve individual columns of atoms with resolutions down to less than 0.5 Ǻngstroms.

TEM samples in the following chapters were prepared by sonicating free-standing nanowire arrays in ethanol which caused the nanowires to detach from the current collector and disperse into the ethanol. The resulting nanowire suspension was then drop cast on a carbon-coated copper grid. A typical TEM image of a MnO_2 nanowire can be found in Figure 2.2.

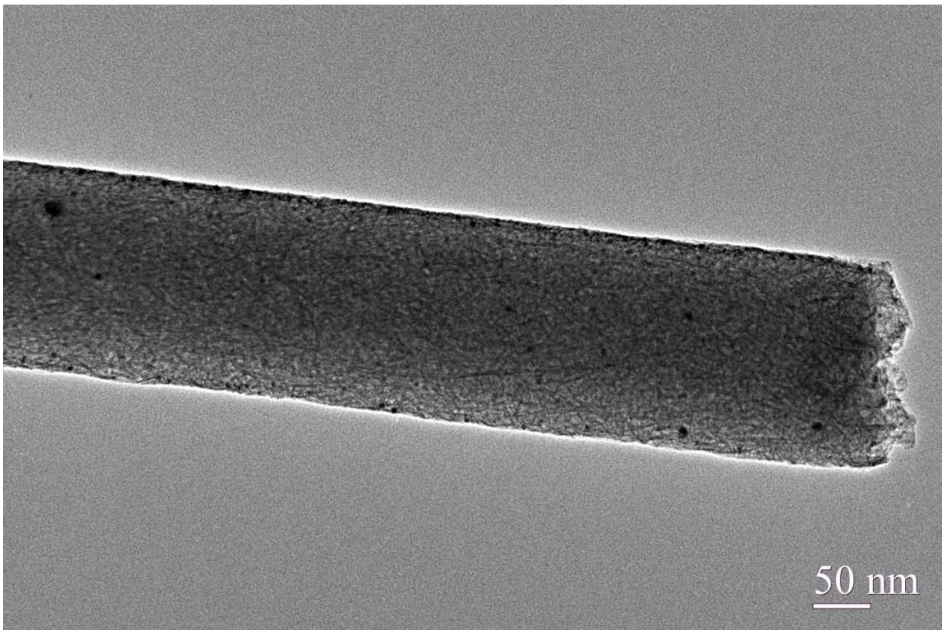

Figure 2.2. Typical TEM Image of MnO_2 Nanowire

2.2 Energy Dispersive X-ray Spectroscopy (EDS)

All EDS data in this manuscript was obtained by Dr. Li-Chung Lai

SEM and TEM are both capable of another analytical technique termed energy-dispersive X-ray spectroscopy (EDS). For this, a detector is used that collects X-rays during the electron bombardment of the sample.[129] The data is then represented as intensity of X-rays versus the energy of the X-rays. Since each X-ray's energy is

associated with a known elemental electron transition of the material, the qualitative and quantitative elemental content of the sample can be determined.

For SEM, the signal can come from over a micron into the sample. This means that care must be taken when analyzing the data as the subsurface and even the substrate may contribute to the overall EDS spectrum.

For TEM, samples should be dispersed on a holey carbon grid with samples positioned over the holes. This results in a mitigation of any contamination from the carbon film or other contaminants that may have adsorbed on the film. As with SEM, the signal for EDS in TEM comes not only from the surface of the material, but from the whole bulk of the material. Even so, the radial distribution of materials in core/shell nanowires can be determined using this method. For example, Figure **2.3** shows a typical core/shell nanowire with the Ru $L_{\alpha 1}$ spectrum indicating of a shell of RuO_2 with larger intensities at the edges of the nanowire and the Mn $K_{\alpha 1}$ spectrum typical of a core MnO_2 structure with the largest intensities in the middle of the nanowire.

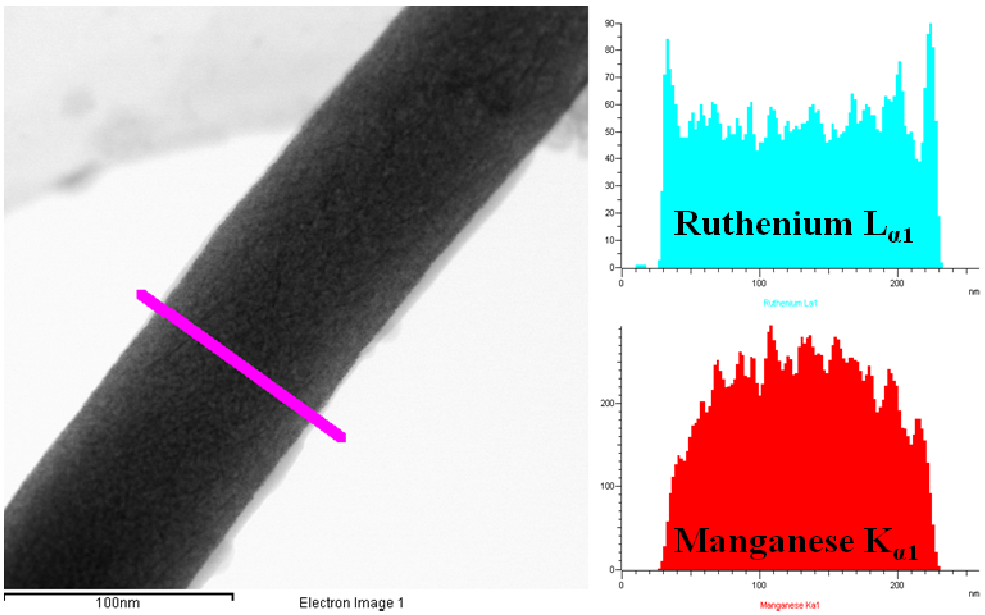

Figure 2.3. TEM Image and EDS Spectra of a MnO_2/RuO_2 Core/Shell Nanowire

2.3 Electron Energy Loss Spectroscopy (EELS)

All EELS data in this manuscript was obtained by Dr. Wen-An Chiou

TEM is also capable of another elemental composition technique called electron energy loss spectroscopy (EELS). In this method, a detector analyzes the energy of electrons after they have passed through the sample.[129] Due to the interaction of the electrons with the atoms in the sample a loss of energy is observed. The magnitude of this loss can be correlated directly with the specific element that caused the loss. An advantage of EELS over EDS is that EELS can probe the chemical state of the elemental atom. In other words, data such as valence state and bonding structure can be obtained.

Samples here should be fairly thin (<50 nm for dense solid samples), as samples thicker than the mean free path can result in more than one electron energy loss

interaction, reducing the signal to noise ratio of the EELS spectra peaks. A typical EELS spectrum of an MnO_2 nanowire can be found in Figure 2.4.

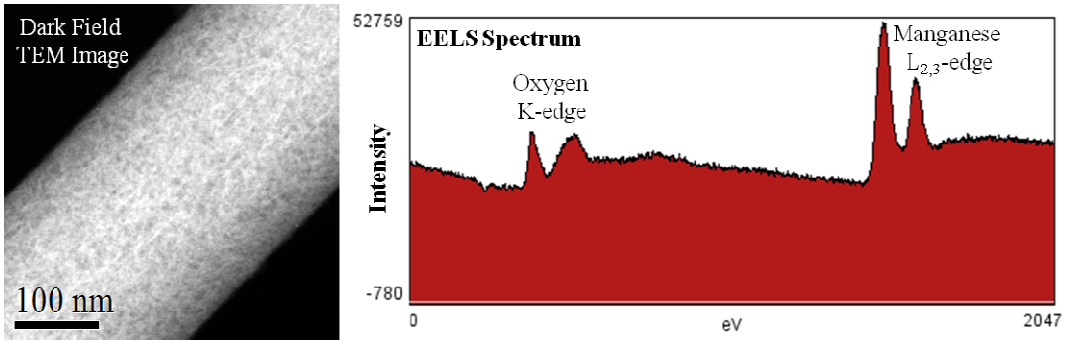

Figure 2.4. Typical EELS Spectrum of MnO_2 Nanowire

2.4 X-ray Photoelectron Spectroscopy (XPS)

All XPS data in this manuscript was obtained by Dr. Karen Gaskell

Another elemental spectroscopy technique used often is X-ray photoelectron spectroscopy (XPS). In this method, the sample is probed with X-rays at a constant energy (typically aluminum Kα = 1486 eV) while a detector monitors the energy of electrons called photoelectrons that are escaping the material.[151] The energy difference between the escaping photoelectrons and the energy of the excitation X-ray is termed the binding energy (BE) and is directly related to the electronic structure of certain elements. The results of XPS can be both qualitative and quantitative as the quantity of electrons at a certain BE can be correlated to the amount of atoms of that element with detection limits as low as the parts per million (ppm) range.

Although the X-rays can penetrate millimeters into the material, the emitted photoelectrons only come from the top ten to twelve nanometers of the material as the

electrons at greater depths tend to be recaptured or trapped in excited states. Therefore, chemical composition is only obtained from the surface. However, ion sputtering can be used to probe the chemical composition of the bulk of the material by removing the surface layer and then analyzing again.

Valence states can also be detected for transition metal elements using this technique. For manganese specifically, the magnitude of the separation of the $2p_{1/2}$ and $2p_{3/2}$ satellite peaks has been used as a valence state indicator; however, this magnitude tends to differ by less than the resolution of the detector (between 11.68-11.78 eV from MnO to MnO_2) and is not very reliable.[152] Therefore, the magnitude of the valence-band 3s satellite separation is thought to be a better indicator as this can vary by more than 1 eV (between 4.69-5.78 eV from MnO_2 to MnO). Figure **2.5** represents a typical XPS spectrum obtained from an MnO_2 nanowire array for the Mn 2p and Mn 3s satellite peaks. Here, only surface valence state can be detected and ion sputtering is not ideal to probe the valence state beneath the surface as oxygen is preferentially sputtered leaving the remaining material at an artificially lower valence state.

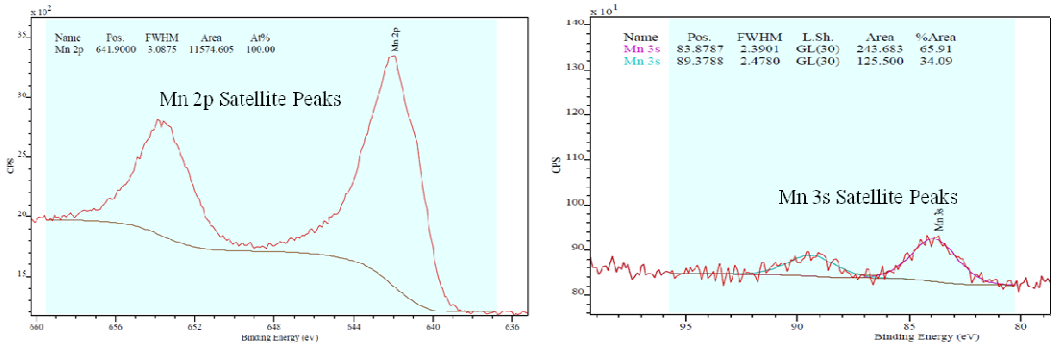

Figure 2.5. Typical XPS Spectrum of MnO_2 Mn 2p and Mn 3s Satellite Peaks

Samples preparation for this technique is not very complicated as most samples can be prepared as they would be used in their system, so a result from this technique is very characteristic of how it is during its performance. However, since it is in a vacuum environment, samples need to be dry and not have any trapped air which can expand in the substrate or support material.

2.5 Raman Spectroscopy

Raman spectroscopy is a technique that can probe the bonding structure of a molecule. In this method, a laser with a wavelength typically in the visible spectrum is used to excite electrons in a material to virtual excited energy states.[153] Upon relaxation, electrons can transition back to their initial state, called Raleigh Scattering, or a higher vibrational state, called Stokes Scattering, or a lower vibrational state, called anti-Stokes scattering. The Stokes and anti-Stokes scattering results in intensity versus energy curves that are characteristic of the bonding structure of a molecule.

Sample preparation for Raman spectroscopy is fairly straightforward as samples are not heated or placed in a vacuum as well as no requirements for conductivity of the sample or the composition of the substrate. However, the power of the excitation laser must be monitored as high power can anneal the sample resulting in Raman spectra associated with the annealed sample and not the original. A typical Raman spectrum obtained from a MnO2 nanowire array sample can be found in Figure 2.6.

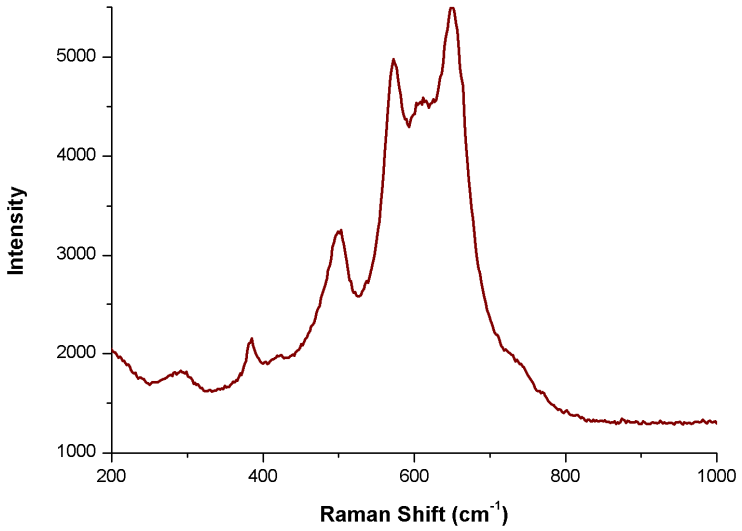

Figure 2.6. Typical Raman Spectrum of an MnO2 Nanowire Array

2.6 Inductively Coupled Plasma – Atomic Emission Spectroscopy

Inductively coupled plasma – atomic emission spectroscopy (ICP-AES) is a destructive technique that can determine the elemental composition of an entire electrode. In a typical ICP-AES analysis, a solution of ions is pumped through a glass nebulizer, where a fine mist of the solution is produced.[153] A small portion of this mist is then carried into argon plasma created by a radiofrequency (RF) coil where the ions are desolvated and excited by the bombardment of electrons from the plasma. The ions then relax to the ground state releasing photons with a wavelengths directly related to their atomic makeup. These photons are then directed to a charge-coupled device (CCD) camera where their intensity is measured.

Samples prepared for this method must first be digested into solution. This requires highly concentrated acids such as nitric or hydrochloric acid. Great care must be taken to avoid contamination as detection limits for ICP-AES reach into the parts per billion

(ppb) range. This includes using only new or nitric acid soaked glassware to prepare samples.

Sample preparation of our nanowire materials can require many rinsing steps in order to eliminate possible analyte contamination from the electrolyte. Typical calibration curves and an example of experimental results from ICP-AES can be found in Figure 2.7.

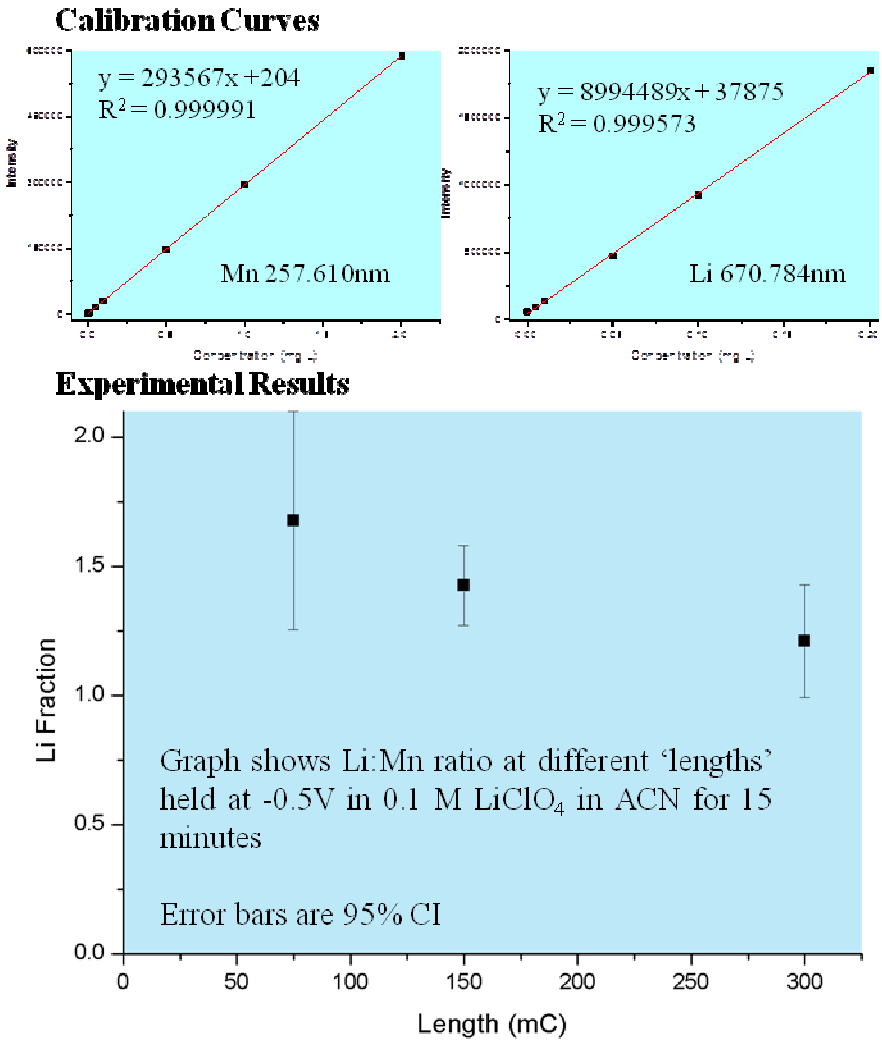

Figure 2.7. Sample Calibration Curves and Experimental Results Utilizing ICP-AES

2.7 Conclusions

An overview of MnO_2 nanomaterials being characterized by a variety of microscopy and spectroscopy techniques in order to characterize their elemental composition and chemical bonding structure was presented here. A easily visualized comparison of each spectroscopy technique can be found in Table 2.1.

Table 2.1. Comparison of Spectroscopy Techniques Used

Spectroscopy Technique	Excitation Source	Detected Product	Typical Spectrum	Chemical Information
EDS	Electron Beam	X-rays	Intensity vs. Energy of X-rays	Semi-Quantitative Elemental Distribution
EELS	Electron Beam	Electrons	Intensity vs. Electron Energy Lost	Elemental Distribution and Valence State
Raman	Laser Beam	Photons	Intensity vs. Wavenumber of Light Emitted	Chemical Structure and Bonding
XPS	X-rays	Photoelectrons	Intensity vs. Binding Energy of Photoelectron	Quantitative Elemental Composition and Surface Valence State
ICP-AES	Argon Plasma	Photons	Intensity vs. Selected Wavelengths	Quantitative Bulk Elemental Composition

In the following chapters, it will be shown how these methods were utilized to characterize heterogeneous, hierarchical, and pure MnO_2 nanowires for advanced and elementary studies.

Chapter 3: Highly Flexible Pseudocapacitor Based on Freestanding Heterogeneous MnO_2/Conductive Polymer Nanowire Arrays

Currently there is a growing interest in flexible electronics. The paradigm of electronics being encased in hard shells is slowly eroding. New technology is focused on flexible applications of electronics such as wearable electronics,[154] paper-like electronics,[155] and flexible biomedical devices[156]. These novel electronic devices will require flexible energy sources to power them. Currently, energy sources based on electrochemical energy contain electrodes consisting of brittle energy dense metal oxides mixed with conductive carbon and polymer binders pressed into pellet form.[157] The conductive carbon is needed to electrically connect, while the polymer binder is used to physically connect, all of the metal oxide material to the current collector. These electrodes must be encased in a rigid metal shell in order to prevent the cracking, breaking, and delamination of the electrode material from the current collector thus severely limiting their flexibility.

On the other hand, vertically aligned freestanding nanowire array electrodes have the ability to be highly flexible. These arrays are directly grown on the current collector providing good electrical connectivity, as well as excellent physical connectivity, of all of the energy dense material. This eliminates the need for additional carbon additives and polymeric binders. Their flexibility can be attributed to each nanowire's independent movement during flexing.

As the flexible electronic devices will no doubt become multi-functional, they will need a high power energy source to help augment the low rate capability battery as a

hybrid system. One energy storage device known for its high power is the capacitor. Electrostatic capacitors have been used extensively as high power load levellers in household devices such as radios and in air conditioners. To use capacitors in flexible electronic devices, they would need to deliver high power over even longer times for such things as Wi-Fi and GPS enabled wearable fabrics. However, these electrostatic capacitors have a very low energy density which would require them to be quite bulky, thus making them unacceptable for use in flexible device applications.

On the other hand, electrochemical capacitors, also known as supercapacitors, have shown large enough energy densities[1, 158] to allow them to be used in mobile electronics as high power load levelers.[159] These devices could be used in conjunction with the battery in order to provide high power when running applications such as GPS, games, and videos on flexible paper-like electronics. These supercapacitor devices could then be recharged by the battery at lower current rates during standby times.

Electrochemical double layer capacitors (EDLCs) based on carbon materials have shown very good performance metrics such as high power and high energy[160-162]; however, supercapacitors based on pseudocapacitance have the capability to have much larger specific capacitances (>1000 F/g theoretical). These pseudocapacitive materials involve a faradaic transfer of charge across the electrolyte-electrode interface. These materials include conductive polymers such as polyaniline,[163] polypyrrole,[164] and polythiophene[165] and their derivatives in addition to metal oxides such as RuO_2,[166, 167] MnO_2,[33, 64, 168-171] V_2O_5,[32] Fe_3O_4,[172] and $Ni(OH)_2$.[173, 174] Among these materials, poly (3,4-ethylenedioxythiophene) (PEDOT) and MnO_2 have a strong potential to be used in commercial supercapacitor applications.

PEDOT, a derivative of polythiophene, has received considerable attention as a supercapacitor material due to its large electroactive potential window and high chemical stability among conductive polymers.[43, 175] MnO_2 is considered a leading candidate for commercialization due to its own large electroactive potential window, low cost, environmental friendliness, high theoretical capacitance, and abundance.

Our group has extensively studied the supercapacitor properties of PEDOT and MnO_2 in different morphological combinations, including PEDOT nanotubes, PEDOT/MnO_2 coaxial nanowires, and PEDOT nanowires embedded with MnO_2 nanocrystals.[40, 43, 176, 177] For example, it has been demonstrated that the supercapacitor performance of arrays of coaxial MnO_2-core PEDOT-shell nanowires is far superior when compared to their single component materials.[40] The MnO_2 provides high energy density, while the PEDOT provides a conductive coating to induce fast electron transport and high ion permeability for ion transport to the MnO_2 core. The PEDOT also provides flexibility which can help buffer the stresses involved during the charging and discharging of MnO_2 in addition to allowing freestanding nanowires to be grown at high aspect ratios without breaking.

Previously, it was shown that the mechanism of synthesis for these coaxial nanowires was due to the annular shaped gold nanoelectrodes at the bottom of the AAO pores which promotes the growth of the PEDOT shell.[176] These nanowires display a specific capacitance of 270 F/g even at a 9 A/g current density in an aqueous electrolyte. Due to these properties, this material was chosen to be incorporated into a flexible supercapacitor device.

However, when designing a supercapacitor, maximizing the energy of the device is

paramount. As the equation for the energy of a supercapacitor, $E = \frac{1}{2} CV^2$, demonstrates, one can not only improve the energy of the device by increasing the capacitance, C, of the electrode materials, but can also increase the energy of the device by increasing the voltage window, V.[178] This increase in the voltage window can occur by using organic instead of aqueous electrolytes and also by using an asymmetric system where the anode and cathode utilize different materials. The asymmetric design has been utilized many times in the literature to offset MnO_2's mediocre 1 volt potential window. This has included using activated carbon[53, 179-181], carbon nanotubes[54], and graphene[182] among other materials[59] as the anode in this design.

Accordingly, for the coaxial MnO_2-PEDOT material, the maximum voltage window that can be used for the symmetric device is 1 V. This is due to MnO_2's electrochemical reversibility window.[35] However, if PEDOT, whose reversibility window extends beyond MnO_2's, is utilized as an anode in an asymmetric system; the voltage window for the entire device can be enhanced up to 1.7 V. This increase in voltage has the capability of the asymmetric device having an almost 3 (1.7^2) times increase in energy.

Herein, a flexible asymmetric pseudocapacitor based on coaxial MnO_2/PEDOT and PEDOT nanowire arrays has been synthesized. This asymmetric device consists of a coaxial nanowire array as the cathode and a PEDOT nanowire array as the anode and is shown here to have a larger energy and power density along with better cycle ability than a symmetric device which incorporates the coaxial nanowire array as both the cathode and anode. The improvement in energy density is attributed to the asymmetric device's larger (1.7 V vs. 1.0 V) voltage window, while the improvement in power

density and cycle life is attributed to the PEDOT nanowire array's improved stability as an anode material when compared to the coaxial nanowire array anode used for the symmetric device.

Evaluated as a full cell, the asymmetric device has a total mass, including all of the packaging materials, of 0.47 g with a total capacitance of 0.26 F and a maximum voltage of 1.7 V, which is capable of providing enough energy to power small portable electronics. This device's electrode materials display an energy density of 9.8 Wh/kg even at a high power density of 850 W/kg. Finally, this device maintains 86% of its energy density even under a highly flexed state.

3.1 Experimental

3.1.1 Chemicals and Materials

Poly(methyl methacrylate) (PMMA), 3,4-ethylenedioxythiopene (EDOT), manganese acetate, propylene carbonate (PC), and lithium perchlorate (LiClO4) were purchased from Sigma Aldrich (Milwaukee, WI). Sodium dodecyl sulfate (SDS) and acetonitrile (ACN), was obtained from Fisher Scientific (Fair Lawn, NJ). Plastic paraffin paper (Parafilm^{TM} M) was purchased from Pechiney Plastic Packaging Company (Chicago, IL). Pressure sensitive polypropylene tape (Scotch^{TM} 3710), and copper electrical tape can be obtained from 3M Corporation (Maplewood, MN). Gold targets for sputtering were purchased from Denton Vacuum LLC (Moorestown, NJ). De-ionized water (ca. 18 MΩ·cm resistivity) was made by a Milli-Q water purification system (Millipore; Dubuque, IA). Anodized alumina (AAO) membranes of 200 nm pore diameter and 60 µm thickness are commercially available from Whatman (Clifton,

NJ). All electrochemical tests were done on a Bistat bipotentiostat from BioLogic (Claix, France).

3.1.2 Synthesis of Electrode Materials

First, a thin layer of gold (ca. 500 nm) is sputtered onto one side of an alumina (AAO) membrane by sputter deposition using a Denton Vacuum Desktop III sputter machine. The Au-coated membrane is connected to an electrical circuit using a copper tape (3M). Defining and sealing an electroactive window (2.88 cm^2 in nominal area) is performed by sandwiching the template between two layers of silicone rubber with one layer having a 2.88 cm^2 hole punched out. Considering the porosity of the membrane (60%), the corrected surface area of the electroactive window is 1.8 cm^2. A separate gold-sputtered AAO membrane is then placed in the electrodeposition bath for the Coaxial and PEDOT nanowire as the working electrode.

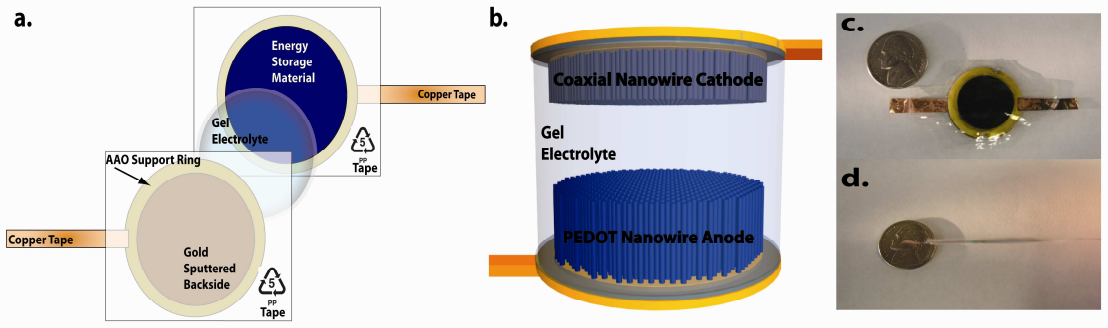

Figure 3.1. Graphic and Digital Images of Flexible Device

(a) Exploded schematic view of flexible supercapacitor device. (b) Side-view schematic of the asymmetric device where gray represents the Coaxial MnO_2/PEDOT Nanowire Cathode and Blue represents the PEDOT Nanowire Anode (c) Top view and (d) side view image of demo device shown with a United States Nickel for scale.

Coelectrodeposition of the heterostructured MnO2/PEDOT nanowire arrays is performed in an aqueous electrodeposition bath consisting of 80 mM EDOT monomer, 10 mM manganese acetate, 160 mM sodium dodecyl sulfate, and 100 mM lithium perchlorate. The gold sputtered AAO is the working electrode with platinum as the counter electrode and Ag/AgCl as the reference electrode. A voltage of 0.75 V vs. Ag/AgCl is applied until the charge reached 5C.

Electrodeposition of PEDOT nanowire arrays is performed in an acetonitrile solution of 100 mM EDOT monomer and 100 mM lithium perchlorate. The gold sputtered AAO is the working electrode with platinum as the counter electrode and Ag/AgCl as the reference electrode. A voltage of 1.2 V vs. Ag/AgCl is applied until the charge reached 8.55 C. The total mass of all electrode materials are calculated using the amount of charge passed and faraday's law.

$$m = \frac{QM}{zF}$$

Where Q is the charge passed in coulombs, M is the molar mass of the material in gram/mole (86.94 g/mol for MnO_2 and 140.13 for PEDOT) , z is the number of electrons transferred per unit material (1.7 for MnO_2 and 2.3 for PEDOT)[176], and F is faraday's constant (96,485 coulombs per mole).

3.1.3 Assembly of the Device

The gold sputtered side of each AAO with the energy material inside is attached to the adhesive side of a piece of polypropylene tape. Another piece of tape with a 2.8 cm^2 hole is attached to the adhesive side of the previously applied tape on top of the AAO support ring. This additional tape is used to define the electroactive window. Each electrode is then soaked in a 3M NaOH solution for 12 minutes to dissolve the AAO, resulting in freestanding nanowires attached to a gold current collector. Each electrode is rinsed and soaked three times each in DI water followed by a rinsing and soaking in acetonitrile.

Next, the electrolyte is made by first mixing 4.2 mL of 1M lithium perchlorate in a 5:2 V:V ratio of acetonitrile:propylene carbonate solvent with 0.8 g of PMMA. This mixture was then heated with vigorous stirring to 105°C using a hotplate until the solution begins to gel. At this point, 100 µL of electrolyte solution is placed onto each electrode. For the symmetric device, the electrodes both consist of the coaxial nanowire array. The asymmetric device consists of the coaxial nanowire array as the cathode and

the PEDOT nanowire array as the anode. The solution is allowed to set for 6 hours to form a viscous gel. Finally, the electrodes are sealed together using more polypropylene adhesive tape.

3.1.4 Device Testing

Cyclic voltammetry is done with 20, 50, and 100 mV/s scan rates at potential windows of 1.0 and 1.7 V for the symmetric and asymmetric device respectively. Galvanostatic voltammetry is done from 0.25 A/g to 10 A/g based on the masses of 5.86 mg for the symmetric device and 8.29 mg for the asymmetric device in the same potential windows as the cyclic voltammetry.

Using the GV curves, the specific capacitance (C_{sp}) for the device can be calculated using the following equation[183]:

$$C_{sp} = \frac{4C}{m} = \frac{4ti_d}{V}$$

Where C is the capacitance of the device, m is the mass of the electrode materials, t is the time for discharge, i_d is the current density, and V is the voltage maximum.

3.1.5 *"in situ"* Anode and Cathode Monitoring

Electrode materials for the symmetric and asymmetric devices were prepared by previous methods except the electroactive area of the AAO template and the amount of charge passed was reduced by one ninth. The testing was done in a beaker cell containing 1M $LiClO_4$ in a 5:2 V:V acetonitrile : propylene carbonate. The anode and cathode were cycled between absolute voltages of 0 to 1 V and 0 to 1.7 V for the symmetric and asymmetric device respectively. The anode and cathode's relative

voltages were monitored using a Ag/AgCl reference electrode.

3.1.6 Extended Window Voltage Testing

Electrode materials for the asymmetric device are prepared by previous methods except the electroactive area of the AAO template and the amount of charge passed was reduced by one ninth. Each electrode is set up in a beaker cell containing 1M $LiClO_4$ in a 5:2 V:V acetonitrile : propylene carbonate. Testing is done in a three electrode system with the electrode material as the working electrode, platinum as the counter electrode, and Ag/AgCl as the reference electrode. The electrodes were cycled between -0.95 V and 0.20 V vs. Ag/AgCl for the PEDOT nanowire electrode and between 0.20 V and 1.45 V vs. Ag/AgCl for the coaxial nanowire electrode.

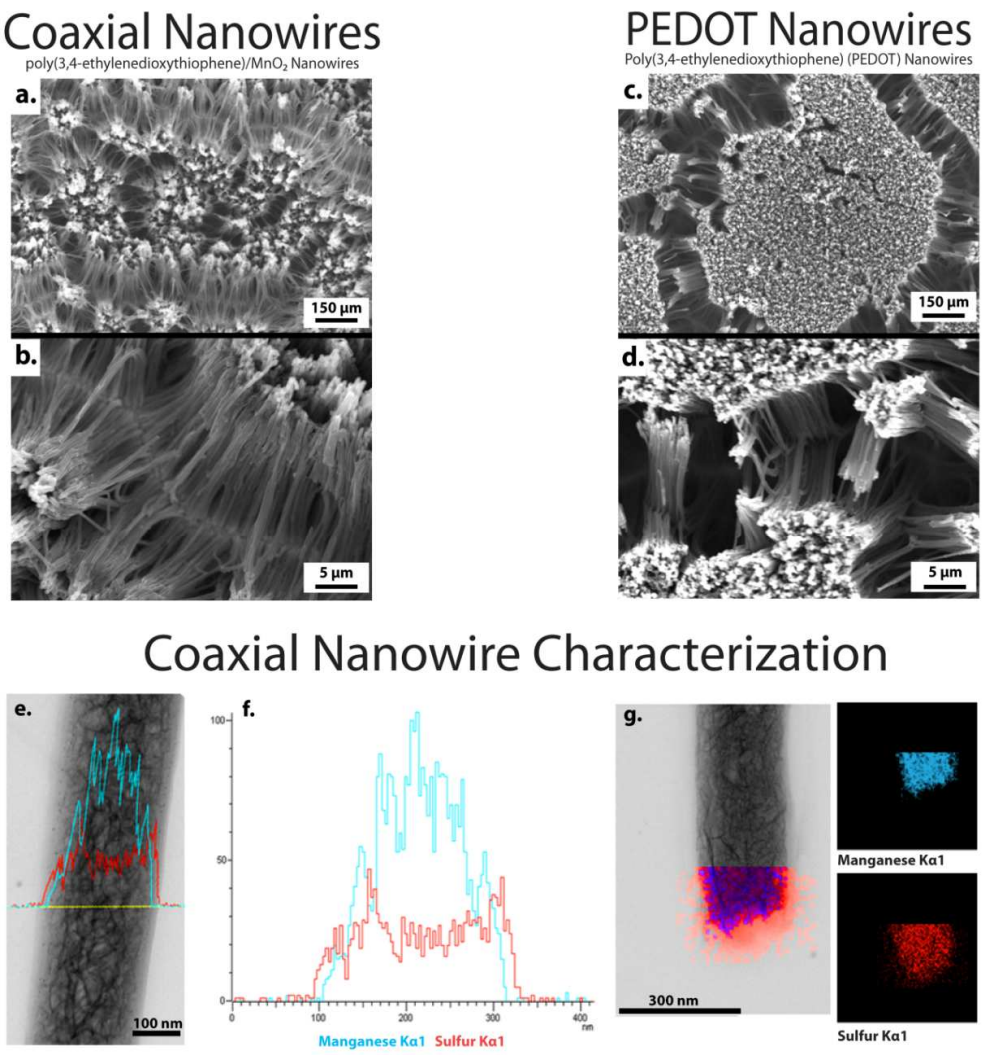

Figure 3.2 SEM, TEM, and EDS Analysis of Coaxial and PEDOT Nanowires

(a) SEM image of an array of freestanding coaxial nanowires on a gold current collector, (b) higher magnification of material in (a), (c) SEM image of an array of freestanding PEDOT nanowires on a gold current collector, (d) higher magnification SEM image of material in (c), (e) EDS line scan across a coaxial nanowire (Blue = Mn, Red = S), (f) EDS line scan graph for better visualization of the position of Mn (Blue) and S (Red) along the nanowire, and (g) EDS mapping of the end structure of a coaxial nanowire where red represents S and blue represents Mn.

3.2 Results and Discussion

Herein, a flexible supercapacitor device is tested that is capable of powering small electronics. This device consists of electrodes made of free-standing arrays consisting of poly (3,4-ethylenedioxythiophene) (PEDOT) and coaxial PEDOT-shell MnO_2-Core nanowires. Both a symmetric Coaxial-Coaxial and asymmetric Coaxial-PEDOT device are tested and compared. The asymmetric device shows here a considerable improvement in energy density, power density, and cycle life when compared to the symmetric device.

A schematic for the devices can be seen in Figure **3.1** (a and b). Each device consists of two electrodes with freestanding nanowires attached to a gold current collector. These electrodes are encased in polypropylene pressure sensitive tape acquired from the 3M Corporation with the electrode material facing away from the adhesive. Each electrode is attached to copper tape in order to be connected to the electronic circuit. The electrolyte consists of 1 M $LiClO_4$ in a 5:2 V:V acetonitrile : propylene carbonate solvent that is mixed with poly(methyl methacrylate) (PMMA) as the gelling agent. The total device mass including packaging is 0.47 g, while the total active area is 2.8 cm^2.

The electrode nanomaterials are synthesized using a commercial anodized aluminum oxide (AAO) membrane by a template-electrodeposition method. Briefly, AAO membranes with a 2.8 cm^2 total area, 60-micron thickness, and 200-nm nominal cylindrical pore-size are used. A gold current collector is sputtered on one side of the AAO template. The template is then immersed in the electrodeposition bath with only the open pore side exposed to the solution. The electrode materials are then grown

electrochemically at the surface of the gold current collector from the bottom of the pores. Finally, the AAO membrane is removed by NaOH wet etching, revealing freestanding nanowires attached to the gold current collector. These nanowire arrays are then combined with the electrolyte and sealed with polypropylene tape to make the completed device.

The PEDOT nanowire arrays for the asymmetric device anode are grown at 1.2 V vs. Ag/AgCl from an acetonitrile solution containing 3,4-ethylenedioxythiophene (EDOT) monomer and $LiClO_4$ as the dopant. These wires are ~40 µm in length and have a 200 nm nominal diameter. The total mass of these nanowires is 5.36 mg. The SEM images in Figure 3.2 (c and d) display the dense forest of freestanding PEDOT nanowires used for the electrode.

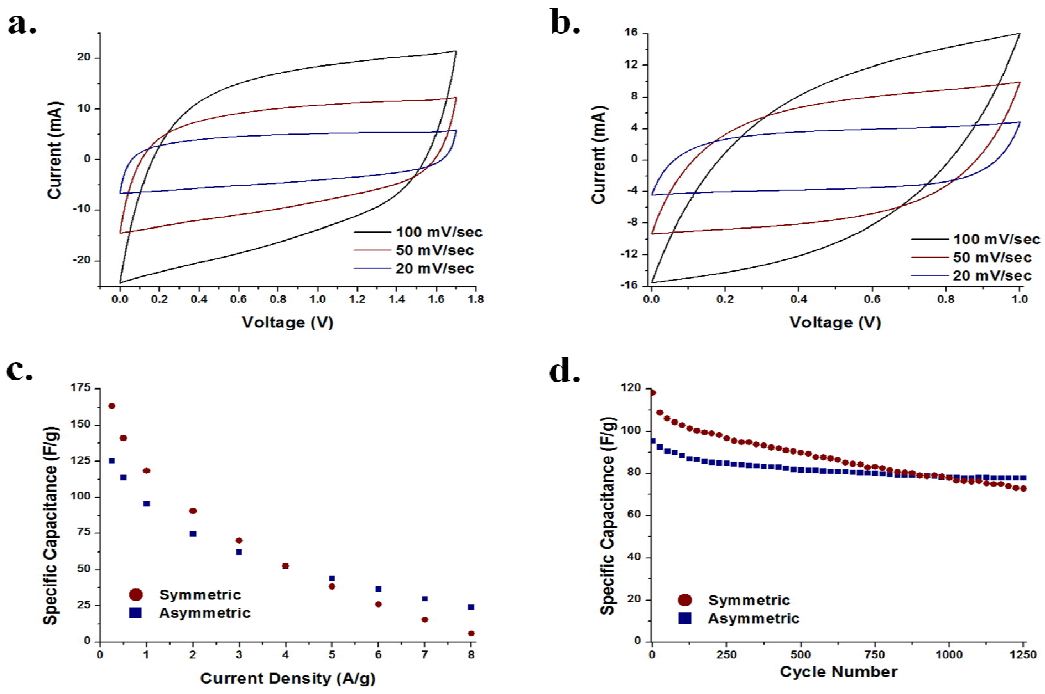

Figure 3.3 Electrochemical Performance of Asymmetric and Symmetric Device

(a) Cyclic voltammetry at different scan rates for the asymmetric Coaxial-PEDOT nanowire device, (b) cyclic voltammetry at different scan rates for the symmetric Coaxial-Coaxial nanowire device, (c) Rate capability for both the symmetric and the asymmetric device and (d) the cycle ability for both the symmetric and the asymmetric device done using galvanostatic voltammetry at 1 A/g.

The coaxial MnO_2/PEDOT nanowires for both the asymmetric and symmetric device are grown at 0.75 V vs. Ag/AgCl from an aqueous solution containing manganese acetate, EDOT monomer, $LiClO_4$, and sodium dodecyl sulfate (SDS) as a surfactant for the dissolution of EDOT. Previously, it had been shown that by using a lower synthesis potential (0.70 V vs. Ag/AgCl) a thinner PEDOT-Shell could be grown resulting in a higher specific capacitance[176]; however, since the coaxial nanowires grown here are

more than 2.5 times longer it is believed that extra PEDOT-Shell can help support this elongated high aspect ratio structure. These 0.75 V synthesized nanowires are ~17 µm in length with a 200 nm nominal diameter. The total mass of these nanowires is 2.93 mg per electrode. Figure 3.2 (a and b) shows the SEM top view image of the freestanding coaxial nanowires attached to a gold current collector. The nanowires are seen to be agglomerated at their tips in the SEM images due to the surface tension of water during the drying process which is needed for the SEM imaging. However, in solution these nanowire tips will not be agglomerated.

The coaxial nanowires are characterized using EDS line scans and mapping as can be seen in Figure 3.2 (e-g). The Mn comes from the MnO_2 material while the S comes from the thiophene ring of the PEDOT. The EDS shows that the PEDOT is located on the outside of the wires, while the MnO_2 is found in the core. Figure 3.2g indicates that the MnO_2-core PEDOT-shell coaxial morphology continues along the axis of this nanowire up to the tip.

The total mass of the electrode materials is 8.29 mg for the asymmetric Coaxial-PEDOT device and 5.86 mg for the symmetric Coaxial-Coaxial device, calculated based on Faraday's law. The PEDOT anode's mass was made much larger than the coaxial cathode's in the asymmetric device because of the higher specific capacitance of the coaxial nanomaterial compared to PEDOT nanowires (210 F/g and 115 F/g, respectively).[40]

Figure 3.3a shows the CV curves of the asymmetric device at different scan rates between 0 and 1.7 V. The asymmetric device maintains its rectangular CV even at scan rates up to 100 mV/s, indicating good rate capabilities.

Figure 3.3b shows the cyclic voltammetry (CV) curves of the symmetric device at different scan rates between 0 and 1 V. The 20 mV/s CV curve again shows a near ideal rectangular shape; however, at the higher scan rate of 100 mV/s, the curve shows a deviation from this shape indicating a low rate capability.

Figure 3.3c shows the rate capability of both the symmetric and asymmetric devices calculated from galvanostatic voltammetry. As eluded to qualitatively in the CV curves, the asymmetric shows a much better rate capability than the symmetric device. Case in point, the symmetric device has a higher specific capacitance than the asymmetric device (163 F/g to 125 F/g, respectively) at a low current density (0.25 A/g), but at a high current density (8 A/g) the symmetric device has a lower specific capacitance (6 F/g to 24 F/g). This increased rate performance of the asymmetric device is highly encouraging for potential high power applications of flexible electronics such as GPS or Wi-Fi enabled wearable devices.

For the previous results, one must keep in mind that although specific capacitance is a great figure of merit to compare supercapacitor materials, voltage window is even better as $E = \frac{1}{2} CV^2$. Therefore, although the symmetric cell has a higher specific capacitance at low current densities, the asymmetric cell will still have a higher energy density as it has a higher voltage window (1.7 to 1.0 V). This is examined further during the discussion of the Ragone Plot.

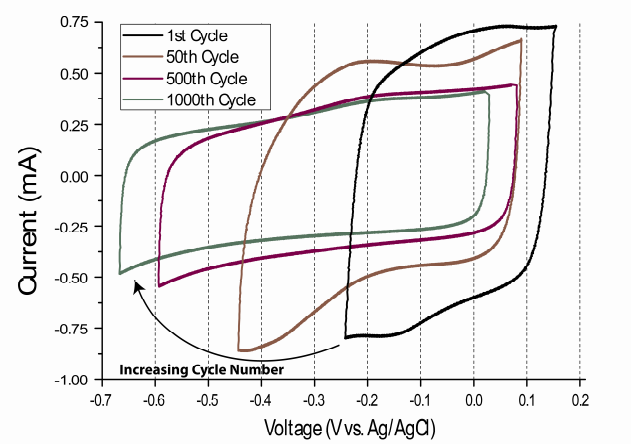

Figure 3.4 PEDOT Anode CV Curve during Cycling

"*In Situ*" CV curves at 20 mV/sec scan rate of the coaxial anode for different cycle numbers (Black = 1st, Orange = 50^{th}, Red = 500^{th}, Green = 1000^{th}). The voltage is measured versus a Ag/AgCl reference.

Figure 3.3d shows the cycle ability for both the symmetric and asymmetric devices calculated from 1 A/g GV cycling. Here, the asymmetric device shows a better cycle ability and actually has a larger specific capacitance after 1250 cycles.

The improved cycle ability and rate capability of the asymmetric device over the symmetric device can be explained by a closer examination of the chemistry taking place at the cathode and anode in each device during use. In each device it is assumed that a fast faradaic reaction at the surface of the electrode nanomaterials is only reaction contributing to the charge. However, if one monitors the referenced cycle potential windows for the cathode and anode during cycling, the reactions contributing to the charge can be monitored. This is accomplished by using a bipotentiostat where the potential is controlled to be between 0 and 1 absolute voltage between the anode and cathode with each electrode's relative potential monitored by a reference electrode.

Figure 3.4 shows the referenced potential window for the coaxial anode of the symmetric device during CV cycling. These qualitative experiments were done in beaker cells at a one ninth scale with the same electrolyte as the device sans PMMA.

As can be seen in Figure 3.4 the referenced potential window changes with each cycle. In the first cycle, the coaxial anode's potential window is from -0.25 to 0.15 V vs. Ag/AgCl. According to the literature, the ideal cycle stability window for MnO_2 in aqueous solution is between 0 and 1 V vs. Ag/AgCl which means in a symmetric capacitor that the anode should be between 0 and 0.5 V vs. Ag/AgCl. Figure 3.4 shows that even in the first cycle the MnO_2-PEDOT coaxial anode is outside MnO_2's reversibility window.

Furthermore, as the cycle number increases, the referenced cycle window moves to increasingly detrimental negative potentials. Also, the negative peak at the bottom right of the curve slowly increases during the first 50 cycles. This peak at negative potentials has been associated with the formation of Mn^{2+},[184] which is not electroactive. This irreversible conversion reduces the amount of active material in the electrode. This reaction is also a slow bulk faradaic reaction which could explain the low rate capability for the symmetric device. Furthermore, from the 50^{th} to the 500^{th} cycle, this same peak decreases, probably due to the complete transformation of all the active manganese species to Mn^{2+}. It may also be noted that the shape of the curve becomes increasingly rectangular, which is characteristic of a PEDOT-only electrode. Thus, it can be inferred that after 1000 cycles only the PEDOT in the coaxial structure remains electrochemically active.

Another trend is the increasing size of the potential window. Ideally the anode

voltage window would be 0.5 V in width, since the absolute cycling voltage for this symmetric device is maintained between 0 and 1 V. In this ideal case, both electrodes would carry the same amount of charge and the same voltage window indicating that both would have the same capacitance. However, in the symmetric device, the anode's window is only 0.4 V during the first cycle indicating that the anode has a larger capacitance than the cathode. This larger capacitance is deceiving because the charge is coming from an irreversible faradaic reaction. Furthermore, as the cycle number increases, the cycle window increases from 0.4 V to 0.7 V indicating a decreasing capacitance for the anode. Again, this can be explained by a decrease in the active manganese species, since this decrease reduces the amount of the high capacitance material, leaving only the moderately capacitive PEDOT material carrying the charge.

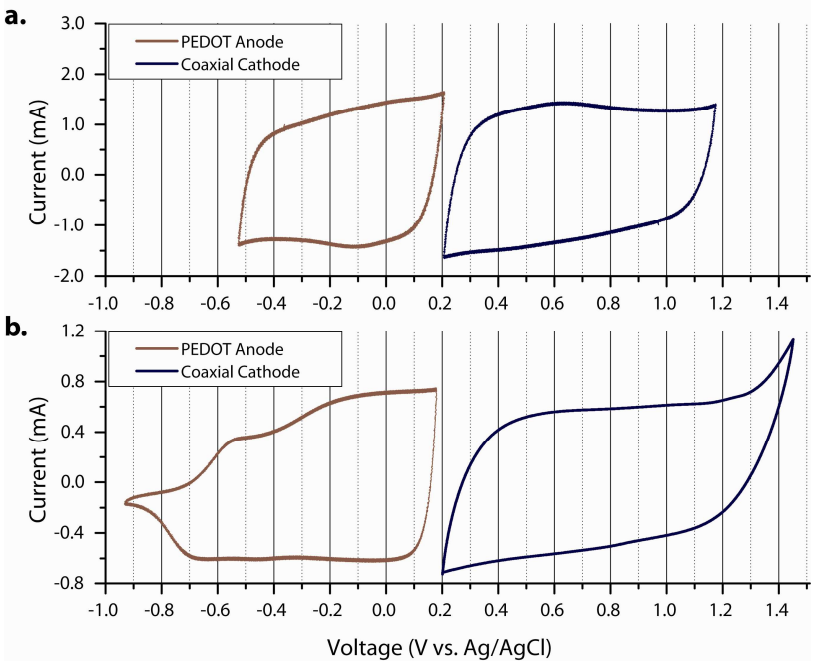

Figure 3.5 Anode and Cathode CV Cycling with Different Voltage Windows

(a) **"***In Situ"* CV curves at a 50 mV/s scan rate exhibiting the referenced potential window vs. Ag/AgCl for the coaxial nanowire cathode (Blue) and PEDOT nanowire anode (Red) when cycled between the absolute potential bias between cathode and anode of 0.0 – 1.7 V and (b) three-electrode cyclic voltammetry at 20 mV/s of a PEDOT nanowire electrode (Red) cycled between -0.95 – 0.20 V vs. Ag/AgCl and a coaxial nanowire electrode (Blue) cycled between 0.20 V and 1.45 V vs. Ag/AgCl.

Therefore, the degredation in capacitance of the coaxial anode can mainly be attributed to the large PEDOT electrochemical stability window. This large potential window allows the coaxial structure to choose an anode voltage that is in MnO_2's electrochemical irreversibility window. Thus the coaxial PEDOT-MnO_2 structure can not be considered for use as an anode in a symmetric supercapacitor device system. Though this is not entirely discouringing information, since MnO_2 itself as an anode

material for supercapacitors has been seen as an issue.[184] However, the coaxial cathode maintains its cycle window in MnO_2's prefered electrochemical stability window, thus showcasing its ability as a great cathode for supercapacitors. Therefore an asymmetric device using the coaxial structure as the cathode is ideal as a possible high power energy storage device.

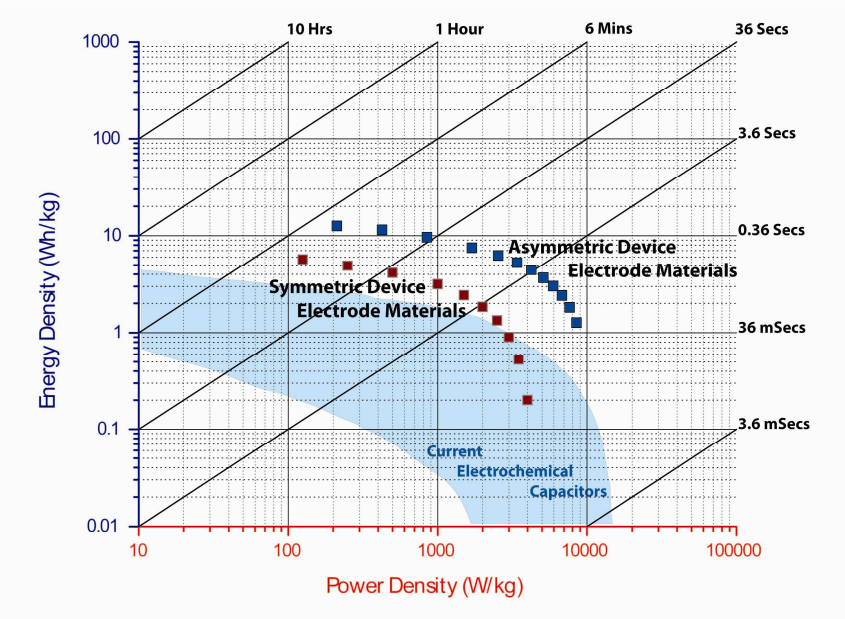

Figure 3.6 Asymmetric and Symmetric Device Plotted on Ragone Plot

Ragone plot of energy density versus power density, comparing the symmetric Coaxial-Coaxial (Red) and asymmetric Coaxial-PEDOT (Blue) device electrode materials to current electrochemical capacitors (Teal Area) found in ref. 5.

One of the advantages of PEDOT as an anode material is its very large voltage window. Therefore in the asymmetrical device, the voltage window can be expanded. A practical voltage up to 1.7 V is found to be possible for the asymmetric device.

Figure 3.5 shows the *"in situ"* cycle potential windows relative to a Ag/AgCl reference for the anode and cathode. Again, this is accomplished by using a bipotentiostat where the potential is controlled to be between 0 and 1.7 absolute volts between the anode and cathode, but each electrode's relative potential is monitored versus a reference. These qualitative experiments were done in beaker cells at one ninth the electroactive area with the same electrolyte as the device sans PMMA.

If the voltage is increased above 1.7 V, detrimental effects appear for both the cathode and anode. As can be seen in Figure 3.5b, an oxidation peak begins to appear above 1.2 V vs. Ag/AgCl for the cathode which has been attributed to the irreversible oxidation of MnO_2 to an electrochemically inactive higher oxidation state of manganese. As for the anode, PEDOT begins the dedoping process below -0.5 V vs. Ag/AgCl causing a loss of conductivity that reduces its capacitance. Therefore, 1.7 V is the maximum potential that can be established from this asymmetric device.

In order to compare our devices to other current capacitors, their energy and power densities were calculated. The calculation for the energy density of a supercapacitor device is:

$$E_d = \frac{CV^2}{2m}$$

Where E_d is the energy density, C is the capacitance, m is the mass of the electrode materials, and V is the maximum voltage. This equation shows that any increase in the maximum voltage window for a supercapacitor results in an exponential increase in energy density. This voltage window is shown to be increased from 1.0 V for the

symmetric Coaxial-Coaxial device to 1.7 V using the asymmetric Coaxial-PEDOT device. Therefore, the asymmetric device can have roughly a three times (2.9x) improvement in energy density over the symmetric device if one assumes the same capacitance for each device. The Ragone plot in Figure 3.6 shows how the symmetric and asymmetric device electrode materials compare to current electrochemical capacitors.[1] At relatively low power densities (213 W/kg), the symmetric device shows a larger energy density (7.7 Wh/kg) than current capacitors; however, at high rates this energy decreases rapidly. This low rate capability is explained above to be due to bulk faradaic reactions which contribute to the charge at low rates but are too slow to contribute to the charge at high rates. However, the asymmetric device shows a higher energy density for its electrode materials than current electrochemical capacitors at low and at high power rates (E_d = 12.6 Wh/kg at 210 W/kg and 1.3 Wh/kg at 8500 W/kg), indicating that this device has tremendous potential to power current small electronics. The total asymmetric device including electrolyte and all of the packaging materials (mass = 0.47 g) has an energy density of 0.22 Wh/kg at a power density of 3.7 W/kg. Improvement and optimization of the current bulky packaging and rudimentary electrolyte is expected, which should decrease the weight significantly and improve the total energy and power densities dramatically.

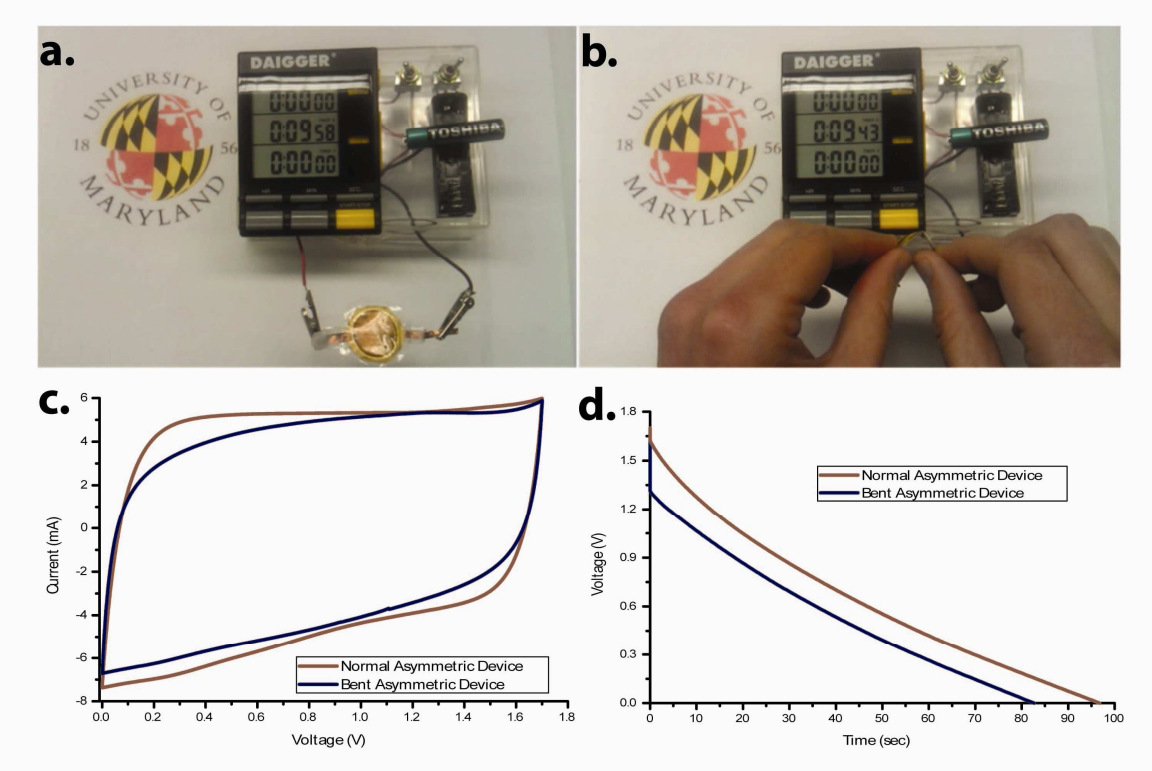

Figure 3.7 Electrochemical Performance during Normal and Bent States

(a) Asymmetric PEDOT anode-coaxial cathode device powering a laboratory timer, (b) the same timer being powered by the asymmetric device in the highly flexed state, (c) CV curves at a 20 mV/s rate for both the normal state (orange) and the bent state (blue), and (d) GV curves for the normal (orange) and bent state (blue) at a 0.5 A/g discharge rate.

In order to apply a supercapacitor device to mobile electronics which are projected to become flexible, this energy source needs to show its capabilities in both the normal and flexed state. Figure 3.7 (a and b) shows the asymmetric device powering a laboratory timer in both the normal and highly flexed states, respectively. It is demonstrated that this device can power a laboratory timer including its high power

drain speakers for 10 minutes with only a fast charge of 3 seconds.

Figure 3.7c illustrates the difference in the CV curve between the normal and the bent state close 90^{o}. The curve becomes less rectangular in the bent state indicating a decrease in rate capability. From the galvanostatic discharge curves in Figure 3.7d, the specific capacitance is shown to decrease from 114 F/g for the normal state and 98 F/g for the bent state at the 0.5 A/g charge rate. This shows the device can deliver 86% of its energy even in the bent state. This demonstrates a great ability for this device to be used in future flexible electronics.

3.3 Conclusion

Flexible supercapacitor devices based on freestanding nanowires are shown here to produce enough energy and power to operate small electronic devices. An asymmetric device consisting of a PEDOT nanowire array anode and coaxial PEDOT/MnO_2 nanowire array cathode exhibited an improvement in energy density, power density, and cycle life when compared to a symmetric device consisting of a coaxial nanowire array as the cathode and anode. The improvement in energy density can be attributed to the increase in the electrochemically reversible voltage window; however, the increase in power and cycle ability can be attributed to the PEDOT anode, since the coaxial PEDOT/MnO_2 nanowire array is shown here to be unsuitable as an anode. This is due to the fact that the voltage window chosen by this heterogeneous anode is centered in MnO_2's irreversible reduction window. This reduces the symmetric cell's cycle ability due to MnO_2's slow conversion to inactive Mn^{2+} and limits its power capability, since a slow faradaic process is contributing to the charge.

This superior asymmetric device is highly flexible and shows fast charging and discharging while still maintaining 86% of its energy in the bent state. The asymmetric device has a total mass including packaging of 0.47 g with a total capacitance of 0.26 F and a maximum voltage of 1.7 V, which is capable of providing enough energy to power small portable devices. This device's electrode materials display an energy density of 9.8Wh/kg even at a high power density of 850 W/kg. Furthermore, this device maintains 86% of its energy density even under a highly flexed state, demonstrating its ability to be used as a high-power energy source in future flexible electronic devices. In addition, we believe the energy and power density of the full cell including packaging and electrolyte can be improved further with the optimization of the packaging and electrolyte materials.

Chapter 4: Self-Limiting Electrodeposition of Hierarchical MnO_2 and $M(OH)_2/MnO_2$ Nanofibril/Nanowires: Mechanism and Supercapacitor Properties

It is well-documented that the adsorption, insertion, and conversion reactions associated with catalysis[185], energy storage[186, 187], energy conversion[188], chromatography[189], and chemical sensing[190, 191] can be enhanced by using hierarchical nanostructures. This multi-scale texturization allows for a synergistic joining of two different length scales. The larger length scale offers an efficient way of transporting the ions (i.e. macropores) or electrons (i.e. one-dimensional structures) while the smaller scale offers either small voids (i.e. micropores) for high ion accessibility with high material density or a higher surface area (i.e. nanoparticles) for greater adsorption or access of ions.

Oxides of manganese (MnO_x) are deeply versatile compounds for material and chemical scientists and are being investigated as important materials for these hierarchical structures.[95, 192, 193] MnOx materials have many favorable qualities that make them desirable products in the chemical science field such as low toxicity, high abundance, low cost, environmental friendliness, and their ability to be synthesized many different ways (electrochemical, chemical, sol-gel, hydrothermal, etc.).[33, 61, 62]

In terms of energy storage, manganese oxides have a long history as they were used in the first Leclanché alkaline battery cell developed in the 1860s.[65] Currently, they are being studied as cathode materials for lithium ion batteries[194-196] and as fast charging

materials for supercapacitors[40, 69, 197]. In this latter application, they have underperformed as most research articles demonstrate capacitances of ≤470 F/g which is far short of their theoretical capacitance of 1110 F/g.[198] It is thought that these meager numbers can be improved by nanosizing its structure as the energy storage mechanism is localized at the surface of the material.[199]

However, it must be kept in mind that these nanosized MnO_2 particles must be interconnected in some fashion in order to maintain their electrochemical activity. Therefore, by utilizing a hierarchical structure, one MnO_2 architectural dimension can provide a continuous interconnected substrate on which the smaller MnO_2 architecture dimension can be deposited. This could result in a synergic relationship between the two architectures.

Hierarchical MnO_2 nanostructures have been successfully synthesized previously. Fei *et al.* have created hollow MnO_2 microspheres and microcubes with nanometer scale shell thickness by reacting solutions of $KMnO_4$ with $MnCO_3$ microspheres and microcubes followed by dissolution of the $MnCO_3$.[95] Li et al. were able to create core-shell MnO_2 microspheres with spherically aligned MnO_2 nanorods on the surface by a one-step solution method utilizing a Ag catalyst.[200] Yu et al. created urchin-like clusters of MnO_2 nanorods by a hydrothermal method.[96] A great review containing other hierarchical MnO_2 nanostructures and additional recent advances in metal oxide architecture design was done by Jiang *et al.*.[97] However, each of these methods is limited to manganese oxide materials and there have limited control over the dimensions of the structures. Thus it is highly desirable to develop a model electrochemical method to build high surface area hierarchical structures with various

materials, aspect ratios, along with other architectural considerations in order to maximize each architecture's contribution to the whole structure.

We describe here a simple self-limiting electrochemical pathway of producing hierarchical MnO_2 nanostructures by exploiting the rich oxidation state chemistry of manganese oxide. This hierarchical material consists of template-synthesized nanowire arrays of MnO_2 conformally coated with nanofibrils of MnO_2. The template method provides great control over the parameters for each of the architectures including their diameter, length, and thickness. The adjustable length and diameter of the nanowires provide a continuous substrate for electron transfer onto which various amounts of the higher surface area nanofibrils are attached. This method does not require any use of binders or conductive additives as our electrodes consist of freestanding bare and hierarchical MnO_2 nanowires directly contacted to a gold current collector. This reduces any errors involved in the calculation of capacitance values that could be associated with double layer capacitance from the conductive carbon or blockage of electrolyte from the polymeric binder.

The mechanism of formation for these nanofibrils is elucidated by electrochemical measurements, Raman spectroscopy, electron energy loss spectroscopy (EELS), and electron microscopy.

The MnO_2 hierarchical structures were then investigated at low scan rates (<10 mV/s) as supercapacitor materials in both an aqueous and organic (acetonitrile) solvent. The charge storage mechanism of the nanofibrils is shown to differ depending on the solvent used. These results indicate that the solvent chosen has a great effect on the

charge storage mechanism and can be the major defining factor on whether the material obtains its theoretical capacitance.

Next, the hierarchical structure was tested at high scan rates in aqueous solution while varying parameters such as the length of the nanowires, the diameter of the nanowires, and the amount of nanofibrils deposited. These results indicate: 1) A shorter length can increase the specific capacitance, but at the cost of the areal capacitance. 2) A smaller diameter nanowire increases the specific capacitance of the bare nanowires and that of the whole hierarchical structure, but does not improve the supercapacitor performance of the nanofibrils. 3) The amount of nanofibrils deposited increases the specific capacitance of the hierarchical material; however, at excessive amounts the nanofibrils become detrimental to the overall specific capacitance.

In addition, unlike synthesis methods for other hierarchical MnO_2 nanostructures, this electrochemical synthesis method can be easily applied to other MnO_2 systems and is shown here to produce additional hierarchical/heterogeneous $Ni(OH)_2/MnO_2$ and $Co(OH)_2/MnO_2$ nanofibril/nanowire arrays.

4.1 Experimental

4.1.1 Chemicals and materials

All chemicals were purchased with high purity requiring no need for further purification. Manganese acetate, nickel chloride, cobalt chloride, lithium perchlorate, sodium chloride, potassium hydroxide, battery-grade acetonitrile, and sodium hydroxide were purchased from Sigma Aldrich (St. Louis, MO). De-ionized water (about 18 MΩ cm^{-1} in resistivity) was made by a Milli-Q water purification system (Millipore;

Billerica, MA). Porous anodized aluminum oxide (AAO) membranes of 200 nm in pore diameter and 60 μm in thickness are commercially available from Whatman (Maidstone, Kent, UK), while membranes with 80 nm pore diameters and 50 µm thickness are available from Synkera (Longmont, CO).

4.1.2 Synthesis

4.1.2.1 Synthesis of freestanding MnO_2 nanowire array

This synthesis is represented by Figure **4.2**a. First, a Denton Desk III sputter machine is used to sputter a ≈300 nm gold layer on the branched side of an AAO membrane. A strip of copper tape, to provide good electrical contact, is then attached to the gold side of the membrane. This piece is then sandwiched between layers of Parafilm with part of the non-sputtered side exposed with a defined window of 0.2 cm^2 resulting in completion of the working electrode.

The working electrode is then placed in a 100 mM manganese acetate bath with a Ag/AgCl reference and a platinum counter electrode. A constant voltage of 0.60 V vs. Ag/AgCl is applied until the total charge passed was 750 mC/cm^2 for 4.5 micron long MnO_2 nanowires or 250 mC/cm^2 for 1.5 micron length nanowires. A soaking time of 30 minutes in a 3 M solution of sodium hydroxide resulted in the complete dissolution of the alumina membrane producing vertically aligned MnO_2 nanowires attached to a gold current collector.

4.1.2.2 Synthesis of MnO_2, $Ni(OH)_2$, and $Co(OH)_2$ nanofibril/nanowire Arrays

A MnO_2 nanowire array with a defined window of 0.32 cm^2 is submerged into a 100 mM manganese acetate, nickel chloride, or cobalt chloride bath with a Ag/AgCl reference and a platinum counter electrode. A voltage of -0.85 V vs. Ag/AgCl was then applied until various amounts of charge are passed. Subsequently, sweeping the potential to 1.0 V vs. Ag/AgCl resulted in the synthesis of the MnO_2 nanofibril/nanowire array.

4.1.3 Characterization

4.1.3.1 Electron microscopy

Imaging of the hierarchical MnO_2 nanomaterial was done using a scanning electron microscope (Hitachi SU-70 FEG-SEM) and a transmission electron microscope (JEM 2100 FE-TEM).

4.1.3.2 Electrochemical measurements

All of the electrochemical testing was done utilizing a bi-potentiostat (BI-STAT, Princeton Applied Research) in a three electrode configuration. The working electrode consisted of as-deposited free-standing bare MnO_2 nanowire arrays and hierarchical MnO_2 nanofibril/nanowire arrays on a gold current collector. A Ag/AgCl electrode was used as the reference electrode and a platinum foil was used as the counter electrode. Electrochemical testing was done in both an aqueous and an organic acetonitrile 1 M $LiClO_4$ solution. All capacitance values were obtained using the data from the cyclic voltammetry curves and the following equation:

$$\frac{\int_0^1 I\, dV}{v * mass} \quad (4)$$

where I is the current, V is the voltage vs. Ag/AgCl, υ is the scan rate, and *mass* is the mass of the material.

4.1.3.3 Inductively coupled plasma-Atomic emission spectroscopy (ICP-AES)

ICP-AES measurements were performed using a PerkinElmer ICP-Optima 4700. Intensities were measured at 257.610 nm for Mn and 231.604 nm for Ni. Calibration curves were made from Mn and Ni standards traceable to the National Institute of Standards and Technology (NIST). All electrodes were dissolved in 3:1 concentrated HCl:HNO_3 and diluted to a known volume before being administered to the plasma.

4.1.3.4 Raman spectroscopy

A Horiba Jobin-Yvon LabRAM HR-VIS microRaman system was used to characterize these manganese oxide materials along with MnO, Mn_3O_4, Mn_2O_3 and MnO_2 standards purchased from Sigma-Aldrich. The green line (514.5 nm) of an argon laser was utilized to excite the sample using a spot size of ≈1 μm^2. The spectrum was taken between the Raman shifts of 300 and 900 cm^{-1}.

4.1.3.5 Electron energy loss spectroscopy

MnO_2, Mn_2O_3, and Mn_3O_4 standards were purchased from Sigma-Aldrich. These standards were each ground with a mortar and pestle in methanol and drop cast on a holey carbon TEM grid.

The MnO_x nanowire samples are grown in AAO by the method above; however, before dissolving the AAO the electrode is placed in a solution of Mn^{2+} and reduced at 0.85 V vs. Ag/AgCl until a charge of 100 mC/cm^2 is passed (Figure **4.5**a).

The resulting nanowires are then released from the AAO template using 3 M NaOH for 12 minutes. These nanowires are then placed on a holey carbon TEM grid.

A Field Emission Gun-Transmission Electron Microscope (FEG-TEM) JEOL JEM 2100F TEM/STEM was used with a Gatan electron energy loss spectrometer to obtain the EELS spectrum.

4.1.3.6 X-ray photoelectron spectroscopy (XPS)

XPS analysis was done on a Kratos AXIS 165 spectrometer. The C 1s peak was calibrated to 284.8 eV. CasaXPS software was used to obtain the components for the fitted curves.

4.2 Results and Discussion

4.2.1 Synthetic mechanism of hierarchical MnO_2 nanowire/nanofibril arrays

Hierarchical MnO_2 nanowire/nanofibril arrays are synthesized by the following method. First, vertically aligned nanowire arrays of manganese oxide attached to gold are synthesized using a common anodic deposition process (Figure **4.2**a).[123, 201]

A nanofibril MnO_2 coating is then produced by the application of -0.85 V vs. Ag/AgCl in a Mn^{2+} solution to the bare MnO_2 nanowire arrays which are then oxidized by a potential sweep to 1 V vs. Ag/AgCl in a 1 M $LiClO_4$ electrolyte.

The proposed mechanism of formation for these hierarchical arrays is represented by Figure **4.2**b and begins with the aforementioned electrochemical reduction of MnO_2 in an Mn^{2+} solution which is represented by '1' in Figure **4.2**b. This results in two simultaneous reactions represented by the following reactions:

$$2MnO_2\ (s) + H_2O\ (l) + 2e^- \rightarrow Mn_2O_3\ (s) + 2OH^-\ (aq) \quad (1a)$$

$$Mn^{2+}\ (aq) + 2OH^-\ (aq) \rightarrow Mn(OH)_2\ (s) \quad (1b)$$

Reaction 1a represents the reduction of the MnO_2 nanowires to Mn_2O_3, while reaction 1b represents the synthesis of $Mn(OH)_2$ nanofibril coating. The first reaction is a well established mechanism found in alkaline batteries which releases hydroxide ions[157] that are needed for reaction 1b. The reduction potential used here was -0.85 V vs. Ag/AgCl which was chosen as a way to increase the reaction kinetics of the bulk

OH^- production while avoiding the reduction of water. This is demonstrated by the linear sweep voltammetry found in **Figure 4.1** where the peak at -0.1 V is attributed to equation 1a, the reduction of MnO_2 to Mn_2O_3.

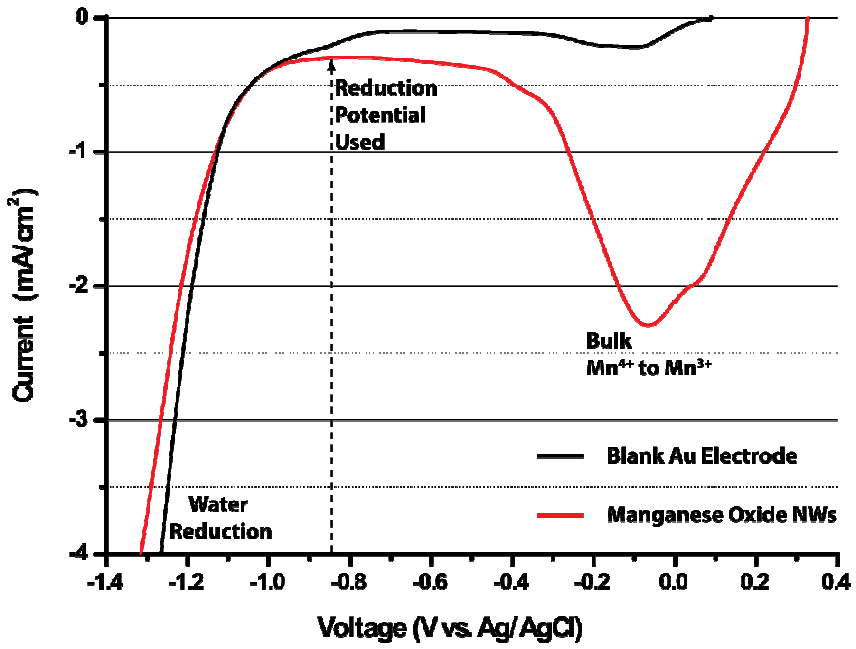

Figure 4.1. Linear Sweep Voltammetry of Blank and MnO_2 Electrode

Reaction 1b is proposed based on manganese's Pourbaix diagram which shows that increasing the pH of a Mn^{2+} solution results in the formation of $Mn(OH)_2$[60]. In this case, the pH is only increased locally around the reducing MnO_2 nanowires resulting in $Mn(OH)_2$ production localized at the surface of these nanowires.

Consequently, since reaction 1b relies on the production of hydroxide ions from reaction 1a, the amount of nanofibrils that can be produced is limited by the amount of MnO_2 available initially. Therefore the production of the $Mn(OH)_2$ nanofibrils is self-limiting.

This is further supported by the following simple experiment: by controlling the amount of charged passed (750, 375, and 225 mC/cm^2) during the electrodeposition, different amounts of MnO_2 are synthesized in anodized aluminum oxide (AAO) templates and then directly reduced in the same Mn^{2+} electrodeposition solution. The curves for current and charge density versus time during the reduction are represented by Figure 4.3 where a, b, and c correspond to the initial electrodeposited MnO_2 amounts of 750, 375, and 225 mC/cm^2, respectively. The current dramatically falls to near zero when the charge reaches or approaches half the charge density of the electrodeposition (a. 350, b. 200, and c. 120 mC/cm^2).

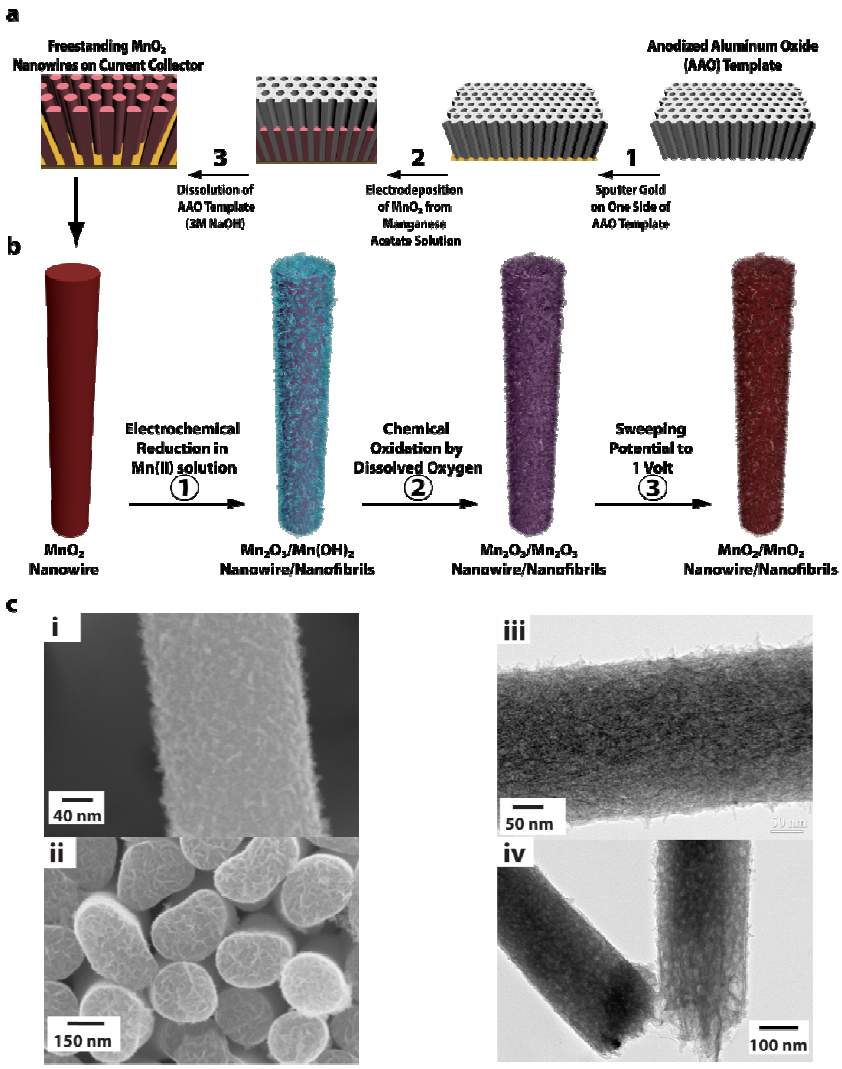

Figure 4.2. Synthetic Mechanism with SEM and TEM Images

(a) Schematic diagram representing the electrochemical template synthesis of arrays of MnO_2 nanowires; (b) schematic diagram demonstrating the Electrochemical Synthesis of MnO_2 nanofibrils on MnO_2 nanowires; (c) SEM and TEM images of hierarchical MnO_2 nanowire/nanofibrils: i High magnification SEM image of nanofibrils on a single nanowire, ii SEM top-view of an array of MnO_2 nanofibril/nanowires, iii TEM image of the nanofibrils along the axis of and MnO_2 nanowire and iv TEM image of the end structure of two nanofibril coated nanowire

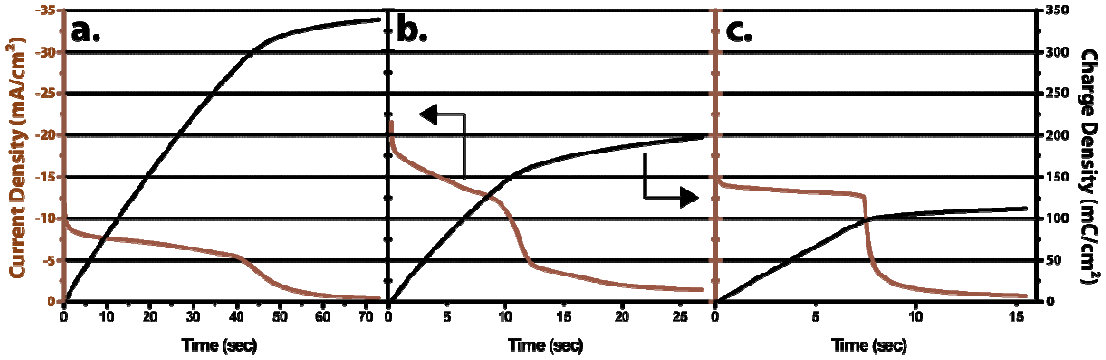

Figure 4.3 Reducing Charge and Current Density at Different Loading Amounts

Curves for current (red) and charge (black) density versus time during the electrochemical reduction of MnO_2 in an AAO template where a, b, and c correspond to the initial electrodeposited MnO_2 amounts of 750, 375, and 225 mC/cm^2, respectively

This correlates well with the assumption that during the electrodeposition, the manganese species oxidizes from Mn^{2+} to Mn^{4+}, while during the reduction, the Mn^{4+} reduces to Mn^{3+}. In other words, only half the charge passed during electrochemical deposition can be used during the reduction process. This means that the amount of hydroxide that can be formed by reaction 1a is limited to the amount of MnO_2 (Mn^{4+}) that is initially electrodeposited. Next, the manganese hydroxide nanofibrils formed in 1b are highly unstable and react within minutes with dissolved oxygen to form Mn_2O_3 which corresponds to process '2' in Figure **4.2**b. This is represented by the following reaction.[202]

$$4Mn(OH)_2\ (s) + O_2\ (g) \rightarrow 2Mn_2O_3\ (s) + 4H_2O\ (l) \qquad (2)$$

The final step in the formation of the MnO_2 nanowire/nanofibril arrays, represented by '3' in Figure **4.2**b, is the total oxidation of the Mn_2O_3 nanowires and nanofibrils to MnO_2 during the first potential sweep of the electrode to 1V vs. Ag/AgCl. This is just the reverse of reaction 1a, represented by the following reaction:

$$Mn_2O_3\ (s) + 3H_2O\ (l) \rightarrow 2MnO_2\ (s) + 2H_3O^+\ (aq) + 2e^- \qquad (3)$$

The resulting MnO_2 nanowire/nanofibril structures can be seen in the SEM and TEM images in Figure **4.2**c. The structures consist of MnO_2 nanowires coated with a conformal layer of MnO_2 nanofibrils. Thus, the MnO_2 nanowires provide a high surface area substrate on which the smaller nanofibrils precipitate. The thickness of the nanofibril layer is estimated to be between 5-10 nm from SEM imaging; however, due to blurring effects at these high magnifications there is a large error in this measurement.

4.2.2 Characterization of the MnO_2 nanofibril/nanowire structure with Raman and EELS

Since our material displays small crystal sizes without any long range order, analysis by X-ray diffraction was not possible as the results showed no clear diffraction peaks. Thus Raman spectroscopy was chosen here to analyze the formation mechanism of our MnO_x material due to its ability to show average crystal structure over a large area. Raman spectrum 3a represents MnO_2 nanowires as initially electrodeposited. The peaks seen at 573 cm^{-1}, and 649 cm^{-1} correspond well with literature values for the δ-phase

MnO_2 Raman spectrum[203, 204] as well as our own Raman analysis of manganese standards found in Figure **4.4**. This phase consists of layered sheets of MnO_6 octahedra. Accordingly, the peak at ≈575 cm^{-1} has been attributed to Mn-O stretching in the basal plane of the MnO_6 sheet, while the peak at ≈650 cm^{-1} has been attributed to MnO_6 symmetric stretching vibrations.[203]

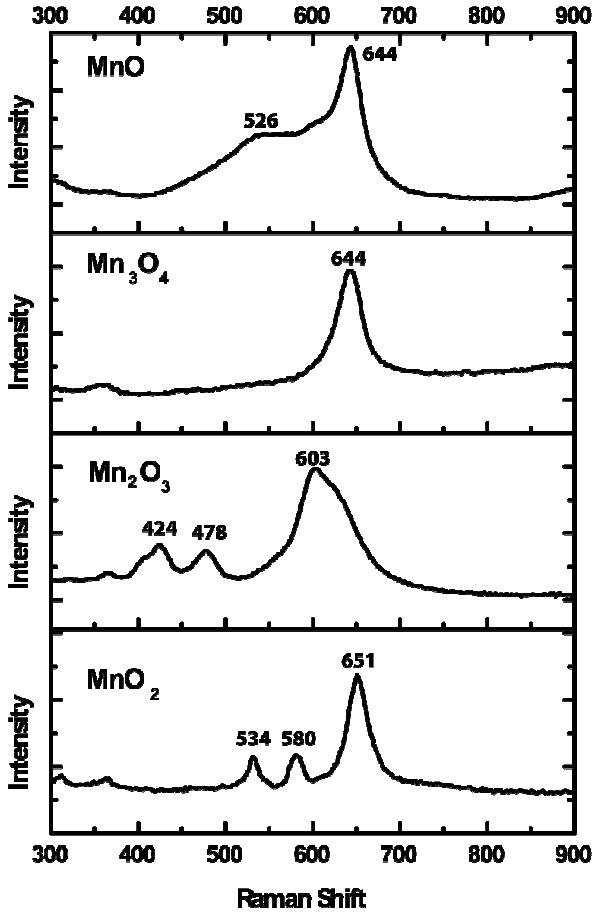

Figure 4.4. Raman spectra of MnO, Mn_3O_4, Mn_2O_3, and MnO_2 Standards

Figure 4.6 (b and d) represents the Raman spectra of MnO_2 nanowires reduced in Mn^{2+} and Li^+ respectively. MnO_2 is reduced in Li^+ here to better illustrate the oxidation state of the underlying nanowires as no MnO_x nanofibrils will be formed during this reaction. This can be found in Figure **4.5** where MnO_2 nanowires embedded in AAO were reduced in Manganese ion and Manganese ion-free solutions; and production of $Mn(OH)_2$ was only seen in the former. Thus, the material reduced in Li^+ has peaks at 590 and 623 cm^{-1} which suggest that the MnO_2 nanowire is reduced to Mn_2O_3[205], while the MnO_2 reduced in Mn^{2+} showcases a broad peak at 608 cm^{-1}.

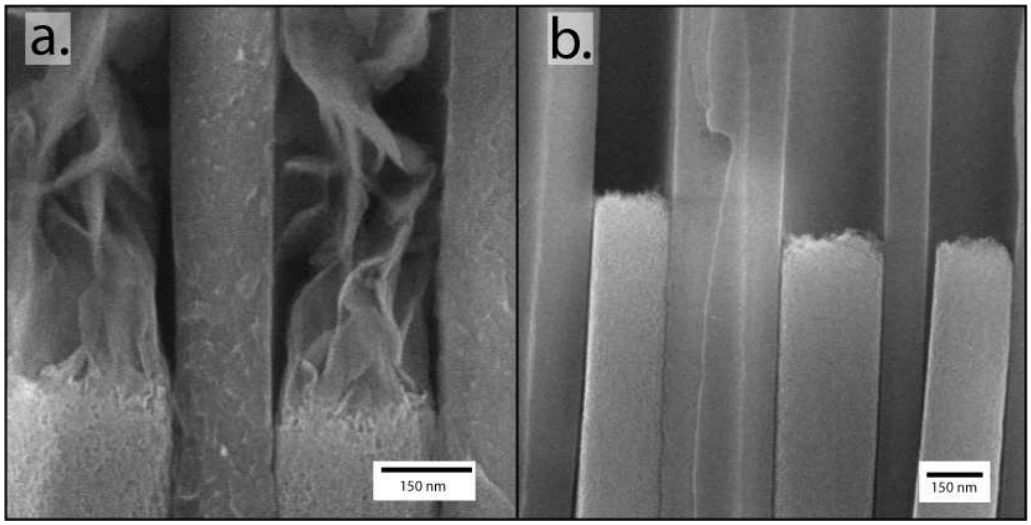

Figure 4.5. SEM Side-view of Reduced MnO_2 Nanowires in AAO

MnO_2 nanowires embedded in AAO reduced at -0.85 V in (a.) Mn^{2+} solution and (b.) Li^+ solution

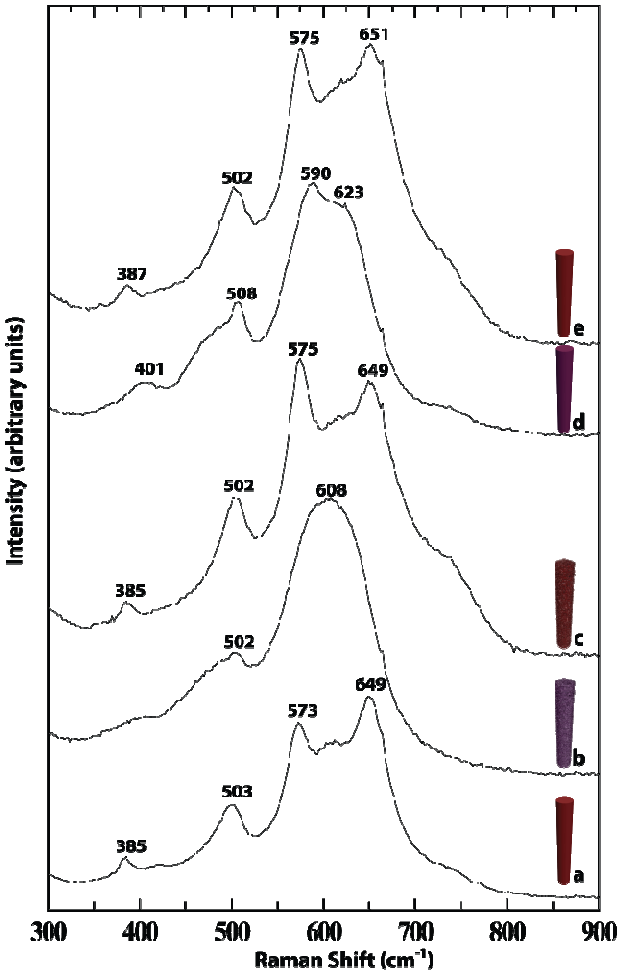

Figure 4.6 Raman Spectroscopy Investigation

Raman Spectroscopy of (a) Electrodeposited MnO_2; (b) MnO_2 reduced in a Mn^{2+} solution; (c) 'b' After sweeping the potential to 1 V vs. Ag/AgCl; (d) MnO_2 reduced in Li^+ solution; (e) after sweeping the potential of 'd' to 1 V vs. Ag/AgCl

This reduction of the MnO_2 nanowire to Mn_2O_3 process is further examined by electron energy loss spectroscopy (EELS) as is shown in Figure 4.7. First, the EELS spectrum of three standard samples purchased from Sigma-Aldrich consisting of MnO_2, Mn_2O_3, and Mn_3O_4 were obtained. These spectra show the characteristic O – K and Mn

- $L_{2,3}$ edges. The different edge details for each of the standards for the O – K edge can be used as a fingerprint to obtain valence information for unknown samples.[206, 207]

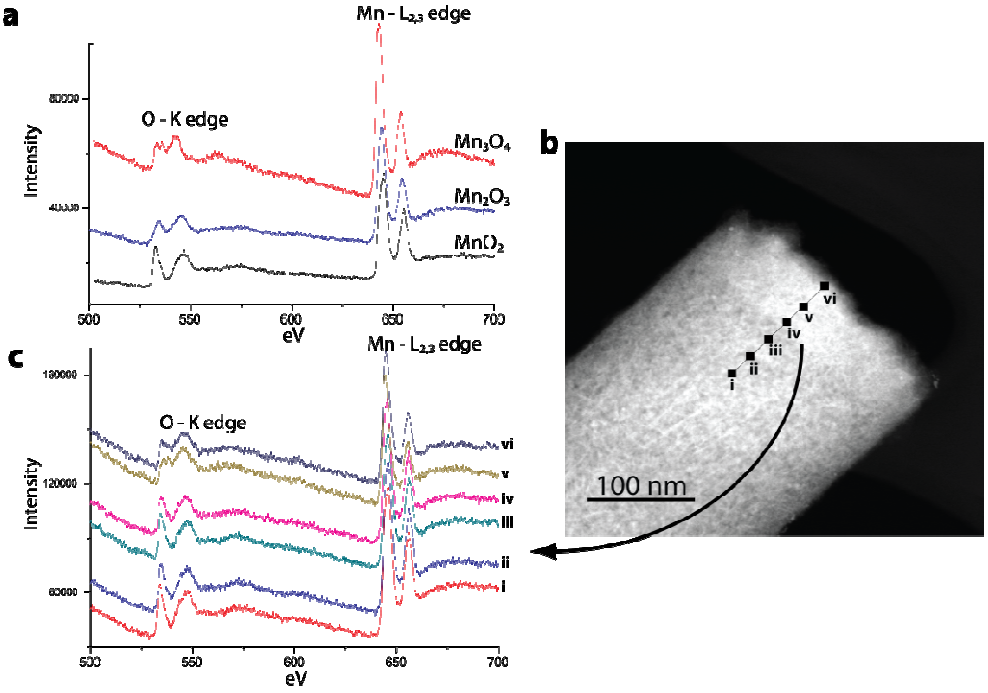

Figure 4.7 Electron Energy Loss Spectroscopy of Hierarchical MnO_2

(a) Electron Energy Loss Spectroscopy (EELS) spectra of standards of MnO_2, Mn_2O_3 and Mn_3O_4; (b) Dark Field Image of end structure of MnO_2 nanowire reduced in Mn^{2+} in an AAO template; (c) EELS spectra of points i – vi found in 'b' indicating phase of MnO_x along the axis of the nanowire

Figure 4.7b is the dark field TEM image of an MnO_2 nanowire partially reduced in Mn^{2+} before release from the AAO template. In this case, only the end of the nanowire which is exposed to the Mn^{2+} solution is reacted (an SEM image of this can be found in Figure **4.5**a). This in-template reduction method was used to promote a sharp interface

between the MnO_2 nanowire and the reduced MnO_x that is formed during the reduction stage of the hierarchical synthesis. As can be seen in Figure 4.7b, there is a sharp visual contrast between the MnO_2 nanowire and the reduced MnO_x part of the nanowire.

Points along the axis of this nanowire were probed using EELS as can be seen in Figure 4.7c. These points progress from the MnO_2 portion of the nanowire (i) to the edge where the MnO_2 is reduced (vi). As exhibited from the data, the shape of the O – K edge transforms from that characteristic of MnO_2 to that characteristic of Mn_2O_3. Thus the EELS data shows that the MnO_2 nanowire is converted to Mn_2O_3 during the reduction process. This EELS data correlates well with our assumption that the MnO_2 nanowire reduces to Mn_2O_3 upon application of a negative potential.

A closer examination of the Raman data in Figure 4.6 (b and d) reveals that the peak at 608 cm^{-1} for the Mn^{2+} reduced MnO_2 is a possible convolution of the two peaks in the spectrum of the Li^+ reduced MnO_2. This convolution may be caused by the smaller particle size and reduced crystallinity of the nanofibrils. In fact, in our own Raman analysis of an Mn_2O_3 standard we saw this same convoluted peak (see Figure **4.4**). This suggests that the nanofibrils are Mn_2O_3 which correlates well with our assumption of $Mn(OH)_2$ nanofibril formation followed by a rapid oxidation to Mn_2O_3.

Finally, the materials represented by Raman spectrum in Figure 4.6 (b and d) are potentially swept to a voltage of 1.0 V vs. Ag/AgCl. This represents a typical first charge of a supercapacitor electrode. The spectra represented by Figure 4.6 (c and e) demonstrate that both materials are oxidized to MnO_2 by evaluating their characteristic MnO_2 Raman peaks of ≈575 and ≈650 cm^{-1}.

X-ray photoelectron spectroscopy (XPS) studies were also done to try to correlate this Raman and EELS data; however, we found the results inconclusive as the peak separation of the Mn 3s multiplet only varied between 5.2 and 5.4 eV indicating a valence state of 3^+ for Mn[152] under all electrochemical states. This can be attributed to the high surface area of our material, which is most likely to contain the MnOOH due to the synthesis in an aqueous solvent. Ion milling of our samples for this XPS work was initially thought to show the true valence state below the surface; however, Oxygen is sputtered more preferentially than Manganese which would show an artificially lower valence state in the bulk resulting in less than true valence state measurements. Nonetheless, these Raman and EELS results support our proposed mechanism of formation for these hierarchical MnO_2 nanowire/nanofibril arrays.

4.2.3 EDS and XPS from Applications to other systems

As a final support of our synthesis mechanism, it was demonstrated in other systems. Herein, MnO_2 nanowire arrays are reduced in Ni^{2+} and Co^{2+} solutions. Figure 4.8a (MnO_2 reduced in Ni^{2+}) and Figure 4.8c (MnO_2 reduced in Co^{2+}) show the energy dispersive X-ray spectroscopy (EDS) line scans for these hierarchical heterogeneous structures. Both graphs illustrate a MnO_2 nanowire core with an oxide of nickel or cobalt nanofibril shell, respectively.

The oxidation state of these nanofibril shells is probed by XPS. The results show that the main peak found in Figure 4.8b (MnO_2 reduced in Ni^{2+}) for the Ni $2p_{3/2}$ multiplet is positioned at 855.3 eV which corresponds well with literature values for $Ni(OH)_2$.[208] The fitted components found in Figure 4.8d (MnO_2 reduced in Co^{2+}) for

the Co $2p_{3/2}$ multiplet (790.8, 786.1, 781.9, and 780.4 eV) match well with the calibrated (C1s = 284.8 eV) literature values found for $Co(OH)_2$ (790.5, 786.1, 782.3, and 780.5 eV).[209]

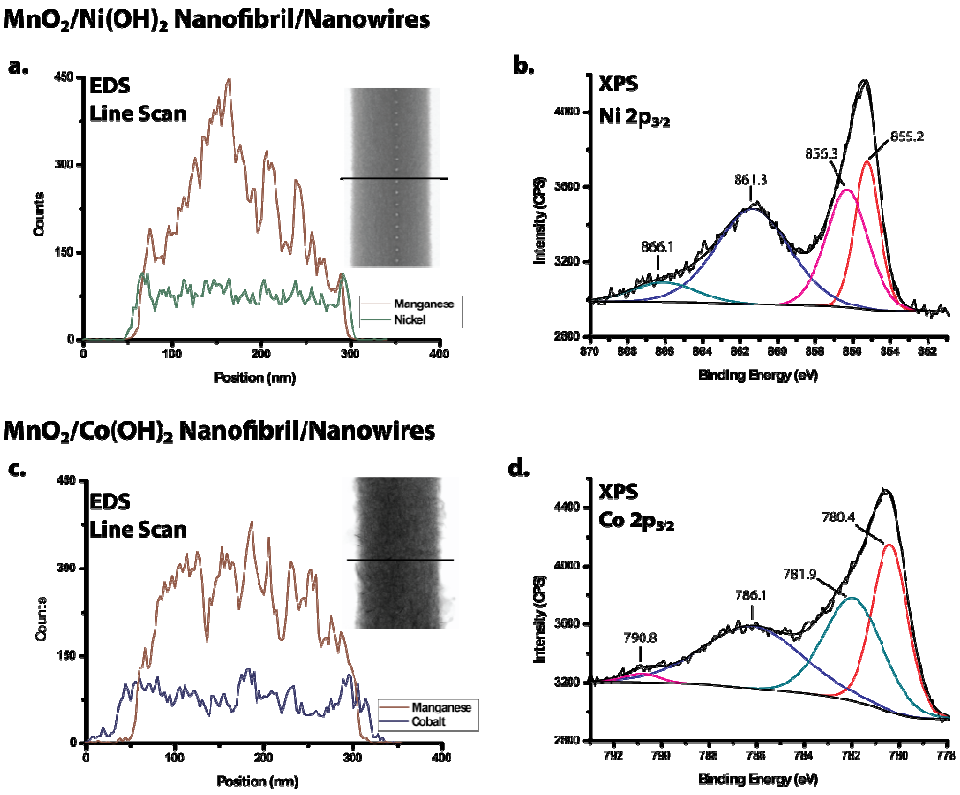

Figure 4.8 EDS and XPS of Heterogeneous $MnO_2/Ni(OH)_2$ and $MnO_2/Co(OH)_2$

Energy dispersive X-ray spectroscopy (EDS) line scans for MnO_2 nanowires reduced in a. Ni^{2+} and c. Co^{2+} and the XPS spectrum of the $2p_{3/2}$ multiplet for b. Ni and d. Co from these structures.

This formation of hydroxides from metal solutions during the reduction of MnO_2 correlates well with our assumption that the reduction of MnO_2 releases OH^- ions that

combine with the metal ions in solution. These metal hydroxides are then shown to precipitate out of solution as nanofibrils. This also demonstrates the ability of this method to be easily applied to other materials.

4.2.4 Supercapacitor application

4.2.4.1 Low Power Investigation of Charge Storage Mechanism

For investigation of the supercapacitor charge storage mechanism of this hierarchical structure, the nanomaterial was studied in the low power realm (scan rate: <10 mV/s). The material was tested in both an aqueous and organic (acetonitrile) solvent with lithium perchlorate as the inorganic salt. The voltage window was kept between 0 and 1 volt vs. Ag/AgCl for both electrolytes to directly compare the charge storage properties in the different solvents.

Figure 4.10 shows that the material in both solvents shows an increase in specific capacitance for the whole hierarchical material (Hier) upon addition of the nanofibrils when compared to the bare nanowire (Bare) counterparts (from 289 to 345 F/g for the aqueous solvent and from 324 to 387 F/g for the organic solvent) at a 0.5 mV/s scan rate. Note: All masses were attained from inductively coupled plasma-atomic emission spectroscopy (ICP-AES) elemental analysis (see Figure **4.9**).

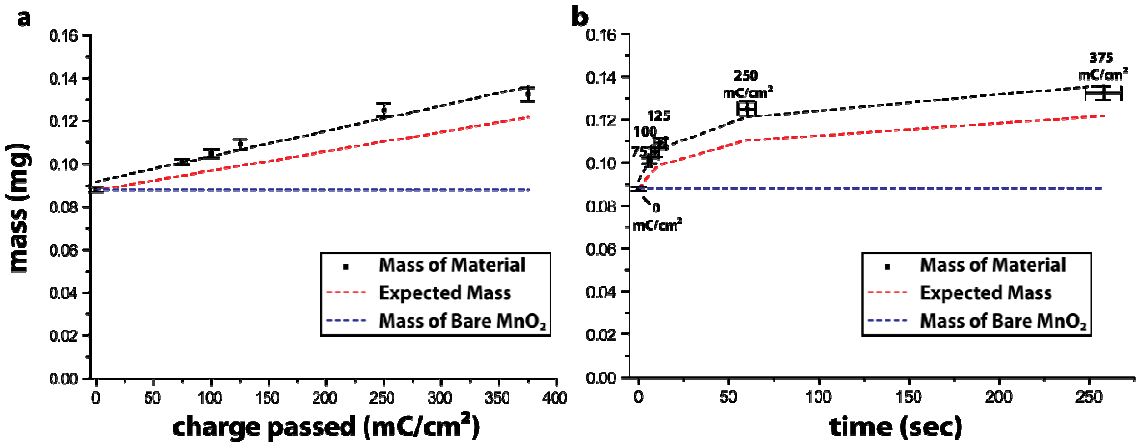

Figure 4.9. ICP-AES Data for the Deposition of MnO_2 Nanofibrils
(a) mass of total material measured from ICP-AES spectroscopy versus charge passed during the reduction of 200 nm 4.5 µm MnO_2 nanowires in Mn^{2+} solution; (b) mass of total material measured from ICP-AES spectroscopy versus time of deposition. (red curve represents expected mass based on reaction 1, while blue dashed line is the mass of the bare MnO_2 nanowire array)

The improvement in gravimetric capacitance may seem minor, but the improvement in areal capacitance is more dramatic. In aqueous electrolyte, the nanofibrils improve areal capacitance by 42.5% (from 128 to 181 mF/cm2). In organic electrolyte, the improvement is similar, with areal capacitances increasing 42.0%, from 143-203 mF/cm3. These total capacitance increases of 42.5% and 42.0% for the aqueous and organic solvent respectively are achieved with only a total mass increase of 19.3%. (Note: the planar area of the working electrode was maintained at 0.2 cm^2 for all materials)

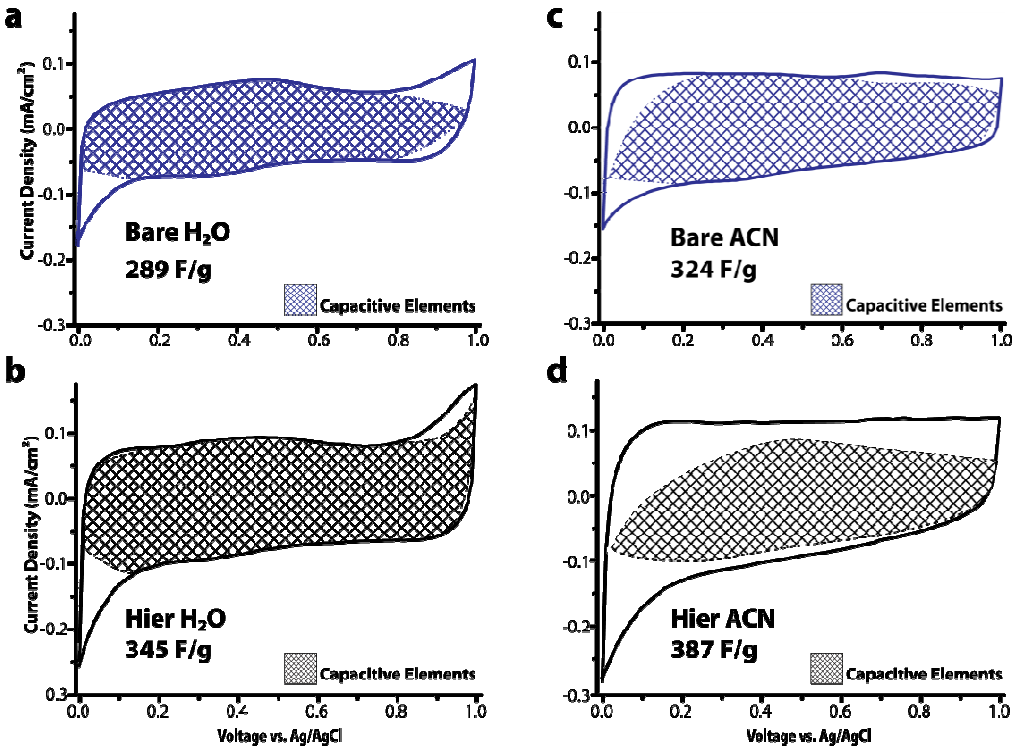

Figure 4.10 CVs of Bare and Hierarchical MnO_2

Cyclic voltammetry at a 0.5 mV/s scan rate with the hashed area representing the part of the curve that contains capacitive elements of a (a) bare MnO_2 nanowire array and (b) hierarchical MnO_2 nanowire cycled in an aqueous 1M $LiClO_4$ solution and a (c) bare MnO_2 nanowire array and (d) hierarchical MnO_2 nanowire cycled in an organic acetonitrile 1M $LiClO_4$ solution

Owing to this, we can obtain the specific capacitance associated with the nanofibrils if we divide the difference in total capacitance by the difference in the mass between the Hier and Bare arrays. The outcome of this calculation is a specific capacitance of 628 F/g and 718 F/g attributed to the nanofibrils for the aqueous and organic solvents respectively.

This large specific capacitance is thought to be due to both the ultrahigh surface area and small dimensions of the nanofibrils; however, due to the low mass loading of our material reliable BET measurements were not possible. The ultrahigh surface area can increase capacitive adsorption and double layer performance and the small dimensions can increase ion access points and shorten diffusion distances for any insertion processes. Although, these values are appealing, it is interesting to see how differently this extra charge is stored whether it be more by capacitive elements or insertion elements in each respective electrolyte.

Two different methods were used to investigate the charge storage mechanisms in the hierarchical structure. First, we use a method derived from Conway *et al* [210] by Dunn *et al* [211] and used recently by Penner *et al* [198] to quantitatively separate the contribution of the capacitive elements of the charge storage from the diffusion controlled insertion processes. By examining the scan rate dependence of the current, one can estimate that the current at each voltage is the sum of both contributions to the capacitance using the following formula:

$$i(V) = k_1 \upsilon + k_2 \upsilon^{1/2} \quad (1)$$

Where $i(V)$ is the current at a given voltage, k_1 and k_2 are constants and υ is the scan rate. In this equation, $k_1\upsilon$ represents the capacitive elements or elements where di/dυ is constant while $k_2\upsilon^{1/2}$ represents diffusion controlled bulk reactions where di/dυ$^{1/2}$ is constant. If we divide both sides of this equation with the square root of the scan rate; then we get the following equation:

$$i(V)/v^{1/2} = k_1 v^{1/2} + k_2 \quad (2)$$

Therefore, if we plot the $i/v^{1/2}$ at a given potential versus $v^{1/2}$, we should obtain a line with the slope equaling constant k_1 and the y-intercept equaling k_2 thus giving us a quantitative way of separating the capacitive elements, $k_1 v$, from the bulk reactions, $k_2 v^{1/2}$, at each given voltage.

If we look at Figure 4.10 again, we can see the results of using this method. Here, the hashed areas are attributed to a capacitive charge storage reaction. Figure 4.11, shows these results at different scan rates (0.5 and 10 mV/s) in terms of areal capacitance. These results indicate that the Hier material's increase in capacitance from the aqueous solvent comes mainly from an increase in capacitive charge storage (118.4 to 170.6 mF/cm^2 at the 0.5 mV/s scan rate) which is mainly due to the high surface area of the nanofibrils. However, the increase in capacitance from the organic solvent comes from an increase in cation insertion (7.0 to 66.7 mF/cm^2 at the 0.5 mV/s scan rate) which results from the short diffusion distance of the nanofibrils.

Another method developed by Trasatti to separate capacitive elements from insertion processes is used here.[212] Again a scan rate series is performed, but this time it is used to project what the capacitance will be at the scan rates of 0 and infinity. The capacitance at 0 mV/s will demonstrate the total capacitance (C_t) if we allowed sufficient for every reaction to take place, while the capacitance at an infinite scan rate will tell us only the charge stored at the surface (C_S). The difference between the total

capacitance and surface capacitance ($C_T - C_S$) will give us the capacitance associated with the insertion processes (C_I).

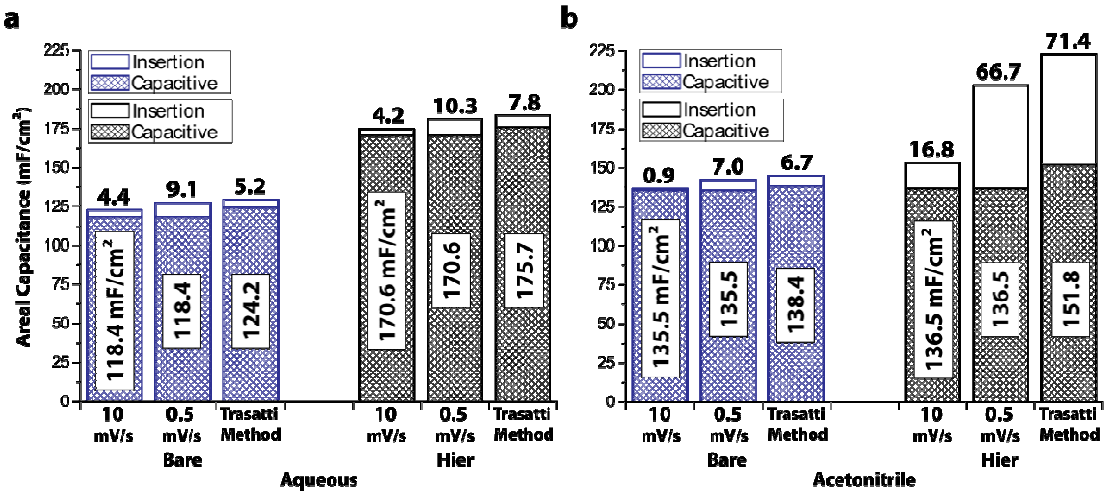

Figure 4.11 Comparing Trasatti's Method to Dunn's Method

Bar graph of bare (blue) and hierarchical (black) MnO_2 nanowire arrays' areal capacitance versus scan rate with the hashed areas representing the capacitance attributed to only capacitive elements derived from Dunn's method and the maximum capacitances derived from Trasatti's method in different solvents (a) aqueous and (b) acetonitrile

First, we obtain the maximum capacitance associated with the surface charges by plotting the capacitance, C, versus the inverse square root of the scan rate, $\upsilon^{-1/2}$, for both the bare and hierarchical structure as seen in Figure 4.12 (a and c) for the aqueous and organic solvents, respectively. (All the values used in Figure 4.12, and the slopes and intercepts obtained in Figure 4.12 can be found in the Table **4.1**) Here, we assume there is semi infinite linear diffusion, so we expect a linear correlation between C and $\upsilon^{-1/2}$.

However, both Figure 4.12 (a and c) deviate from linearity at high scan rates. This is caused by ohmic drops and irreversible redox transitions owing to the resistance of MnO_2.[213] Therefore, we fit the curve only at low scan rates (0.5 to 10 mV/s) where the points are close to linear. Using this curve, we can obtain $\upsilon^{-1/2} = 0$, which represents the maximum surface capacitance of the material. These results can be found in the hashed areas of the bar graphs labeled 'Trasatti Method' in Figure 4.11.

a. H_2O	Hier	Trassati	Bare	Trassati
Scan Rate	Capacitance		Capacitance	
0.5	180.9	**Figure 4.12a**	127.5	**Figure 4.12a**
1	180.7	**Slope (a)**	127.3	**Slope (a)**
2	180.8	4.5	127.5	2.9
5	178.7	**Intercept (b)**	127.1	**Intercept (b)**
10	174.8	175.7	122.8	124.2
20	172.7		120.7	
50	156.5	**Figure 4.12b**	107.8	**Figure 4.12b**
100	136.4	**Slope (a)**	91.2	**Slope (a)**
250	91.2	0.000079	61.3	0.000107
500	53.4	**Intercept (b)**	41.0	**Intercept (b)**
1000	23.8	0.00545	22.0	0.00773

b. ACN	Hier	Trassati	Bare	Trassati
Scan Rate	Capacitance		Capacitance	
0.5	203.2	**Figure 4.12c**	142.5	**Figure 4.12c**
1	193.3	**Slope (a)**	142.4	**Slope (a)**
2	186.8	40.0	142.4	3.6
5	176.3	**Intercept (b)**	142.4	**Intercept (b)**
10	153.1	151.8	136.4	138.4
20	133.4		133.9	
50	94.6	**Figure 4.12d**	116.9	**Figure 4.12d**
100	63.2	**Slope (a)**	97.3	**Slope (a)**
250	33.7	0.000615	62.4	0.000113
500	20.1	**Intercept (b)**	37.1	**Intercept (b)**
1000	9.3	0.00448	14.2	0.00689

Table 4.1. Values Used to Determine Trasatti Graphs

Capacitance values of the hierarchical and bare nanowire arrays in (a) water and (b) acetonitrile at different scan rates. The slopes and y-intercepts of the curves represented in Figure 4.12 for each material and solvent.

Furthermore, we plotted the inverse of the capacitance versus the square root of the scan rate. This can be observed in Figure 4.12 (b and d) for the aqueous and acetonitrile

solvent. Again we extrapolate the curve at low scan rates, this time to $\upsilon^{1/2} = 0$. Here we obtain the total maximum capacitance. These values can be seen in Figure 4.11 along with the results from the Dunn method for the scan rates of 0.5 and 10 mV/s. In comparison, both the Dunn method and Trasatti method show similar quantitative results with a better correlation between the methods at the smaller scan rates.

If we further utilize Trasatti's method to obtain the specific capacitance only attributed to the nanofibrils, then we can extrapolate the maximum specific capacitance of the nanofibrils at a 0 scan rate. Thusly, the specific capacitance of the nanofibrils at a given scan rate, SC_{nfs}, can be obtained using the following equation:

$$\square\square_{\square\square\square} = \frac{\left(\frac{\square}{\square_{\square\square\square\square}\square^{\square/\square} + \square_{\square\square\square\square}}\right) - \left(\frac{\square}{\square_{\square\square\square\square}\square^{\square/\square} + \square_{\square\square\square\square}}\right)}{\square_{\square\square\square\square} - \square_{\square\square\square\square}} * \square \qquad (3)$$

where *a* represents the slope and b represents the y-intercept of the fitted lines found in Figure 4.12 (b and d) for the aqueous and organic solvents, respectively. υ represents the scan rate, A represents the area of the electrode (0.2 cm^2), and mass represents the mass of the bare and hierarchical nanowire arrays.

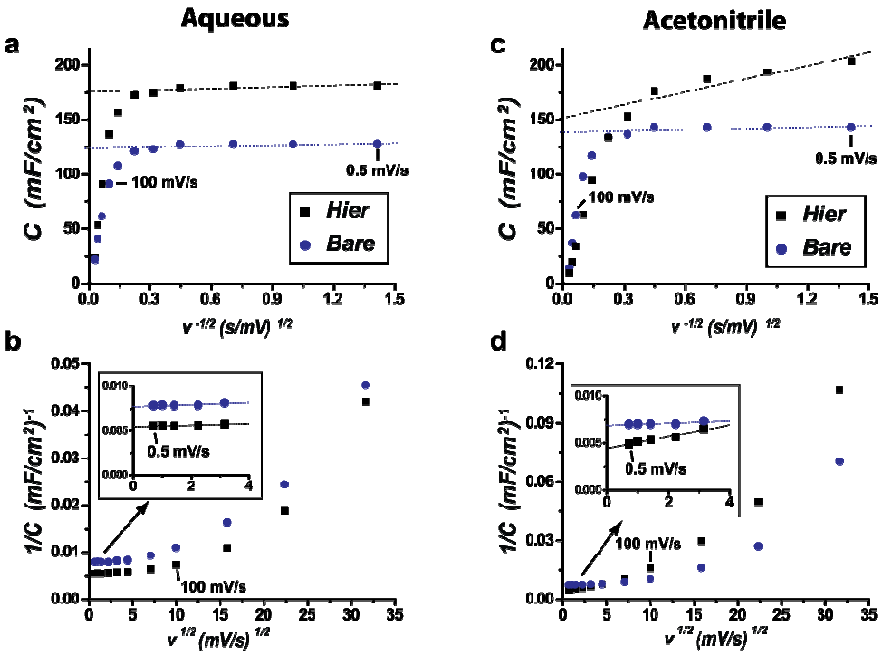

Figure 4.12 Trasatti's Method Data Curves

(a,c) Areal capacitance versus inverse square root of scan rate for bare (blue circles) and hierarchical (black squares) MnO_2 nanowire arrays cycled in (a) aqueous and (c) acetonitrile solvent electrolytes. (b,d) Inverse areal capacitance versus square root of scan rate for bare (blue circles) and hierarchical (black squares) MnO2 nanowire arrays cycled in (b) aqueous and (d) acetonitrile solvent electrolytes with the inset representing the linear aspect of these points at low scan rates

Figure 4.13 shows the raw data obtained from the scan rate series and the fitted data utilizing Trasatti's method for both the aqueous and organic solvents. The nanofibrils cycled in aqueous solution appear to have nearly reached their maximum capacitance of 637 F/g at a 0.5 mV/s scan rate, while the nanofibrils cycle in the acetonitrile solvent

appear to need exceedingly slow scan rates to come close to their maximum capacitance of 919 F/g.

This is a very interesting result as it shows that in the acetonitrile solvent, the MnO_2 nanofibrils can reach close to its theoretical maximum capacitance; however, in the aqueous solvent, these same MnO_2 nanofibrils reach a maximum capacitance far below their theoretical. This correlates well with our projection that the nanofibrils in aqueous solution only contribute fast surface capacitance thus they do not need exceedingly slow scan rates to reach their maximum specific capacitance. While in organic solution the nanofibrils utilize slow cation diffusion which does need very slow scan rates to fully make use of the material. Accordingly, one would expect that at a scan rate of zero, the material would exhibit the full theoretical capacitance of 1110 F/g based on one electron transfer; however, due to manganese oxide's low intrinsic conductivity, the data used to create Trasatti's curve in Figure 4.13 could be skewed to create a lower maximum specific capacitance.

Qualitatively, we can see that with the Trasatti method the nanofibrils have mainly a capacitive charge storage element in aqueous solution and mainly an insertion charge storage element in the organic electrolyte. This different charge storage mechanism in the different solvents is believed to be due to the proton adsorption behavior in water which mitigates the lithium insertion mechanism. In fact, in literature it has been shown that the cation does not play a major role in the charge storage mechanism in aqueous solutions.[34] Currently, we are investigating these different charge storage mechanisms using ICP-AES. However, it is interesting to note that regardless of the predominant

charge storage mechanism, the nanofibril structure produces an advantage for overall performance.

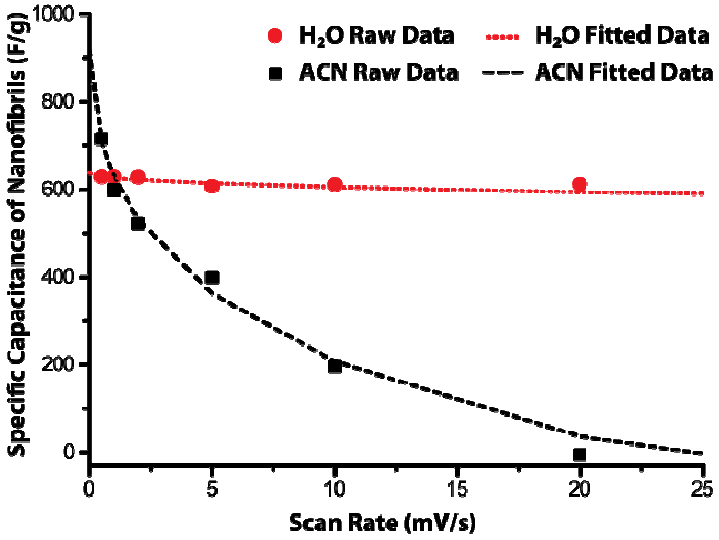

Figure 4.13 Specific Capacitance of MnO_2 Nanofibrils in Different Solvents

Specific capacitance attributed to the nanofibrils at various scan rates for the hierarchical MnO_2 material cycled in aqueous (red circles) and acetonitrile (black squares) solvents with the dashed lines representing the fitted curve based on Trasatti's method

4.2.5 High Power Investigation for Practical Applications

It was shown in the previous section that at low scan rates, the charge storage mechanism of the material can be obtained. However, for real supercapacitor applications, the material must show superior high power capabilities. For investigation of the practical supercapacitor properties of this hierarchical structure, the nanomaterial was studied at high power rates (>50 mV/s). For this high power testing,

the material was only tested in an aqueous solvent due to its intrinsically high ionic conductivity and low environmental impact.[58]

Figure 4.14a shows the cyclic voltammetry curves of the hierarchical material at high scan rates, 50, 100, and 250 mV/s. Although, the shape of the curve and the capacitance of the material (260 F/g) at 100 mV/s are promising for future applications, it is shown here that at the higher scan of 250 mV/s, the shape of the CV curve begins to have a sloping behavior and the capacitance drops dramatically.

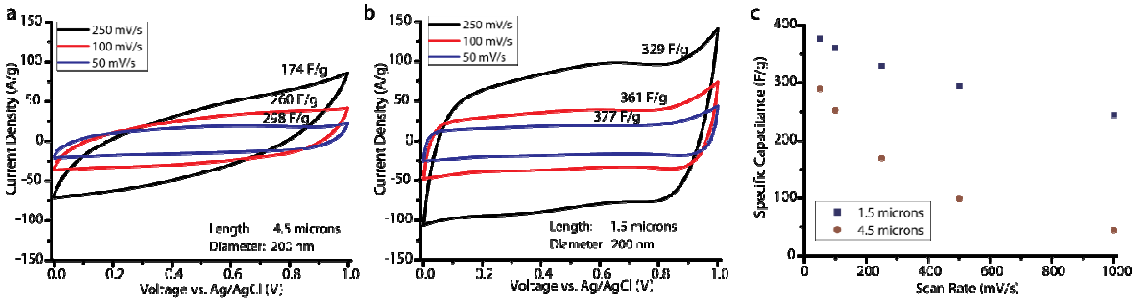

Figure 4.14 Comparison of Hierarchical MnO_2 with Different Lengths

Cyclic voltammetry curves in aqueous 1M $LiClO_4$ from 50-250 mV/s scan rates for the (a) 4.5 micron and (b) 1.5 micron in length hierarchical nanowire arrays and the power capability from 50-1000 mV/s scan rate for the 4.5 and 1.5 micron length hierarchical nanowires

Since, MnO_2 is known as a poor electron conductor, the 4.5 µm long nanowires (aspect ratio: 22.5) would seem to be exceedingly long. Therefore, shorter lengths of ≈ 1.5 µm of hierarchical nanowires (aspect ratio: 7.5) were produced by reducing the charge passed by a third during the synthesis of the nanowires. The synthesis of the

nanofibril layer was also cut by a third. Figure **4.14**b indicates that these shorter hierarchical nanowires are able to maintain their CV shape at the higher scan rates. The rate capability comparison of these nanowires is further shown in Figure **4.14**c.

Another benefit of the shorter nanowires is the increase in the specific capacitance (from 298 F/g to 377 F/g at 50 mV/s). However, it should be noted that although the gravimetric capacitance values increases with the shorter nanowires; the areal capacitance values decreases (from 156.5 mF/cm^2 to 66.0 mF/cm^2). Therefore, for future electrochemical energy storage, the benefits of higher gravimetric capacitance should be weighed against any loses in the areal capacitance.

Another aspect for this hierarchical material that can be varied is the amount of charge passed during the synthesis of the MnO_2 nanofibrils. Figure **4.15**a shows the specific capacitance vs. charge passed during the synthesis of the MnO_2 nanofibrils. The black squares in Figure **4.15**a represent the specific capacitance associated with the whole hierarchical structure, while the red squares represent the specific capacitance only associated with the MnO_2 nanofibrils. Figure **4.15** (b and c) shows the TEM images at different loading amounts for the MnO_2 nanofibrils with the upper left image in Figure **4.15**b representing a smooth bare MnO_2 nanowire and the bottom right image representing a fully nanofibril-coated nanowire.

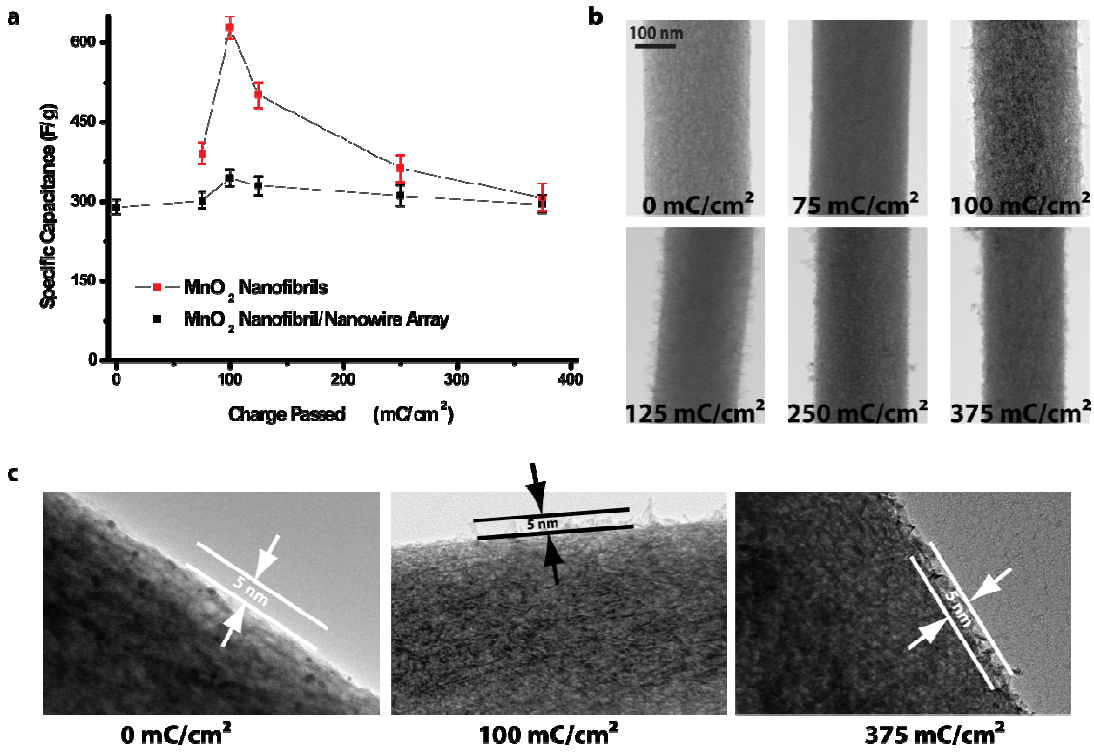

Figure 4.15 Hierarchical MnO_2 with Different Nanofibril Loading Amounts

(a) Specific capacitance (50 mV/s) of the whole hierarchical structure and that attributed to the nanofibrils during different nanofibril loading amounts controlled by the amount of charged passed during the synthesis of these nanofibrils and (b) the TEM images of these nanowires at the different stages along the graph in (a). (c) Magnified TEM images showing thickness of nanofibril layer as charge density is increased.

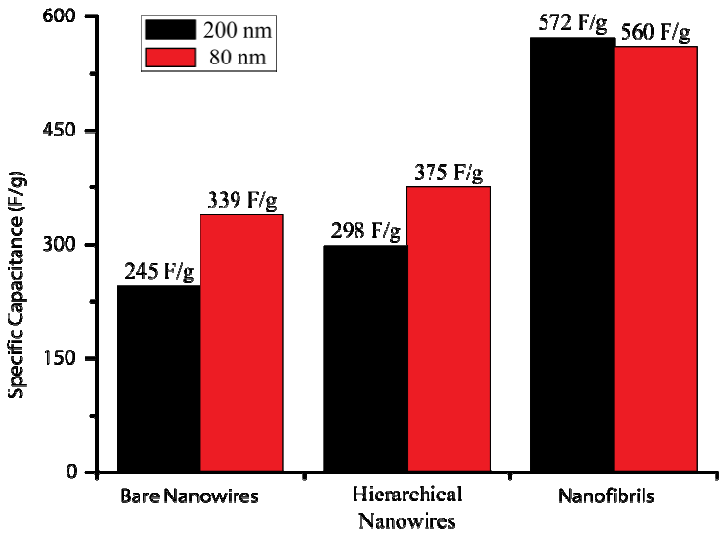

Figure 4.16 Comparing Hierarchical MnO_2 Nanowires with Different Diameters

Specific capacitance (50 mV/s) comparison between the 80 nm and 200 nm diameter nanowires showing the contribution from the individual architectures

As demonstrated in the graphs, the specific capacitance for both the hierarchical structure and the nanofibrils reaches a peak at a total charge passed of 100 mC/cm^2 for the hierarchical MnO_2 material. An explanation for this peak shaped plot is that at lower charge densities, the nanofibrils produced from the fast effusion of the hydroxide ions from equation 1a are too frail and are not in good electrical contact with the MnO_2 nanowires and so are electrochemically inactive. At higher charge densities, the nanofibril material is in good electrical contact; however, as the amount of charge passed increases the amount of coverage by the nanofibril layer ultimately reducing the access of the electrolyte to the nanowire. This reduces the specific capacitances associated with the MnO_2 nanofibrils to a number that is smaller than that associated with the pure MnO_2 nanowires.

Finally, the diameter of the nanowires was adjusted using AAO templates with 80 nm diameter pores during the synthesis process. As the charge storage mechanism is thought to be a near surface reaction, it is assumed that the smaller nanowires will reduce the amount of inactive MnO_2 resulting in larger specific capacitances. Figure 4.16 shows the comparison of the specific capacitance (50 mV/s) of the different diameter hierarchical nanowires. The results indicate that indeed the overall specific capacitance of the hierarchical nanowires increased when the diameter is decreased from 200 nm to 80 nm (298 F/g and 339 F/g, respectively); however, it is noted that the specific capacitance associated with the nanofibrils is not greatly affected (572 F/g for 200 nm and 560 F/g for 80 nm). This is attributed to the fact that the amount of nanofibrils produced is not affected by the diameter of the nanowires.

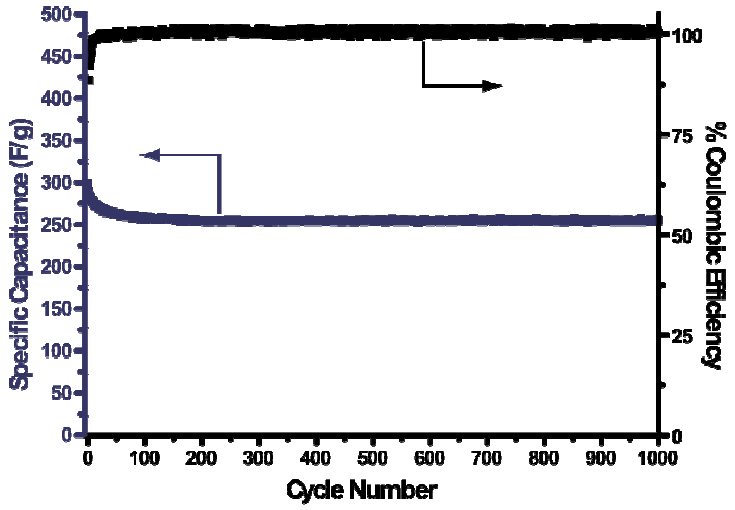

Figure 4.17 Cycle Ability of Hierarchical MnO_2

Cycle ability including specific capacitance (50 mV/s) and coulombic efficiency of the hierarchical structure over 1000 cycles in 1M $LiClO_4$ in water

Next, we show the cycle life of the hierarchical structure. Figure **4.17** shows the cycle ability of the 4.5 micron long 200 nm diameter hierarchical array over 1000 cycles at a 50 mV/s scan rate. The material maintains 85.2% (254 F/g) of its specific capacitance after 1000 cycles, which is still better than the initial bare specific capacitance at this scan rate (245 F/g). Most of this capacitance loss occurs within the first 100 cycles and correlates well with the coulombic efficiency during these initial cycles. It is thought that this may be due to some residual Mn_2O_3 to MnO_2 conversion associated with equation 3. After, the initial cycle degradation the material sees only a small drop in specific capacitance from 257 to 254 F/g for the remaining 900 cycles.

Finally, in order to compare our results with other hierarchical MnO_2 nanomaterials, we have included the tabulated information in table 1. This table shows that although our material may not have the highest capacitance, highest loading capability, or other superlatives; it does offer a controllable structure without the affects of binders and additives to gain scientific insight into the desired aspects of hierarchical MnO_2 nanomaterials.

Table 4.2. Literature Survey of Hierarchical MnO_2 Supercapacitors

Description	Specific Capacitance at Low and High Power	Cycle Retention Rate	Mass Loading	Synthesis Method	Binder and Additives	Control of Structure
Hollow Urchin-like MnO_2 Nanospheres[102]	167 F/g (2.5 mA) 124 F/g (10 mA)	89% after 350 cycles	≈10 mg (calc)	Hydrothermal	Yes	Some Morphological Control
Hollow MnO_2 Nanospheres[214]	299 F/g (5 mV/s) No High Power Testing Shown	97.6% after 1000 Cycles	≈7 mg (calc)	SiO_2 Nanosphere as sacrificial template	Yes	None Shown
3D Porous birnessite-MnO_2[215]	194 F/g (0.1 A/g)	95% after 1000 Cycles	≈11 mg (calc)	Hydrothermal using thermally reduced graphene oxide as template	Yes	None Shown
MnO_2 coated on Mn_3O_4 Decorated MnOOH Nanorods[216]	470 F/g (25 mV/s) 360 F/g (500 mV/s)	95.7 % after 10000 cycles	≈50 µg/cm^2 (calc)	Pulsed Electrochemical Deposition	No	None Shown
MnO_2 Nanorods Assembled into Spheres[217]	356 F/g (2 A/g) 184 F/g (10 A/g)	"No Degradation" after 2000 Cycles	≈0.5 mg (calc)	Precipitation Reaction of Mn^{2+} with Mn^{4+} in presence of P123 Micelles	Yes	None Shown
Assembled MnO_2 Nanowire Flowers[218]	407 F/g (10 mV/s) 258 F/g (100 mV/s)	>90% after 400 Cycles (Dependent on charge rate)	≈1 mg (calc)	Microwave Heating of acidified MnO_4^- solution	Yes	Random versus assembled MnO_2 nanowires
Urchin-like MnO_2 Nanospheres[96]	120 F/g (5 mV/s) 80 F/g (200 mV/s)	Not Shown	0.2 mg/cm^2	Hydrothermal	Yes	Urchin-like to Clew-like Morphology Control
MnO_2 nanowires coated with MnO_2 Nanofibrils (This research)	**1.5 µm Long Nanowires** 377 F/g (50 mV/s) 244 F/g (1000 mV/s)	89.6% after 1000 Cycles (91.2% after first 100 cycles)	0.035 mg	Two Step Electrochemical Deposition	No	Can Control Length and Diameter of nanowires, and Amount of nanofibrils
	4.5 µm Long Nanowires 298 F/g (50 mV/s) 44 F/g (1000 mV/s)	85.2% after 1000 Cycles (86.6% after first 100 cycles)	0.105 mg			

4.2.6 Heterogeneous $Ni(OH)_2/MnO_2$ nanofibril/nanowire Arrays

Finally, in order to further study this mechanism and to show the versatility of this method, we have applied it to another system. Here, MnO_2 nanowire arrays are reduced by the same method, but this time in Ni^{2+}. Again, a hierarchical nanowire array is produced, this time with $Ni(OH)_2$ nanofibrils. Figure 4.8a shows the energy dispersive X-ray spectroscopy (EDS) line scan for this hierarchical heterogeneous structure. The graph illustrates a MnO_2 nanowire core with an oxide of nickel shell.

The phase of this nanofibril shell was shown to be $Ni(OH)_2$ by utilizing X-ray photoelectron spectroscopy (XPS) (Figure 4.8b). This formation of hydroxides from metal solutions during the reduction of MnO_2 correlates well with our assumption that the reduction of MnO_2 releases OH^- ions that combines with the metal ions in solution. These metal hydroxides are then shown to precipitate out of solution as nanofibrils. This also demonstrates the ability of this method to be easily applied to other systems.

This material was also probed for its supercapacitor performance and compared to its bare MnO_2 nanowire counterpart. Please note that the electrolyte, reference electrode, and potential window used for this hierarchical $Ni(OH)_2/MnO_2$ structure (4M KOH, Hg/HgO, and 0.1-0.6 V) are different than those used for the hierarchical MnO_2 structure (1M $LiClO_4$, Ag/AgCl, and 0-1 V). It should also be noted that the heterogeneous $Ni(OH)_2/MnO_2$ structure is not proposed here as a future material for supercapacitors due to MnO_2's deficient cycle ability in high pH KOH solutions. This is shown in Figure **4.18** where the cycle ability of the hierarchical MnO_2 array is compared to that of the heterogeneous $Ni(OH)_2/MnO_2$ nanofibril/nanowire array. Even so, this material is shown here to support the benefits of these hierarchical structures.

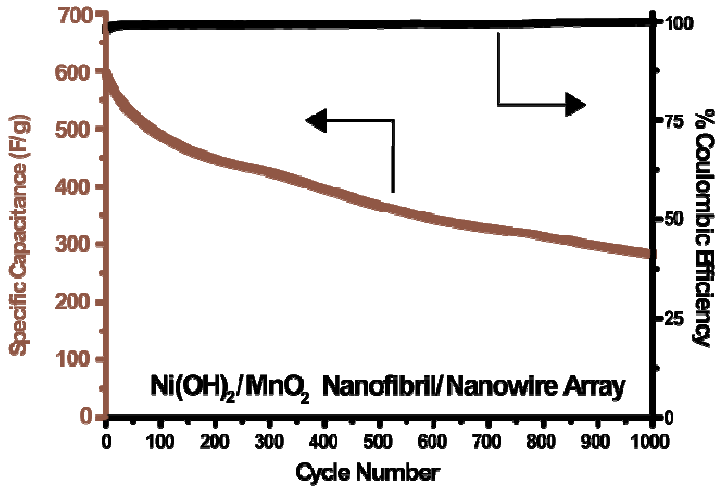

Figure 4.18. Cycle Ability of $Ni(OH)_2/MnO_2$ Nanofibril/Nanowire Array

In the CV in Figure **4.19**, a redox peak shaped curve appears for the heterogeneous $Ni(OH)_2/MnO_2$ material after reduction in Ni^{2+}. This peak is associated with the Ni(OH)/NiO redox couple.[173] Due to this peak, the heterogeneous structure shows an increase, when compared to the bare MnO_2 array, in the area encapsulated by the CV curve which represents an increase in energy for this material.

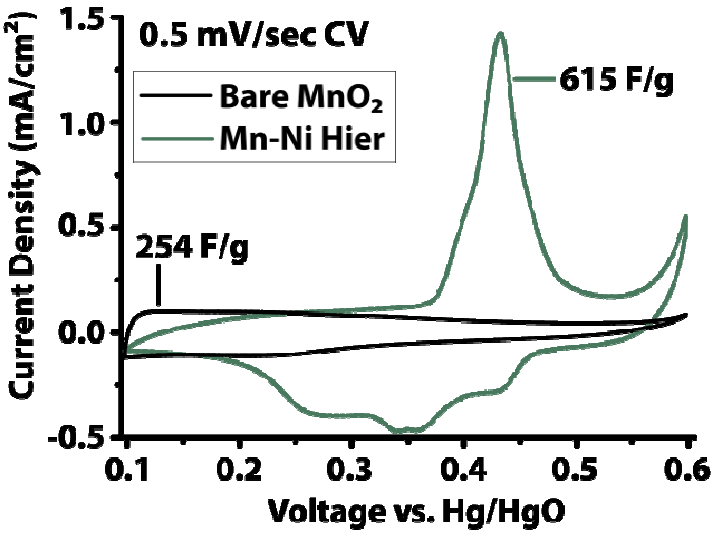

Figure 4.19. CV of Hierarchical $MnO_2/Ni(OH)_2$ Array

Cyclic voltammetry scans of bare MnO_2 (black) and hierarchical MnO_2-$Ni(OH)_2$ (green) nanowire arrays cycled in 4M KOH

The specific capacitance of the heterogeneous $Ni(OH)_2/MnO_2$ structure is 615 F/g which is significantly better than that of the bare MnO_2 nanowires (254 F/g). The specific capacitance associated with just the $Ni(OH)_2$ nanofibers is calculated as 1505 F/g which approaches the theoretical maximum of 2081 F/g for $Ni(OH)_2$. These high specific capacitances are associated with the high surface area and good electrical contact of the $Ni(OH)_2$ nanofibrils. However, since MnO_2 is a poor conductor, these results have a lot of room for improvement. These results indicate that the method of synthesis here can be applied to other systems.

4.3 Conclusion

A controllable hierarchical MnO_2 nanofibril/nanowire array was successfully synthesized. The structure consists of a conformal layer of MnO_2 nanofibrils evenly

distributed on the surface of the MnO_2 nanowires. The synthesis of the MnO_2 nanofibril layer was done by a simple electrochemical conversion of the MnO_2 nanowires to Mn_2O_3 in a Mn^{2+} solution. Due to the hydroxide formation during this conversion, a $Mn(OH)_2$ nanofibril layer was formed at the surface of these nanowires which quickly oxidized to Mn_2O_3. Subsequently, oxidation of both the Mn_2O_3 nanowires and Mn_2O_3 nanofibrils resulted in the formation of the hierarchical MnO_2 nanofibril/nanowire material. This structure was characterized by Raman, EELS, ICP-AES, electrochemical measurements, and electron microscopy.

At slow scan rates, this hierarchical nanowire structure showed an enhanced supercapacitor performance when compared to its bare nanowire counterpart in both aqueous and acetonitrile solvents. However, this enhancement is shown to a result of different mechanisms depending on the solvent. In aqueous solvent, the nanofibril structure increases its capacitance by capacitive processes, while in an acetonitrile solvent, the nanofibril structure increases its capacitance by insertion processes. These results indicate that the solvent has a major effect on whether this material can reach its theoretical capacitance.

At fast scan rates, this hierarchical material showed a good capacitance of 298 F/g at 50 mV/s. The capacitance and power capability was shown to be further improved at the detriment of areal capacitance to 329 F/g at 250 mV/s when the length of the nanowire was shortened from 4.5 µm to 1.5 µm. The overall hierarchical capacitance was also shown to be improved by smaller diameter nanowires (298 F/g to 375 F/g at 50 mV/s); however, the capacitance attributed to the nanofibrils remains close to the same (572 F/g to 560 F/g) regardless of nanowire diameter. The loading amount of

nanofibrils is also shown to have a dynamic affect on the material's specific capacitance with an increase occurring initially due to the high nanofibril surface area followed by a decrease occurring due to the blockage of electrolyte by the increasingly dense nanofibril layer.

This facile synthesis method was successfully applied to other divalent metal solutions (Ni^{2+} and Co^{2+}) resulting in $Ni(OH)_2$ and $Co(OH)_2$ nanofibrils, respectively, conformally coating the MnO_2 nanowires. The $Ni(OH)_2/MnO_2$ material shows an increase in overall specific capacitance resulting from a large initial specific capacitance of 1505 F/g for the formed $Ni(OH)_2$ nanofibril layer. We hope to analyze these materials in depth as previous literatures have shown great supercapacitor properties with these types of hierarchical/heterogeneous materials.[219, 220] Other hierarchical nanostructures are thought to be possible including but not limited to MnO_2/RuO_2, MnO_2/Fe_3O_4, and MnO_2/Al_2O_3 materials from using Ru^{3+}, Fe^{2+}, or Al^{3+} solutions, respectively. This method of formation is versatile enough that it may well be used in the many different applications where MnO_2 is already or proposed to be employed.

Chapter 5: Charge-Storage Mechanism Investigation of MnO_2 using ICP-AES

As indicated above, MnO_2 appears to have a different fundamental charge storage mechanism in different solvents. In order for MnO_2 to be used to its full potential, we must understand this mechanism. In other words, what combination of chemistries including specific surface area, crystal structure, electronic conductivity, adsorbed water molecules, ionic conductivity, material morphology, and electrolyte cation will give us the best performance for MnO_2? This chapter is focused on giving some answers to this fundamental question.

In organic electrolyte, the mechanism is thought to directly involve the insertion of the cation into the bulk of the electrode material;[221] although, to our knowledge, this mechanism has not been thoroughly investigated in the literature.

On the other hand, the aqueous charge storage mechanism has been investigated in detail, using analytical methods such as XPS,[34] Raman,[222] XRD,[223, 224] X-ray absorption near-edge structure spectroscopy (XANES),[225] and electrochemical quartz-crystal microbalance (EQCM),[224] in addition to other electrochemical observations utilizing different electrolyte salts[35, 226] and calculations made observing the scan rate dependence of the material as our group did on page 113 of this work and others have done in the literature.[198]

So far, the proposed charge storage mechanism of MnO_2 in aqueous solvent can be represented by the following equation with the typically referenced potentials below:

$$MnO_2 + aH^+ + bC^+ + (a+b)e^- \leftrightarrow MnOOH_aC_b$$

$$1\ V\ vs.\ Ag/AgCl \leftrightarrow 0\ V\ vs.\ Ag/AgCl$$

where Mn^{4+} becomes Mn^{3+} upon reduction to 0 V vs. Ag/AgCl with either an adsorbed or inserted cation, C^+, or H^+ acting as the counter ion from the electrolyte.

Certainly, the results of the XPS, Raman, XRD, and XANES experiments indicate that MnO_2's oxidation state as well as crystal structure does change during charging; however, the issue comes about when trying to determine what is counter ion involved with these changes. Electrochemical observations do suggest that the cation plays a role; however, how much of a role and does it insert or only adsorb on the surface have yet to be answered unequivocally.

Attempts to answer this fundamental question have been done by Kuo *et al.* who did some EQCM experiments utilizing different electrolyte cations in aqueous solution and observed mass changes that they associated with the uptake of a combination of H_3O^+ ions and cations during charging.[224] They determined that the amount of cation participation in the charge storage was dependent on the cation with alkali ions participating more and then less in the charge storage mechanism with increasing ionic size. However, they were not able to directly determine the molar ratio of the cation to MnO_2 unit during charging. In addition, the cycle window that was chosen between 0.5 and 0.8 V vs. Ag/AgCl may not be characteristic of the normal cycle window for MnO_2 of between 0.0 and 1.0 V vs. Ag/AgCl as they mention that previous studies using EQCM to determine the charge storage mechanism of RuO_2 showed different mechanisms in different voltage regions.[227]

In another experiment, Guan et al. systematically ruled out the proton as a source of the charge storage mechanism by analyzing different alkali cations in different pH solvents while monitoring MnO_2's capacitance.[228] They observed no change in capacitance as the pH was adjusted from 7 to 4 and even a decrease in capacitance when the pH was set at 3. This would indicate that the proton has a detrimental effect at high H^+ concentrations which is the inverse of what would be thought if the proton was the major charge storage species.

However, Mho *et al.* performed another experiment where they monitored the capacitance of MnO_2 as they adjusted the concentration of a KCl electrolyte.[229] Although, they saw a decrease in the capacitance upon decreasing the K^+ ion concentration, they also were able to increase the capacitance of dilute K^+ by decreasing its pH to 3. Again, indicating that the proton does play a role in the charge storage.

Owing to these experiments, there needs to be a systematic way of analyzing MnO_2's charge storage mechanism that takes into account electrochemical measurements; elemental analysis; detailed solvent, material, and electrolyte properties; as well as voltage window analysis and even electrolyte and material computer modeling. Although, this is the ultimate goal of this research, this chapter will only show our initial experiments using inductively coupled plasma – atomic emission spectroscopy (ICP-AES) for elemental analysis and some electrochemical results obtained so far.

ICP-AES is used here due its low detection limit, high selectivity, and precise measurement capability of the total cation and manganese ion content. This method has yet to be explored partly due to the complex makeup of energy storage electrodes that

involve polymeric binders and conductive additives that inhibit electrode digestion, which can detrimentally affecting the analysis.

AAO template grown MnO_2 nanowire arrays are utilized for this analysis, due their controllable features such as their length and diameter which will give us a better ability to probe surface to bulk ratios that may affect the charge storage mechanism. These nanowires are electrochemically grown directly on the current collector, assuring almost 100% electrochemical activity for all of the MnO_2 material.

Both organic (acetonitrile) and aqueous phase solvents are used here in order to examine the proton contribution by eliminating its presence entirely by using a aprotic organic solvent and also to compare and contrast MnO_2's potential window in each solvent as it has been suggested that MnO_2's supercapacitive behavior can have a larger window in organic electrolytes.

Initial results indicate that the proton does indeed play a large role in the charge storage mechanism of MnO_2 in aqueous solvents; however, only cations are shown to play a role in organic acetonitrile solvents. In addition, enlarging the potential window in acetonitrile has shown a capability of increasing the cation to Mn ratio to greater than 1.5, indicating a possible larger charge storage capacity for MnO_2 than previously thought.

5.1 ICP-AES as an Electrode Analysis Method

In order to do the quantitative elemental analysis of MnO_2 during the charging and discharging process, an analytical method had to be found that has high sensitivity, high selectivity, and a capability to detect alkali (including lithium) and alkaline earth metals.

Inductively coupled plasma – atomic emission spectroscopy (ICP-AES) instrumentation was found to be perfect for this work.

ICP-AES has sensitivities for most metallic elements in the parts per billion (ppb) range ($\mu g\ L^{-1}$). It is highly selective and can simultaneous determine cation and manganese ion concentrations. All naturally occurring alkali and alkaline earth metals can be detected and quantified using this method. This method has yet to be explored partly due to the complex makeup of energy storage electrodes that involve polymeric binders and conductive additives that inhibit electrode digestion, which can detrimentally affecting the analysis.

In a typical ICP-AES analysis, a solution of ions is pumped through a glass nebulizer, where a fine mist of the solution is produced. A small portion of this mist is then carried into an argon plasma created by a radiofrequency (RF) coil where the ions are desolvated and excited by the bombardment of electrons from the plasma. The ions then relax to the ground state releasing photons with a wavelengths directly related to their atomic makeup. These photons are then directed to a charge-coupled device (CCD) camera where their intensity is measured.

Due to this process, all materials must be dissolved in solution before any analysis can be done. In our case, this means that each sample must be destroyed in order to take a measurement using this instrument. Therefore all measurements done here are considered *ex situ*.

5.2 Experimental

5.2.1 Synthesis of freestanding MnO_2 nanowire array

First, a Denton Desk III sputter machine is used to sputter a ≈300 nm gold layer on the branched side of an AAO membrane. A strip of copper tape, to provide good electrical contact, is then attached to the gold side of the membrane. This piece is then sandwiched between layers of Parafilm with part of the non-sputtered side exposed with a defined window of 0.2 cm^2 resulting in completion of the working electrode.

The working electrode is then placed in a 100 mM manganese acetate bath with a Ag/AgCl reference and a platinum counter electrode. A constant voltage of 0.60 V vs. Ag/AgCl is applied until 150 mC of charge was charge passed.. A soaking time of 15 minutes in a 3 M solution of sodium hydroxide resulted in the complete dissolution of the alumina membrane producing vertically aligned MnO_2 nanowires attached to a gold current collector.

5.2.2 Electrochemical Analysis

After removal of AAO, MnO_2 nanowire arrays are soaked in DI water twice for five minutes in order to remove any residual hydroxide. The arrays are then place in the solvent that they will be tested in and soaked again for five minutes. Finally, the arrays are placed in their test solution.

The arrays are then galvanostatically scanned from 0 to 1 V vs. Ag/AgCl at a 1 A/g current density and stopped at specific voltages. For the holding potential test, a specified voltage vs. Ag/AgCl is applied for 15 minutes.

After testing, the arrays are soaked in the pure solvent that they were tested in three times for five minutes each. This is done in order to avoid any contamination from the high concentration lithium salt in the testing solution. After soaking, the electrodes are ready to be dissolved and administered to the ICP-AES instrument.

5.2.3 Inductively coupled plasma-Atomic emission spectroscopy (ICP-AES)

ICP-AES measurements were performed using a PerkinElmer ICP-Optima 4300. Intensities were measured at 257.610 nm for Mn and 670.784 nm for Li. Calibration curves were made from Mn and Li standards traceable to the National Institute of Standards and Technology (NIST).

All electrodes were dissolved in 3:1 concentrated HCl:HNO_3 and diluted to a known volume before being administered to the plasma; however, before this dissolution, electrodes were removed from their respective electrolytes and successively soaked in DI water twice for five minutes in order to eliminate any cation contribution that could come from any residual electrolyte.

5.3 Results and Discussion

MnO_2 nanowire arrays are galvanostatically cycled at 1 A/g between 0 and 1 volt vs. Ag/AgCl and then stopped at specific voltages during their discharge. The electrodes are then dissolved and analyzed for their lithium and manganese content by ICP-AES. The results for samples cycled in water and acetonitrile are found in Figure 5.1. The black squares indicate the suspected Li:Mn ratio based on the amount of charge

accumulated during the discharge, while the colored circles are the Li:Mn fractions measured from ICP-AES.

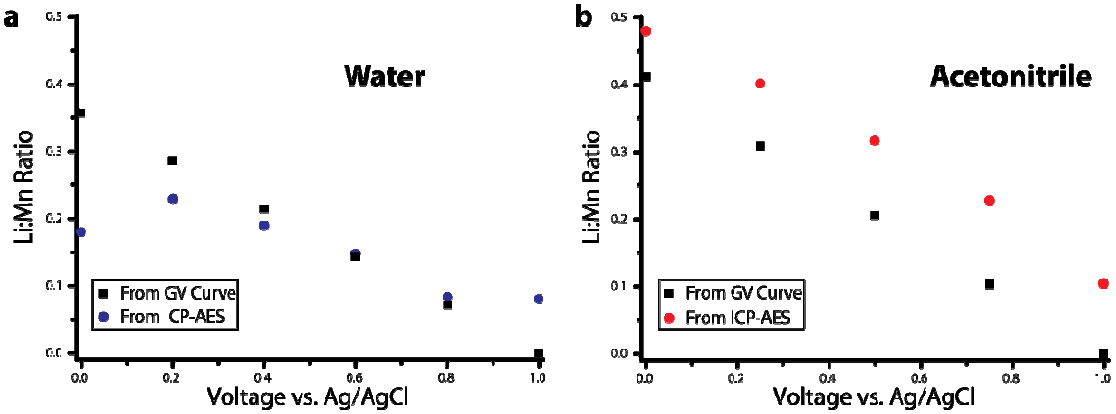

Figure 5.1. ICP-AES vs. GV Results in Water and Acetonitrile

MnO_2 nanowires scanned from 0 to 1 V in 0.1 M $LiClO_4$ in (a) water and (b) acetonitrile with the calculated Li:Mn ratio from the GV curve and ICP-AES results

The data from the GV and ICP-AES for the water system do not match very well. Instead of linear increase in lithium ratio as expected from the GV curve, the ICP-AES indicates a small increase with a leveling off at potentials below 0.4 V. This perhaps indicates that the lithium ion only plays a role at the higher potentials in aqueous solution.

As for the acetonitrile graph, the slopes of the GV and ICP-AES curves match nicely, albeit off set by ≈0.1 Li:Mn. However, this offset may be a an error from the GV calculation, as it assumes complete lithium removal from the material at 1.0 V vs. Ag/AgCl, which may not be the case at the high GV current density of 1 A/g.

This high current density may not be ideal for this type of research as the electrodes are only scanned to these potentials and not allowed to equilibrate; therefore, the following research was done by holding the potential at a given voltage for 15 minutes.

In this case, MnO_2 nanowire arrays were held at potentials of 0 and 1 V vs. Ag/AgCl in 0.1 M $LiClO_4$ in water and acetonitrile solvents. The voltages were chosen due to the traditional voltage window used for MnO_2 as a supercapacitor material where 1 V represents the charged state and 0 V represents the discharged state. The material was held at extended times, 15 minutes, in order to obtain equilibrium with the electrolyte. The samples were then dissolved and analyzed by ICP-AES. The results of these samples in terms of the Li:Mn ratio versus voltage applied are presented in Figure **5.2** along with results from electrodes soaked in the electrolytes for the 15 minutes plotted according to their open circuit potential (OCP).

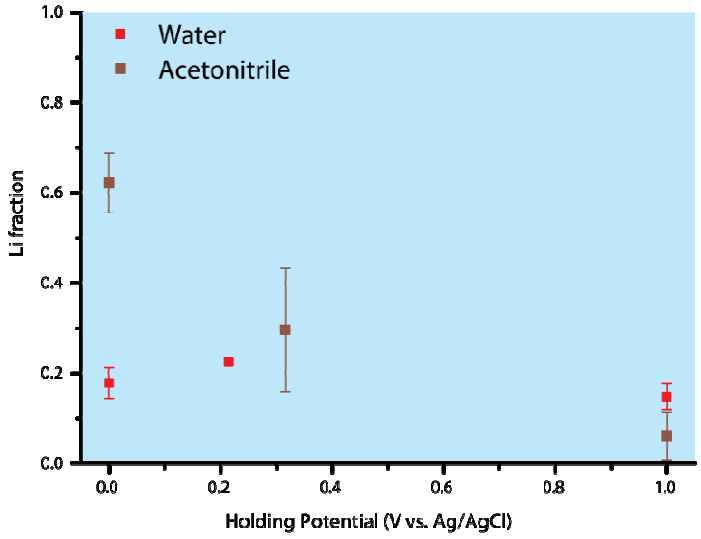

Figure 5.2. Li:Mn Ratio of MnO_2 Held at Different Potentials in Different Solvents

As can be observed, at 1 V there is little Li presence (<0.2 Li:Mn) in the electrode in both solvents as expected as MnO_2 is in the oxidized state. However, at 0V the Li:Mn ratio is expected to rise to 1:1 if the cation is the only active ion in the solvent; however, for the aqueous solvent there is no perceivable change in the Li amount and for the organic solvent the Li:Mn ratio only achieves a little more than 0.6 lithium ions per manganese ion. This indicates a greater dependence on the cation for charge transfer in the organic electrolyte when compared to the aqueous electrolyte.

As the Li:Mn ratio is still somewhat short of the 1.0 Li:Mn ratio expected for the aprotic acetonitrile solution, we investigated the possibility that the traditional stopping point of 0.0 V vs. Ag/AgCl is not in fact the real thermodynamic minimum for lithium insertion in the organic electrolyte. The results of this is shown in Figure **5.3**a where the Li fraction approaches a value of 1.5 at a voltage of -0.5 V vs. Ag/AgCl and maintains this ratio even as the holding potential applied is further augmented to -1.0 V. This increase and then leveling off of the Li fraction at potentials beyond -0.5 V is interesting as it is normally assumed that there is no insertion or adsorption of cations at potentials less than 0.0 V. Also, the magnitude of this fraction was thought to reach a maximum of 1.0 while this result indicates that a value of 1.5 may be possible.

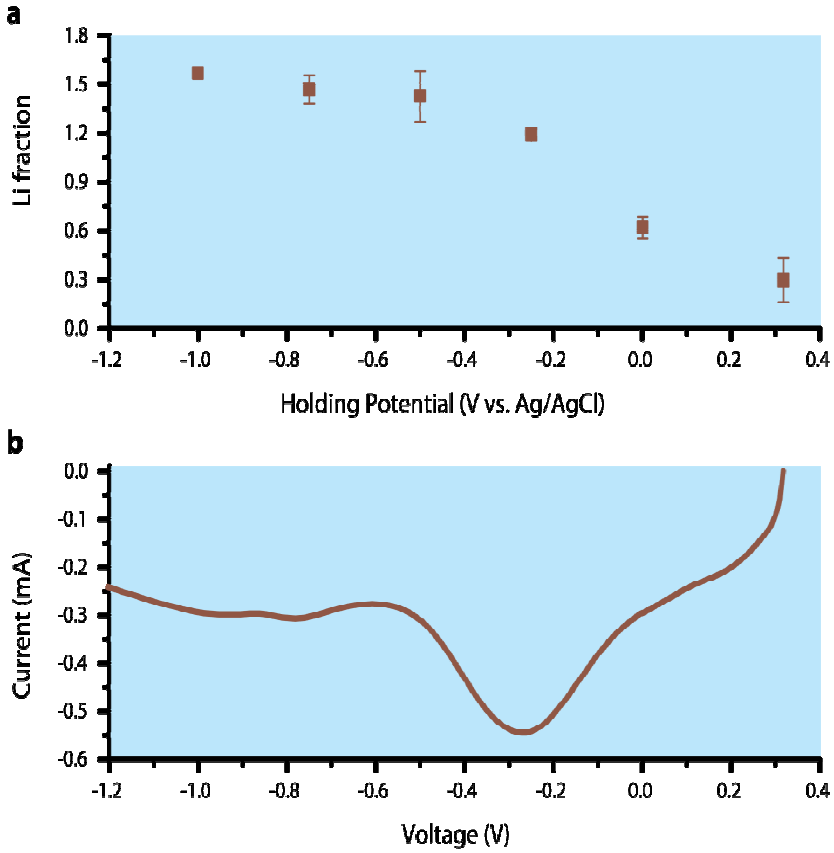

Figure 5.3. Li:Mn Ratio and Linear Sweep Voltammetry at Negative Potentials

(a) Lithium fraction vs. holding potential for MnO_2 nanowires in acetonitrile at potentials beyond traditional stable cycle windows for MnO_2 and (b) linear sweep voltammetry of MnO_2 from OCP to -1.2 in a 0.1M $LiClO_4$ acetonitrile electrolyte

We investigated this result by looking at the linear sweep voltammetry of MnO_2 in acetonitrile which can be seen in Figure **5.3**b. This sweep from OCP to -1.2 V vs. Ag/AgCl indicates that there is a reductive peak centered at -0.28 V. The position of this peak corresponds well with the Li fraction results, whereas holding potentials approaching this peak had Li fractions that were increasing and results beyond this peak contained constant Li ion fractions. This indicates that this peak is directly related to

lithium ion adsorption or insertion and therefore MnO_2 supercapacitor voltage windows that do include this peak cannot obtain theoretical maximum.

5.4 Conclusion

Although not completed, the initial results of this study suggest that protons do indeed play a role in the charge storage mechanism of MnO_2 in aqueous solutions. However, in organic solutions, only cations play a role. It is also observed that a potential increase in the theoretical capacitance may be needed as MnO_2 is shown here to have cation to Mn ratios greater than 1.5; even though, only ratios of 1.0 have been thought possible.

Additional experiments need to be done to support these conclusions. It is suggested that valence state measurements of bulk MnO_2 need to be done alongside the ICP-AES experiments in order to show that there is no self-discharge reaction happening during the electrode rinse step. Different cations, including divalent ions, will need to be tested in order to further probe the cations role in this charge storage. Additional studies on the nanowire morphology and crystal structure may be needed in order to observe how surface area and electronic structure play a role. Finally, electrolyte and material modeling may be needed in order to develop an encompassing theory that can be experimentally tested.

Chapter 6: Summary and Outlook

This thesis introduced the importance of MnO_2 nanostructures for supercapacitors and demonstrated three ways in which we are trying to question the role of MnO_2 in future electronic energy storage devices. These include:

1. MnO_2 nanomaterials in flexible devices: where in Chapter 3: we investigated and attempted to improve the use of coaxial MnO_2/PEDOT nanowires as a cathode for flexible supercapacitor devices.
2. Hierarchical MnO_2 Nanowires: where in Chapter 4: we developed a new facile method for creating hierarchical MnO_2 nanofibril/nanowire arrays and investigated their charge storage mechanism in organic and aqueous solvents.
3. MnO_2 charge storage mechanism: where in Chapter 5: we used ICP-AES to further investigate MnO_2's charge storage mechanism in both aqueous and organic solvents and found novel results that could transform how we determine the maximum theoretical specific capacitance of MnO_2.

We in no way claim that any of these projects are complete as each can be improved; however, we offer our results so far to the scientific community and hope that they can be built upon. These results include:

From Chapter 3:

I. Freestanding heterogeneous MnO_2 nanowires have considerable promise to be used in future flexible power sources as these nanowires are grown directly on

the current collector with no need for additives or binders which allows each nanowire to independently move during any flexing or bending.

II. The asymmetric supercapacitor configuration can not only improve energy density when compared to the symmetric configuration, but also the rate capability and cycle life. This improvement can be explained by a close examination of the voltage windows for the anode and cathode in the device configuration, which reveals a deviation from the voltage window generally assumed during half-cell testing.

III. Nanomaterials made using the AAO template method can provide enough energy even in a highly flexed state to be used practically to power portable electronics.

From Chapter 4:

IV. A new self-limiting electrochemical pathway of producing hierarchical MnO_2 nanostructures is accomplished by exploiting the rich oxidation state chemistry of manganese oxide.

V. The fundamental charge storage mechanism of the high surface area nanofibrils grown on MnO_2 nanowires is shown to differ depending on the solvent used.

VI. Unlike synthesis methods for other hierarchical MnO_2 nanostructures, this electrochemical synthesis method was easily applied to other heterogeneous MnO_2 materials systems to produce more complicated hierarchical/heterogeneous $Ni(OH)_2/MnO_2$ and $Co(OH)_2/MnO_2$ nanofibril/nanowire arrays

From Chapter 5:

VII. ICP-AES supports the theory of different charge storage mechanisms in different solvents for MnO_2. Where the proton in seen as the major ion in water and the cation is the major ion in organic solvents.

VIII. Upon charging, the Li fraction per MnO_2 unit may be increased to 1.5 when the cycle voltage window is expanded in organic electrolyte which is greater than the previous thought maximum of 1.0.

All of these results indicate that nanostructured MnO_2's role for future supercapacitor electrodes is very promising, but has yet to be utilized to its full capability which may be better than previously thought. We hope these results further interest in this material and one day will achieve its full potential even at high loading amounts.

Publications

An adaptation of Chapter 3: can be found in the following publication:
Phys. Chem. Chem. Phys., 2012, 14, 3329-3337

An adaptation of Chapter 4: can be found in the following publication:
ACS Nano, 2013, **7**, 1200-1214

References

1. P. Simon and Y. Gogotsi, *Nature Materials*, 2008, **7**, 845-854.

2. L. Gaines and R. Cuenca, *Costs of lithium-ion batteries for vehicles* DOI: 10.2172/761281, United States Department of Energy, 2000.

3. M. Winter and R. J. Brodd, *Chemical Reviews*, 2004, **104**, 4245-4269.

4. J. M. Tarascon and M. Armand, *Nature*, 2001, **414**, 359-367.

5. K. S. Kang, Y. S. Meng, J. Breger, C. P. Grey and G. Ceder, *Science*, 2006, **311**, 977-980.

6. M. S. Whittingham, *Chemical Reviews*, 2004, **104**, 4271-4301.

7. P. G. Bruce, B. Scrosati and J. M. Tarascon, *Angewandte Chemie-International Edition*, 2008, **47**, 2930-2946.

8. F. Cheng, Z. Tao, J. Liang and J. Chen, *Chemistry of Materials*, 2008, **20**, 667-681.

9. B. L. Ellis, K. T. Lee and L. F. Nazar, *Chemistry of Materials*, 2010, **22**, 691-714.

10. J. B. Goodenough and Y. Kim, *Chemistry of Materials*, 2010, **22**, 587-603.

11. M. G. Kim and J. Cho, *Advanced Functional Materials*, 2009, **19**, 1497-1514.

12. H. Li, Z. X. Wang, L. Q. Chen and X. J. Huang, *Advanced Materials*, 2009, **21**, 4593-4607.

13. M. Winter, J. O. Besenhard, M. E. Spahr and P. Novak, *Advanced Materials*, 1998, **10**, 725-763.

14. R. F. Service, *Science*, 2006, **313**, 902-902.

15. D. N. Futaba, K. Hata, T. Yamada, T. Hiraoka, Y. Hayamizu, Y. Kakudate, O. Tanaike, H. Hatori, M. Yumura and S. Iijima, *Nature Materials*, 2006, **5**, 987-994.

16. L. L. Zhang and X. S. Zhao, *Chemical Society Reviews*, 2009, **38**, 2520-2531.

17. D. C. Grahame, *Chemical Reviews*, 1947, **41**, 441-501.

18. P. Banerjee, I. Perez, L. Henn-Lecordier, S. B. Lee and G. W. Rubloff, *Nature Nanotechnology*, 2009, **4**, 292-296.

19. A. G. Pandolfo and A. F. Hollenkamp, *Journal of Power Sources*, 2006, **157**, 11-27.

20. C. Emmenegger, P. Mauron, A. Zuttel, C. Nutzenadel, A. Schneuwly, R. Gallay and L. Schlapbach, *Applied Surface Science*, 2000, **162**, 452-456.

21. S. Trasatti and G. Buzzanca, *Journal of Electroanalytical Chemistry*, 1971, **29**, A1-&.

22. T. C. Liu, W. G. Pell and B. E. Conway, *Electrochimica Acta*, 1997, **42**, 3541-3552.

23. L. B. Hu, W. Chen, X. Xie, N. A. Liu, Y. Yang, H. Wu, Y. Yao, M. Pasta, H. N. Alshareef and Y. Cui, *Acs Nano*, 2011, **5**, 8904-8913.

24. D. Choi, G. E. Blomgren and P. N. Kumta, *Advanced Materials*, 2006, **18**, 1178-1181.

25. W. Sugimoto, H. Iwata, Y. Yasunaga, Y. Murakami and Y. Takasu, *Angewandte Chemie-International Edition*, 2003, **42**, 4092-4096.

26. B. E. Conway, *Electrochemical supercapacitors : scientific fundamentals and technological applications*, Plenum Press, New York, 1999.

27. R. Liu, J. Duay, T. Lane and S. B. Lee, *Physical Chemistry Chemical Physics*, 2010, **12**, 4309-4316.

28. W. Sugimoto, K. Yokoshima, Y. Murakami and Y. Takasu, *Electrochimica Acta*, 2006, **52**, 1742-1748.

29. L. Taberna, S. Mitra, P. Poizot, P. Simon and J. M. Tarascon, *Nature Materials*, 2006, **5**, 567-573.

30. K. W. Chung, K. B. Kim, S. H. Han and H. Lee, *Electrochemical and Solid State Letters*, 2005, **8**, A259-A262.

31. G. Wee, H. Z. Soh, Y. L. Cheah, S. G. Mhaisalkar and M. Srinivasan, *Journal of Materials Chemistry*, 2010, **20**, 6720-6725.

32. H. Y. Lee and J. B. Goodenough, *Journal of Solid State Chemistry*, 1999, **148**, 81-84.

33. C. J. Xu, F. Y. Kang, B. H. Li and H. D. Du, *Journal of Materials Research*, 2010, **25**, 1421-1432.

34. M. Toupin, T. Brousse and D. Belanger, *Chemistry of Materials*, 2004, **16**, 3184-3190.

35. H. Y. Lee and J. B. Goodenough, *Journal of Solid State Chemistry*, 1999, **144**, 220-223.

36. S. C. Pang, M. A. Anderson and T. W. Chapman, *Journal of the Electrochemical Society*, 2000, **147**, 444-450.

37. G. P. Wang, L. Zhang and J. J. Zhang, *Chemical Society Reviews*, 2012, **41**, 797-828.

38. J. M. Miller, B. Dunn, T. D. Tran and R. W. Pekala, *Journal of the Electrochemical Society*, 1997, **144**, L309-L311.

39. M. Min, K. Machida, J. H. Jang and K. Naoi, *Journal of the Electrochemical Society*, 2006, **153**, A334-A338.

40. R. Liu and S. B. Lee, *Journal of the American Chemical Society*, 2008, **130**, 2942-2943.

41. M. D. Ingram, H. Staesche and K. S. Ryder, *Journal of Power Sources*, 2004, **129**, 107-112.

42. A. S. Arico, P. Bruce, B. Scrosati, J. M. Tarascon and W. Van Schalkwijk, *Nature Materials*, 2005, **4**, 366-377.

43. R. Liu, S. Il Cho and S. B. Lee, *Nanotechnology*, 2008, **19**.

44. Y. G. Guo, J. S. Hu and L. J. Wan, *Advanced Materials*, 2008, **20**, 2878-2887.

45. R. K. Sharma, A. C. Rastogi and S. B. Desu, *Electrochemistry Communications*, 2008, **10**, 268-272.

46. K. S. Ryu, K. M. Kim, N. G. Park, Y. J. Park and S. H. Chang, *Journal of Power Sources*, 2002, **103**, 305-309.

47. Y. Z. Zheng, H. Y. Ding and M. L. Zhang, *Materials Research Bulletin*, 2009, **44**, 403-407.

48. G. A. Snook, P. Kao and A. S. Best, *Journal of Power Sources*, 2011, **196**, 1-12.

49. S. Kirchmeyer and K. Reuter, *Journal of Materials Chemistry*, 2005, **15**, 2077-2088.

50. J. H. Jiang and A. Kucernak, *Electrochimica Acta*, 2002, **47**, 2381-2386.

51. E. Frackowiak, *Physical Chemistry Chemical Physics*, 2007, **9**, 1774-1785.

52. E. Frackowiak, V. Khomenko, K. Jurewicz, K. Lota and F. Beguin, *Journal of Power Sources*, 2006, **153**, 413-418.

53. V. Khomenko, E. Raymundo-Pinero and F. Beguin, *Journal of Power Sources*, 2006, **153**, 183-190.

54. G. X. Wang, B. L. Zhang, Z. L. Yu and M. Z. Qu, *Solid State Ionics*, 2005, **176**, 1169-1174.

55. T. Brousse, P. L. Taberna, O. Crosnier, R. Dugas, P. Guillemet, Y. Scudeller, Y. Zhou, F. Favier, D. Belanger and P. Simon, *Journal of Power Sources*, 2007, **173**, 633-641.

56. V. Ganesh, S. Pitchumani and V. Lakshminarayanan, *Journal of Power Sources*, 2006, **158**, 1523-1532.

57. Y. G. Wang, Z. D. Wang and Y. Y. Xia, *Electrochimica Acta*, 2005, **50**, 5641-5646.

58. Q. T. Qu, P. Zhang, B. Wang, Y. H. Chen, S. Tian, Y. P. Wu and R. Holze, *Journal of Physical Chemistry C*, 2009, **113**, 14020-14027.

59. V. Khomenko, E. Raymundo-Pinero, E. Frackowiak and F. Beguin, *Applied Physics a-Materials Science & Processing*, 2006, **82**, 567-573.

60. M. Pourbaix, *Atlas of electrochemical equilibria in aqueous solutions*, 2d English edn., National Association of Corrosion Engineers, Houston, Tex., 1974.

61. J. Emsley, *Nature's building blocks : an A-Z guide to the elements*, Oxford University Press, Oxford ; New York, 2001.

62. H. Hasan, *Manganese*, 1st edn., Rosen Central, New York, 2008.

63. D. Belanger, T. Brousse and J. W. Long, *The Electrochemical Society **Interface***, 2008, **17**, 49-52.

64. W. F. Wei, X. W. Cui, W. X. Chen and D. G. Ivey, *Chemical Society Reviews*, 2011, **40**, 1697-1721.

65. Y. Chabre and J. Pannetier, *Progress in Solid State Chemistry*, 1995, **23**, 1-130.

66. M. Q. Wu, G. A. Snook, G. Z. Chen and D. J. Fray, *Electrochemistry Communications*, 2004, **6**, 499-504.

67. C. C. Hu and T. W. Tsou, *Journal of Power Sources*, 2003, **115**, 179-186.

68. C. K. Lin, K. H. Chuang, C. Y. Lin, C. Y. Tsay and C. Y. Chen, *Surface & Coatings Technology*, 2007, **202**, 1272-1276.

69. M. Toupin, T. Brousse and D. Belanger, *Chemistry of Materials*, 2002, **14**, 3946-3952.

70. S. W. Donne, A. F. Hollenkamp and B. C. Jones, *Journal of Power Sources*, 2010, **195**, 367-373.

71. T. Brousse, M. Toupin, R. Dugas, L. Athouel, O. Crosnier and D. Belanger, *Journal of the Electrochemical Society*, 2006, **153**, A2171-A2180.

72. O. Ghodbane, J. L. Pascal and F. Favier, *Acs Applied Materials & Interfaces*, 2009, **1**, 1130-1139.

73. E. Beaudrouet, A. L. G. La Salle and D. Guyomard, *Electrochimica Acta*, 2009, **54**, 1240-1248.

74. Y. Hou, Y. W. Cheng, T. Hobson and J. Liu, *Nano Letters*, 2010, **10**, 2727-2733.

75. R. K. Sharma, H. S. Oh, Y. G. Shul and H. Kim, *Journal of Power Sources*, 2007, **173**, 1024-1028.

76. X. Wang and Y. D. Li, *Chemistry-a European Journal*, 2003, **9**, 300-306.

77. S. L. Chou, F. Y. Cheng and J. Chen, *Journal of Power Sources*, 2006, **162**, 727-734.

78. J. W. Long, R. M. Stroud and D. R. Rolison, *Journal of Non-Crystalline Solids*, 2001, **285**, 288-294.

79. J. G. Wen, X. Y. Ruan and Z. T. Zhou, *Journal of Physics and Chemistry of Solids*, 2009, **70**, 816-820.

80. Y. S. Chen and C. C. Hu, *Electrochemical and Solid State Letters*, 2003, **6**, A210-A213.

81. R. Liu, J. Duay and S. B. Lee, *Acs Nano*, 2011, **5**, 5608-5619.

82. R. Liu, J. Duay and S. B. Lee, *Acs Nano*, 2010, **4**, 4299-4307.

83. S. A. Sherrill, J. Duay, Z. Gui, P. Banerjee, G. W. Rubloff and S. B. Lee, *Physical Chemistry Chemical Physics*, 2011, **13**, 15221-15226.

84. S. M. Dong, X. Chen, L. Gu, X. H. Zhou, L. F. Li, Z. H. Liu, P. X. Han, H. X. Xu, J. H. Yao, H. B. Wang, X. Y. Zhang, C. Q. Shang, G. L. Cui and L. Q. Chen, *Energy & Environmental Science*, 2011, **4**, 3502-3508.

85. G. H. Yu, L. B. Hu, M. Vosgueritchian, H. L. Wang, X. Xie, J. R. McDonough, X. Cui, Y. Cui and Z. N. Bao, *Nano Lett.*, 2011, **11**, 2905-2911.

86. S. L. Chou, J. Z. Wang, S. Y. Chew, H. K. Liu and S. X. Dou, *Electrochem. Commun.*, 2008, **10**, 1724-1727.

87. J. W. Liu, J. Essner and J. Li, *Chem. Mat.*, 2010, **22**, 5022-5030.

88. L. B. Hu, M. Pasta, F. La Mantia, L. F. Cui, S. Jeong, H. D. Deshazer, J. W. Choi, S. M. Han and Y. Cui, *Nano Lett.*, 2010, **10**, 708-714.

89. A. E. Fischer, K. A. Pettigrew, D. R. Rolison, R. M. Stroud and J. W. Long, *Nano Letters*, 2007, **7**, 281-286.

90. R. Liu, J. Duay and S. B. Lee, *Chemical Communications*, 2011, **47**, 1384-1404.

91. C. Liu, F. Li, L. P. Ma and H. M. Cheng, *Advanced Materials*, 2010, **22**, E28-E31.

92. W. Xu and C. A. Angell, *Electrochemical and Solid State Letters*, 2001, **4**, L3-L3.

93. J. W. Long, C. P. Rhodes, A. L. Young and D. R. Rolison, *Nano Letters*, 2003, **3**, 1155-1161.

94. J. W. Long and D. R. Rolison, *Accounts of Chemical Research*, 2007, **40**, 854-862.

95. J. B. Fei, Y. Cui, X. H. Yan, W. Qi, Y. Yang, K. W. Wang, Q. He and J. B. Li, *Advanced Materials*, 2008, **20**, 452-455.

96. P. Yu, X. Zhang, D. L. Wang, L. Wang and Y. W. Ma, *Crystal Growth & Design*, 2009, **9**, 528-533.

97. J. Jiang, Y. Y. Li, J. P. Liu, X. T. Huang, C. Z. Yuan and X. W. Lou, *Advanced Materials*, 2012, **24**, 5166-5180.

98. Y. U. Jeong and A. Manthiram, *Journal of the Electrochemical Society*, 2002, **149**, A1419-A1422.

99. P. Ragupathy, H. N. Vasan and N. Munichandraiah, *Journal of the Electrochemical Society*, 2008, **155**, A34-A40.

100. V. Subramanian, H. W. Zhu, R. Vajtai, P. M. Ajayan and B. Q. Wei, *Journal of Physical Chemistry B*, 2005, **109**, 20207-20214.

101. X. Wang and Y. D. Li, *Chemical Communications*, 2002, 764-765.

102. M. Xu, L. Kong, W. Zhou and H. Li, *Journal of Physical Chemistry C*, 2007, **111**, 19141-19147.

103. N. A. Tang, X. K. Tian, C. Yang and Z. B. Pi, *Materials Research Bulletin*, 2009, **44**, 2062-2067.

104. A. Zolfaghari, F. Ataherian, M. Ghaemi and A. Gholami, *Electrochimica Acta*, 2007, **52**, 2806-2814.

105. M. Ghaemi, F. Ataherian, A. Zolfaghari and S. M. Jafari, *Electrochimica Acta*, 2008, **53**, 4607-4614.

106. P. Yu, X. Zhang, Y. Chen, Y. W. Ma and Z. P. Qi, *Materials Chemistry and Physics*, 2009, **118**, 303-307.

107. S. Bach, M. Henry, N. Baffier and J. Livage, *Journal of Solid State Chemistry*, 1990, **88**, 325-333.

108. R. N. Reddy and R. G. Reddy, *Journal of Power Sources*, 2003, **124**, 330-337.

109. R. N. Reddy and R. G. Reddy, *Journal of Power Sources*, 2004, **132**, 315-320.

110. X. Y. Wang, X. Y. Wang, W. G. Huang, P. J. Sebastian and S. Gamboa, *Journal of Power Sources*, 2005, **140**, 211-215.

111. S. Franger, S. Bach, J. Farcy, J. P. Pereira-Ramos and N. Baffier, *Journal of Power Sources*, 2002, **109**, 262-275.

112. P. K. Nayak, S. Devaraj and N. Munichandraiah, *Electrochemical and Solid State Letters*, 2010, **13**, F29-F32.

113. P. K. Nayak and N. Munichandraiah, *Electrochemical and Solid State Letters*, 2009, **12**, A115-A119.

114. I. Zhitomirsky, M. Cheong and J. Wei, *Jom*, 2007, **59**, 66-69.

115. G. M. Jacob and I. Zhitomirsky, *Applied Surface Science*, 2008, **254**, 6671-6676.

116. J. Wei, N. Nagarajan and I. Zhitomirsky, *Journal of Materials Processing Technology*, 2007, **186**, 356-361.

117. J. N. Broughton and M. J. Brett, *Electrochimica Acta*, 2005, **50**, 4814-4819.

118. M. Nakayama, A. Tanaka, Y. Sato, T. Tonosaki and K. Ogura, *Langmuir*, 2005, **21**, 5907-5913.

119. S. Rodrigues, N. Munichandraiah and A. K. Shukla, *J. Appl. Electrochem.*, 1998, **28**, 1235-1241.

120. H. Zhang, G. P. Cao, Z. Y. Wang, Y. S. Yang, Z. J. Shi and Z. N. Gu, *Nano Letters*, 2008, **8**, 2664-2668.

121. Q. Cheng, J. Tang, J. Ma, H. Zhang, N. Shinya and L. C. Qin, *Carbon*, **49**, 2917-2925.

122. H. Xia, J. K. Feng, H. L. Wang, M. O. Lai and L. Lu, *Journal of Power Sources*, **195**, 4410-4413.

123. C. L. Xu, S. J. Bao, L. B. Kong, H. Li and H. L. Li, *Journal of Solid State Chemistry*, 2006, **179**, 1351-1355.

124. S. Devaraj and N. Munichandraiah, *Electrochemical and Solid State Letters*, 2005, **8**, A373-A377.

125. M. S. Wu, J. T. Lee, Y. Y. Wang and C. C. Wan, *Journal of Physical Chemistry B*, 2004, **108**, 16331-16333.

126. J. Chen, W. D. Zhang and J. S. Ye, *Electrochemistry Communications*, 2008, **10**, 1268-1271.

127. G. H. Yu, L. B. Hu, M. Vosgueritchian, H. L. Wang, X. Xie, J. R. McDonough, X. Cui, Y. Cui and Z. N. Bao, *Nano Letters*, **11**, 2905-2911.

128. M. Nakayama, T. Kanaya and R. Inoue, *Electrochemistry Communications*, 2007, **9**, 1154-1158.

129. D. B. Williams and C. B. Carter, *Transmission electron microscopy : a textbook for materials science*, 2nd edn., Springer, New York, 2008.

130. J. Li and I. Zhitomirsky, *Colloids and Surfaces a-Physicochemical and Engineering Aspects*, 2009, **348**, 248-253.

131. J. Li and I. Zhitomirsky, *Journal of Materials Processing Technology*, 2009, **209**, 3452-3459.

132. B. Djurfors, J. N. Broughton, M. J. Brett and D. G. Ivey, *Journal of Materials Science*, 2003, **38**, 4817-4830.

133. P. A. G. Nelson, K. G. Bloom, I. Dees, D. W., *Modeling the performance and cost of lithium-ion batteries for electric-drive vehicles* ANL-11/32; TRN: US201123%%348.

134. P. Taheri, S. Hsieh and M. Bahrami, *J. Power Sources*, 2011, **196**, 6525-6533.

135. N. F. Yu, L. J. Gao, S. H. Zhao and Z. D. Wang, *Electrochim. Acta*, 2009, **54**, 3835-3841.

136. K. W. Nam and K. B. Kim, *J. Electrochem. Soc.*, 2002, **149**, A346-A354.

137. A. Patil, V. Patil, D. W. Shin, J. W. Choi, D. S. Paik and S. J. Yoon, *Materials Research Bulletin*, 2008, **43**, 1913-1942.

138. T. Xue, C. L. Xu, D. D. Zhao, X. H. Li and H. L. Li, *Journal of Power Sources*, 2007, **164**, 953-958.

139. S. Kawai and R. Ueda, *J. Electrochem. Soc.*, 1975, **122**, 32-36.

140. G. D. Sulka,Nanostructured Materials in Electrochemistry, 2008 1-120.

141. M. M. Shaijumon, F. S. Ou, L. J. Ci and P. M. Ajayan, *Chemical Communications*, 2008, 2373-2375.

142. A. L. M. Reddy, M. M. Shaijumon, S. R. Gowda and P. M. Ajayan, *Journal of Physical Chemistry C*, 2010, **114**, 658-663.

143. S. R. Gowda, A. L. M. Reddy, X. B. Zhan, H. R. Jafry and P. M. Ajayan, *Nano Letters*, 2012, **12**, 1198-1202.

144. A. Finke, P. Poizot, C. Guery, L. Dupont, P. L. Taberna, P. Simon and J. M. Tarascon, *Electrochemical and Solid State Letters*, 2008, **11**, E5-E9.

145. E. Perre, L. Nyholm, T. Gustafsson, P. L. Taberna, P. Simon and K. Edstrom, *Electrochemistry Communications*, 2008, **10**, 1467-1470.

146. S. K. Cheah, E. Perre, M. Rooth, M. Fondell, A. Harsta, L. Nyholm, M. Boman, T. Gustafsson, J. Lu, P. Simon and K. Edstrom, *Nano Letters*, 2009, **9**, 3230-3233.

147. L. Bazin, S. Mitra, P. L. Taberna, P. Poizot, M. Gressier, M. J. Menu, A. Barnabe, P. Simon and J. M. Tarascon, *Journal of Power Sources*, 2009, **188**, 578-582.

148. S. Il Cho and S. B. Lee, *Accounts of Chemical Research*, 2008, **41**, 699-707.

149. R. Xiao, S. Il Cho, R. Liu and S. B. Lee, *Journal of the American Chemical Society*, 2007, **129**, 4483-4489.

150. R. F. Egerton, *Physical principles of electron microscopy : an introduction to TEM, SEM, and AEM*, Springer, New York, NY, 2005.

151. D. Briggs and J. T. Grant, *Surface analysis by Auger and x-ray photoelectron spectroscopy*, IM Publications, Chichester, West Sussex, U.K., 2003.

152. A. A. Audi and P. M. A. Sherwood, *Surface and Interface Analysis*, 2002, **33**, 274-282.

153. D. A. Skoog, F. J. Holler and S. R. Crouch, *Principles of instrumental analysis*, 6th edn., Thomson Brooks/Cole, Belmont, CA, 2007.

154. B. S. Shim, W. Chen, C. Doty, C. L. Xu and N. A. Kotov, *Nano Letters*, 2008, **8**, 4151-4157.

155. J. A. Rogers, Z. Bao, K. Baldwin, A. Dodabalapur, B. Crone, V. R. Raju, V. Kuck, H. Katz, K. Amundson, J. Ewing and P. Drzaic, *Proceedings of the National Academy of Sciences of the United States of America*, 2001, **98**, 4835-4840.

156. X. F. Zhuang, D. S. Lin, O. Oralkan and B. T. Khuri-Yakub, *Journal of Microelectromechanical Systems*, 2008, **17**, 446-452.

157. D. Linden and T. B. Reddy, *Handbook of batteries*, 3rd edn., McGraw-Hill, New York, 2002.

158. J. R. Miller and P. Simon, *Science*, 2008, **321**, 651-652.

159. A. Burke, *Journal of Power Sources*, 2000, **91**, 37-50.

160. S. Yoon, J. W. Lee, T. Hyeon and S. M. Oh, *Journal of the Electrochemical Society*, 2000, **147**, 2507-2512.

161. G. Salitra, A. Soffer, L. Eliad, Y. Cohen and D. Aurbach, *Journal of the Electrochemical Society*, 2000, **147**, 2486-2493.

162. Y. P. Zhai, Y. Q. Dou, D. Y. Zhao, P. F. Fulvio, R. T. Mayes and S. Dai, *Advanced Materials*, 2011, **23**, 4828-4850.

163. Y. G. Wang, H. Q. Li and Y. Y. Xia, *Advanced Materials*, 2006, **18**, 2619-2621.

164. L. Z. Fan and J. Maier, *Electrochemistry Communications*, 2006, **8**, 937-940.

165. A. Laforgue, P. Simon, C. Sarrazin and J. F. Fauvarque, *Journal of Power Sources*, 1999, **80**, 142-148.

166. J. W. Long, K. E. Swider, C. I. Merzbacher and D. R. Rolison, *Langmuir*, 1999, **15**, 780-785.

167. R. Liu, J. Duay, T. Lane and S. B. Lee, *Physical Chemistry Chemical Physics*, 2010, **12**, 4309-4316.

168. S. M. Dong, X. Chen, L. Gu, X. H. Zhou, L. F. Li, Z. H. Liu, P. X. Han, H. X. Xu, J. H. Yao, H. B. Wang, X. Y. Zhang, C. Q. Shang, G. L. Cui and L. Q. Chen, *Energy & Environmental Science*, 2011, **4**, 3502-3508.

169. M. J. Deng, J. K. Chang, C. C. Wang, K. W. Chen, C. M. Lin, M. T. Tang, J. M. Chen and K. T. Lu, *Energy & Environmental Science*, 2011, **4**, 3942-3946.

170. X. H. Lu, D. Z. Zheng, T. Zhai, Z. Q. Liu, Y. Y. Huang, S. L. Xie and Y. X. Tong, *Energy & Environmental Science*, 2011, **4**, 2915-2921.

171. S. A. Sherrill, J. Duay, Z. Gui, P. Banerjee, G. W. Rubloff and S. B. Lee, *Physical Chemistry Chemical Physics*, 2011, **13**, 15221-15226.

172. S. Y. Wang, K. C. Ho, S. L. Kuo and N. L. Wu, *Journal of the Electrochemical Society*, 2006, **153**, A75-A80.

173. D. D. Zhao, S. J. Bao, W. H. Zhou and H. L. Li, *Electrochemistry Communications*, 2007, **9**, 869-874.

174. G. W. Yang, C. L. Xu and H. L. Li, *Chem. Commun.*, 2008, 6537-6539.

175. K. S. Ryu, Y. G. Lee, Y. S. Hong, Y. J. Park, X. L. Wu, K. M. Kim, M. G. Kang, N. G. Park and S. H. Chang, *Electrochimica Acta*, 2004, **50**, 843-847.

176. R. Liu, J. Duay and S. B. Lee, *Acs Nano*, 2011, **5**, 5608-5619.

177. R. Liu, J. Duay and S. B. Lee, *Acs Nano*, 2010, **4**, 4299-4307.

178. P. C. Chen, G. Z. Shen, Y. Shi, H. T. Chen and C. W. Zhou, *Acs Nano*, 2010, **4**, 4403-4411.

179. T. Brousse, M. Toupin and D. Belanger, *Journal of the Electrochemical Society*, 2004, **151**, A614-A622.

180. Q. T. Qu, P. Zhang, B. Wang, Y. H. Chen, S. Tian, Y. P. Wu and R. Holze, *Journal of Physical Chemistry C*, 2009, **113**, 14020-14027.

181. A. Malak, K. Fic, G. Lota, C. Vix-Guterl and E. Frackowiak, *Journal of Solid State Electrochemistry*, 2010, **14**, 811-816.

182. Q. Cheng, J. Tang, J. Ma, H. Zhang, N. Shinya and L. C. Qin, *Carbon*, 2011, **49**, 2917-2925.

183. C. Z. Meng, C. H. Liu, L. Z. Chen, C. H. Hu and S. S. Fan, *Nano Letters*, 2010, **10**, 4025-4031.

184. E. Raymundo-Pinero, V. Khomenko, E. Frackowiak and F. Beguin, *Journal of the Electrochemical Society*, 2005, **152**, A229-A235.

185. J. Perez-Ramirez, C. H. Christensen, K. Egeblad, C. H. Christensen and J. C. Groen, *Chemical Society Reviews*, 2008, **37**, 2530-2542.

186. F. L. Zheng, G. R. Li, Y. N. Ou, Z. L. Wang, C. Y. Su and Y. X. Tong, *Chem. Commun.*, 2010, **46**, 5021-5023.

187. S. Y. Gao, S. X. Yang, J. Shu, S. X. Zhang, Z. D. Li and K. Jiang, *Journal of Physical Chemistry C*, 2008, **112**, 19324-19328.

188. F. Sauvage, F. Di Fonzo, A. L. Bassi, C. S. Casari, V. Russo, G. Divitini, C. Ducati, C. E. Bottani, P. Comte and M. Graetzel, *Nano Letters*, 2010, **10**, 2562-2567.

189. J. Song, D. S. Jensen, D. N. Hutchison, B. Turner, T. Wood, A. Dadson, M. A. Vail, M. R. Linford, R. R. Vanfleet and R. C. Davis, *Advanced Functional Materials*, 2011, **21**, 1132-1139.

190. J. Y. Liu, Z. Guo, F. L. Meng, Y. Jia, T. Luo, M. Q. Li and J. H. Liu, *Crystal Growth & Design*, 2009, **9**, 1716-1722.

191. V. T. Le, T. N. L. Le and V. H. Nguyen, *Sensors and Actuators B-Chemical*, 2010, **150**, 112-119.

192. F. Y. Cheng, J. Z. Zhao, W. Song, C. S. Li, H. Ma, J. Chen and P. W. Shen, *Inorganic Chemistry*, 2006, **45**, 2038-2044.

193. Y. S. Ding, X. F. Shen, S. Gomez, H. Luo, M. Aindow and S. L. Suib, *Advanced Functional Materials*, 2006, **16**, 549-555.

194. H. L. Wang, L. F. Cui, Y. A. Yang, H. S. Casalongue, J. T. Robinson, Y. Y. Liang, Y. Cui and H. J. Dai, *Journal of the American Chemical Society*, 2010, **132**, 13978-13980.

195. B. Ammundsen and J. Paulsen, *Advanced Materials*, 2001, **13**, 943-946.

196. A. L. M. Reddy, M. M. Shaijumon, S. R. Gowda and P. M. Ajayan, *Nano Letters*, 2009, **9**, 1002-1006.

197. C. C. Hu and T. W. Tsou, *Electrochemistry Communications*, 2002, **4**, 105-109.

198. W. B. Yan, T. Ayvazian, J. Kim, Y. Liu, K. C. Donavan, W. D. Xing, Y. G. Yang, J. C. Hemminger and R. M. Penner, *Acs Nano*, 2011, **5**, 8275-8287.

199. B. E. Conway, V. Birss and J. Wojtowicz, *Journal of Power Sources*, 1997, **66**, 1-14.

200. Z. Q. Li, Y. Ding, Y. J. Xiong, Q. Yang and Y. Xie, *Chem. Commun.*, 2005, 918-920.

201. J. H. Kim, T. Ayalasomayajula, V. Gona and D. Choi, *Journal of Power Sources*, 2008, **183**, 366-369.

202. O. Bricker, *American Mineralogist*, 1965, **50**, 1296-1302.

203. C. Julien, M. Massot, R. Baddour-Hadjean, S. Franger, S. Bach and J. P. Pereira-Ramos, *Solid State Ionics*, 2003, **159**, 345-356.

204. Y. K. Hsu, Y. C. Chen, Y. G. Lin, L. C. Chen and K. H. Chen, *Chem. Commun.*, 2011, **47**, 1252-1254.

205. M. C. Bernard, A. H. L. Goff, B. V. Thi and S. C. Detorresi, *Journal of the Electrochemical Society*, 1993, **140**, 3065-3070.

206. L. A. Grunes, R. D. Leapman, C. N. Wilker, R. Hoffmann and A. B. Kunz, *Physical Review B*, 1982, **25**, 7157-7173.

207. H. Kurata, E. Lefevre, C. Colliex and R. Brydson, *Physical Review B*, 1993, **47**, 13763-13768.

208. A. P. Grosvenor, M. C. Biesinger, R. S. Smart and N. S. McIntyre, *Surface Science*, 2006, **600**, 1771-1779.

209. J. Yang, H. W. Liu, W. N. Martens and R. L. Frost, *Journal of Physical Chemistry C*, 2010, **114**, 111-119.

210. T. C. Liu, W. G. Pell, B. E. Conway and S. L. Roberson, *Journal of the Electrochemical Society*, 1998, **145**, 1882-1888.

211. J. Wang, J. Polleux, J. Lim and B. Dunn, *Journal of Physical Chemistry C*, 2007, **111**, 14925-14931.

212. S. Ardizzone, G. Fregonara and S. Trasatti, *Electrochimica Acta*, 1990, **35**, 263-267.

213. C. P. Depauli and S. Trasatti, *Journal of Electroanalytical Chemistry*, 1995, **396**, 161-168.

214. X. H. Tang, Z. H. Liu, C. X. Zhang, Z. P. Yang and Z. L. Wang, *Journal of Power Sources*, 2009, **193**, 939-943.

215. Z. P. Li, J. Q. Wang, Z. F. Wang, H. Q. Ran, Y. Li, X. X. Han and S. R. Yang, *New Journal of Chemistry*, 2012, **36**, 1490-1495.

216. C. C. Hu, C. Y. Hung, K. H. Chang and Y. L. Yang, *Journal of Power Sources*, 2011, **196**, 847-850.

217. A. Sumboja, U. M. Tefashe, G. Wittstock and P. S. Lee, *Journal of Power Sources*, 2012, **207**, 205-211.

218. S. K. Meher and G. R. Rao, *Journal of Power Sources*, 2012, **215**, 317-328.

219. J. P. Liu, J. Jiang, M. Bosman and H. J. Fan, *Journal of Materials Chemistry*, 2012, **22**, 2419-2426.

220. J. P. Liu, J. Jiang, C. W. Cheng, H. X. Li, J. X. Zhang, H. Gong and H. J. Fan, *Advanced Materials*, 2011, **23**, 2076-2081.

221. K. W. Nam, C. W. Lee, X. Q. Yang, B. W. Cho, W. S. Yoon and K. B. Kim, *Journal of Power Sources*, 2009, **188**, 323-331.

222. Y. K. Hsu, Y. C. Chen, Y. G. Lin, L. C. Chen and K. H. Chen, *Chemical Communications*, 2011, **47**, 1252-1254.

223. M. Nakayama and H. Tagashira, *Langmuir*, 2006, **22**, 3864-3869.

224. S. L. Kuo and N. L. Wu, *Journal of the Electrochemical Society*, 2006, **153**, A1317-A1324.

225. K. W. Nam, M. G. Kim and K. B. Kim, *Journal of Physical Chemistry C*, 2007, **111**, 749-758.

226. M. Nakayama, T. Kanaya, J. W. Lee and B. N. Popov, *Journal of Power Sources*, 2008, **179**, 361-366.

227. M. C. Santos, A. J. Terezo, V. C. Fernandes, E. C. Pereira and L. O. S. Bulhoes, *Journal of Solid State Electrochemistry*, 2005, **9**, 91-95.

228. C. J. Xu, C. G. Wei, B. H. Li, F. Y. Kang and Z. C. Guan, *Journal of Power Sources*, 2011, **196**, 7854-7859.

229. S. Wen, J. W. Lee, I. H. Yeo, J. Park and S. Mho, *Electrochimica Acta*, 2004, **50**, 849-855.